Trajectory design for a Titan mission using the Direct Fusion Drive

Politecnico di Torino

Corso di Laurea Magistrale in Ingegneria Aerospaziale

Relatori:
Prof.ssa Sabrina Corpino
Prof.   Roman Ya. Kezerashvili

Candidato:
Marco Gajeri

July 2020

Trajectory design for a Titan mission using the Direct Fusion Drive

Politecnico di Torino,
CUNY City College of Technology

Master Degree in Aerospace Engineering

Supervisors:
Prof.ssa Sabrina Corpino
Prof.   Roman Ya. Kezerashvili

Candidate:
Marco Gajeri

July 2020

Abstract

Titan is the only satellite in our Solar System with a dense atmosphere similar to the Earth. The main purpose of this work is to perform analysis of realistic new trajectories for a robotic mission to Saturn's largest moon, Titan in order to demonstrate the great advantages related to the Direct Fusion Drive (DFD). The DFD is based on a D-^{3}He fueled, aneutronic, thermonuclear fusion propulsion system, related to the ongoing fusion research at Princeton Plasma Physics Laboratory [1] (PPPL). This fusion propulsion concept is based on a magnetically confined field reversed configuration plasma, where the deuterium propellant is heated by fusion products, and then expanded into a magnetic nozzle, providing both thrust and electrical energy to the spacecraft.

The trajectories calculations for the Titan mission are obtained based on the estimated characteristics provided by the PPPL [1]. We considered a 2-MW-class single DFD module, which provides 8 N of constant thrust and a specific impulse of $\approx 10^4$ s. Two different profile missions have been considered: the first one is a thrust-coast-thrust profile with constant thrust and specific impulse and the second is a continuous and constant thrust profile, with a switch in thrust direction operated in the last phases of the mission. Each mission is divided into four different phases, starting from the initial Low Earth Orbit departure, the interplanetary trajectory, Saturn orbit insertion and the Titan orbit insertion. For all mission phases, maneuver time and propellant consumption have been calculated. The results of calculations and mission analysis offer a complete overview of the advantages in term of payload mass and travel time. The first scenario analysed is the thrust-coast-thrust profile mission which is based on the assumption that the DFD is capable to turn off and on the thrust generation, though without restart the engine. This is an important hypothesis which requires that the engine will not produce thrust for about a year, which is in theory possible but not yet certain, without stopping to generate the electrical power arising from the fusion reactions. The second scenario is the continuous thrust profile mission, which leads to the advantage related to the shortening of the total mission duration, which makes also possible to save precious fuel (^{3}He) if compared with the main scenario of the thrust-coast-thrust profile mission. This second profile mission results into a shorter time travel mission with a not negligible decrease in payload capability related to the fact that the propellant consumption is more than doubled.

It is important to emphasize that the deceleration capability is one of the DFD game changer: in fact, the DFD performance allows to rapidly reach high velocity and decelerate in even shorter time period via low-thrust maneuvers, that would have been too demanding for any kind of current propulsion systems. This capability results in a total trip duration of 2.6 years for the thrust-coast-thrust profile and less than 2 years considering the continuous thrust profile. The high payload enabling capability, combined with the huge electrical power available from the fusion reactor, leads to a tremendous advantage compared with present technology.

Contents

List of Figures

7

List of Tables

1 Introduction

The emotional desire to explore and challenge the boundaries of our knowledge has allowed us to evolve and make amazing discoveries. As our ancestors searched and discovered new lands so we are exploring the universe, looking for pleasant answers. Because of its relative proximity, human exploration began with Earth's natural satellite, tooking first men to walk on lunar soil in 1969 [2]. At the beginnings of the sixties first robotic Mars missions were designed and launched [3]. A key aspect, as well known, concerns the payload mission capability. The higher the payload mass, the more scientific instruments can be carry onboard the spacecraft and the more precious scientific data are collectable. This is very important both for robotic and manned missions, such as the near future lunar and Mars missions, where it would be significant to increase the payload as much as possible, without excessively extend the journey time. One can say that new propulsion concept need to be developed in order to colonize our Solar system, overcoming the limitations related to chemical and electric propulsion (CP and EP respectively). In fact, considering current solutions, low power EP systems are affected by long journey time although their high specific impulse ($I_{sp} \approx 1500 - 5000$ s), because of the extremely low thrust. CP systems are not convenient due to the limitation on the maximum specific impulse ($I_{sp} \approx 450$ s) [4], directly dependent on the fuel chemical energy. Shorter the time, higher the mass at launch, and so the cost.

The main issue for human space exploration is the huge vastness of space, that condemns space travelers to lengthy travel times. In a long journey in space physiological response to microgravity adaptation has all the features of accelerated aging (about 10 times faster) involving almost all body systems [5]. Surely, before humanity can succeed in a Mars manned mission, a great technological advancement will have to be carried out, which must concern many fields with a particular focus on propulsion. At present, round-trip may take up to three years to complete and research suggests that astronauts could lose close to half their bone mass before they return [6].

1.1 New propulsion solution for space exploration

One can say that in order to colonize our Solar system new propulsion concept need to be developed. Taking into account for instance manned mission, travel is expensive and it requires long time frames, and with present technology reaching outer space would take much longer. Therefore, new technologies directly related to propulsion systems are necessary both for manned and unmanned missions.

1.1.1 Solar sail propulsion

Whereas the purpose of interplanetary or interstellar space exploration, an interesting alternative to chemical and electric propulsion is represented by Solar Sail propulsion. In fact traditionally, deep space exploration has been limited by physical characteristics of chemical rocket engines and more specifically by the amount of fuel that a spacecraft needs onboard to generate thrust in space. In fact chemical rockets provide powerful bursts of acceleration for relatively short times with low specific impulse offering high

thrust. And even though solar sail acceleration is much slower, it has the advantage of a continuous thrust (as well as for the electric propulsion) which is "directly" related to the energy furnished by the Sun photons flux [7, 8]. This means that solar sail-propelled spacecraft can reach speeds that would be practically impossible for chemical/electric propulsion to achieve [9]. Moreover, there is no need to carry heavy fuel tanks which limit the precious transportable amount of payload. Thanks to the discoveries of James Clerk Maxwell (1865) [10, 11], Solar sails generate thrust by exploiting radiation pressure related to electromagnetic waves and in some cases also due to solar wind, much the way wind pushes ship's sails across water. Depending on mission destination, the size of the sail differs from a few meters up to 1,000 meters in diameter, and usually is square in shape. Solar sail's ability to achieve high ΔV missions cheaply can significantly reduce the cost of interplanetary missions. Furthermore, the possibility of a hybrid design, where a solar sail is in addition to an electric propulsion system, is being still studied [12].

In the seventies, NASA considered to try the first solar sail flight to perform a rendezvous with Comet Halley flyby of Earth (1986), but unfortunately the mission was considered unfeasible, due to the low technological level at that time. Many space agencies thought about several missions during the next decades, but only in 2010 there was the launch of the first mission ever (IKAROS) to have demonstrated solar sail technology in interplanetary space [13, 14]. During this mission, planned by the Japan Aerospace Exploration Agency (JAXA), deployment system of the sail and guidance, navigation control skill have been succesfully tested. Meanwhile, one of the most promising current proposed mission is Breakthrough Starshot, where a highly reflective photon sail is pushed by a powerful terrestrial laser array [15]. This ambitious project is still under development by the Breakthrough Initiatives, founded in 2016 by Stephen Hawking, Yuri Milner and Mark Zuckerberg. The main purpose of the mission is to demonstrate the functioning for ultra-fast light-driven nanocrafts, performing a flyby mission to reach Alpha Centauri in just over 20 years, sending back to Earth images of its recently-discovered planet Proxima b, as well as collecting other scientific data such as analysis of magnetic fields [16].

1.1.2 Nuclear propulsion

Certanly, one can say that a full range of technological advancements need to be developed to explore and colonize our solar system and beyond. For instance one should be able to access and take advantage of in situ resources or to better protect travelers from physiological problems of space travel, etc. It is also true that new technologies directly related to spacecraft propulsion are essential, because of the consequently shortening of the travel times [17]. In fact, considering manned space exploration, travel time becomes crucial and impose to dismiss solar sail propulsion solution which remains an excellent candidate for future unmanned space exploration [18, 9]. Therefore, it is natural to think about using nuclear energy instead of chemical energy to propel spacecraft which could reach Mars in about half the time of current Mars missions. The exploration of the solar system requires advanced propulsion techniques capable of specific impulse above 10^4 s and specific power in the range $1 - 10$ kW/kg [19], which is related to the specific mass α expressed in kg/kW (the thrust power per unit mass). In particular, nuclear fusion is the most interesting option to meet these requirements, excluding mass annihilation solution

due to the enormous technological difficulties linked to its development.

The idea of using nuclear power for spacecraft propulsion arises from the high energy density of the fuel and the high velocity of the fusion products. The onboard nuclear reactor provides heat which allows a higher effective exhaust velocity that would have to increase payload capacity. Mainly there are two ways to use this huge amount of energy to generate propulsive thrust: nuclear thermal propulsion (NTP) and nuclear electric propulsion (NEP), although nuclear rocket systems also include hybrid NTP/NEP concepts, and interesting nuclear pulse rockets exploiting the energy of nuclear explosions like in the ORION project [20, 21]. Several designs for nuclear based rockets already exists [22], including solid, liquid, and gas core. Solid core nuclear rockets, a relatively mature propulsion technology, operate by pumping the liquid hydrogen propellant through narrow channels in a solid nuclear reactor. As liquid hydrogen moves through the channels, it is heated by the reactor into a high temperature gas, and then ejected from the exhaust nozzle of the rocket at high speeds. Liquid and gas core nuclear rockets operate according to a similar principle, but, instead of using a solid fuel core to heat the hydrogen propellant, they use a liquid or gaseous nuclear fuel, respectively.

1.1.3 Nuclear thermal propulsion and Nuclear Electric Propulsion

A nuclear thermal rocket is a type of rocket where the energy of nuclear reaction, nuclear fusion or fission, replaces the chemical energy of the fuel. A working fluid, usually liquid hydrogen, is heated to a high temperature in a nuclear reactor and then expands through a nozzle to generate thrust and the high plasma temperatures result in very high specific impulses. In 1961, NASA decide to estabilish the nuclear engine for rocket vehicle application (NERVA) program, with the purpose to design, build, and test nuclear reactors [23].

Instead, Nuclear Electric Rockets convert thermal energy, arising from nuclear reactions, to electrical energy, through a conventional thermodynamic cycle. Then this energy, which could be stored, is used to supply any kind of electrical spacecraft propulsion technology (such as ion thruster). In contrast with nuclear thermal propulsion, which directly uses reactor heat to add energy to a working fluid, in NEP the "rocket" part of the propulsion system could also be driven by batteries for instance. A central issue in any NEP mission analysis is the mass budget, where the most important contributions come from the ion thruster itself, the power processing unit (PPU), the propellant and the reactor, among which the nuclear reactor power system, is often the most remarkable. In 1965, the first flight test of a space nuclear reactor, the SNAP-10A (systems nuclear auxiliary power USA program) was conducted. It consisted of a cooled reactor, with uranium–zirconium hydride fuel, where thermoelectric power conversion was used with a specific mass of about 670 kg/kW [24]. During the test the engine operated for 40 days, producing a maximum power of 650 W. About twenty years later, with the SP-100 space reactor program, a 100 kW reactor was designed in which the overall mass of the system would have been about 4600 kg, including radiation shield, within a specific mass of about 46 kg/kW if everything worked as intended [25].

1.2 Nuclear stability

Nuclei of all elements exist in their stable form due to the strength of nuclear interactions between internal constituents. As is well known, the internal component parts of a nucleus are neutrons and protons, which are called *nucleons*. Definitely, a crucial point is related to the nuclear binding energy, which is the *minimum* energy necessary to separate the nucleus of an atom into protons and neutrons.
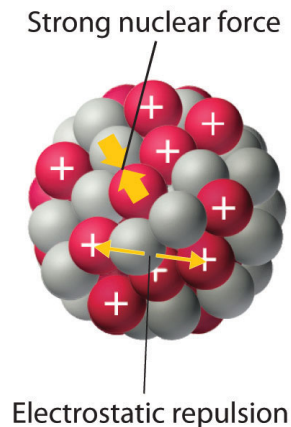
Figure 1.1: Generic representation of an atomic nucleus structure, where protons and neutrons are shown like spherical particles, respectively red and grey [26].

Moreover, it is important to emphasize that considering nuclear interactions, principle of mass conservation is no longer fully adequate. In fact, the mass of an atomic nucleus is less than the sum of the individual masses of the free constituent protons and neutrons, according to Einstein's equation [27]:

$$E = mc^2. \tag{1.1}$$

This missing mass represents the energy that was released when the nucleus was formed. Considering the periodic table of elements, starting from light elements as hydrogen and moving to the heavier ones, it has been noted that binding energy per nucleon increases. This growth is generated by increasing forces per nucleon in the nucleus, related to the increase of the atomic mass, because each additional nucleon is attracted by other nucleons, and this results in more tightly bounds. Further increasing the atomic mass, there is a saturation region with constant energy, where the electromagnetic repulsive forces begin to counterbalance the nuclear attractive ones. Finally, evaluating the heaviest elements (nuclei comprising a minimum of 209 nucleons), there is a decrease in the bond energy per nucleon as the atomic mass increases due to the fact that the large number of nucleons within the nucleus causes electromagnetic repulsive forces which start to overcome the strong nuclear force attraction.
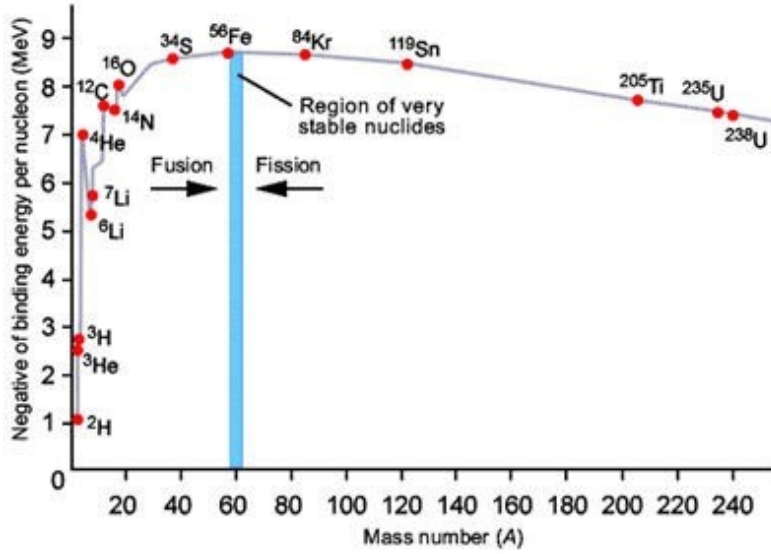
Figure 1.2: Dependence of binding energy per nucleon on nucleon number (mass number, A) [26].

At the peak of the graph shown in Fig. 1.2, nickel-62 is the most tightly bound nucleus (per nucleon), followed by iron-56 and iron-58. The fact that the maximum is related to medium sized nuclei is linked to the balance in the effects of the above mentioned opposing forces that have different range characteristics. In fact, in contrast to Coulombian force, which falls off as the inverse square of distance, the strong nuclear force has a range of action much smaller, as consequence of its exponential proportionality with distance. The above mentioned conversion of mass to energy, and vice versa, is consistent with Einstein's mass-energy equivalence formula:

$$\Delta E = \Delta m c^2, \tag{1.2}$$

in which, ΔE is the energy release, Δm the mass defect, and c is the speed of light in a vacuum ($c \approx 3 \cdot 10^8$ m/s). Therefore, thinking to notions predicated on this elegant and simple equation, the more mass disappears, the more energy is released. This physical mechanism is exactly what governs all nuclear reactions exploited to generate energy in the universe, from stellar nucleosynthesis to human build nuclear reactors.

17

1.2.1 Nuclear fission

The first nuclear reaction that man has used, which takes advantage of the just mentioned fundamental physical mechanism, is fission. Nuclear fission is the process of splitting apart nuclei, such as uranium-235, in order to release a great amount of energy. Because of the fact that nucleons in each fission son element are more tightly bound to one another than the nucleons in father nucleus, as it is appreciable in Fig. 1.2, the fission process releases energy according to Einstein's equation.
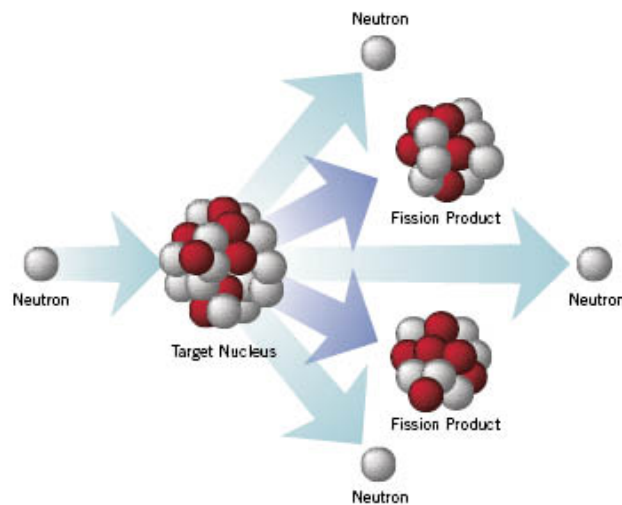
Figure 1.3: Schematic illustration of the nuclear fission process, where a neutron hits the target nucleus, which splits apart, realeasing fission products and energy [28].

The enormous energy that is released from this splitting also comes from how hard the protons are repelling each other due to the Coulomb force, barely held together by the strong nuclear force. Nucleus's protons repel each other with a considerable force for such small particles. Then, a sizeable amount of mass disappears converting into energy released. Whereas an heavy unstable nucleus, if a thermal neutron, any free neutron that has an average energy of motion (kinetic energy) corresponding to the average energy of the particles of the ambient materials, strikes it there is a high probability that fission process occours and products are formed, such as smaller nuclei and few neutrons.

1.2.2 Nuclear fusion

Nuclear fusion is a type of reaction where two light nuclei collide together to form a single, heavier nucleus and releases much more energy than any other fission reactions. The products of this reaction are generally unstable compound nuclei, and thus they decay into more stable products.
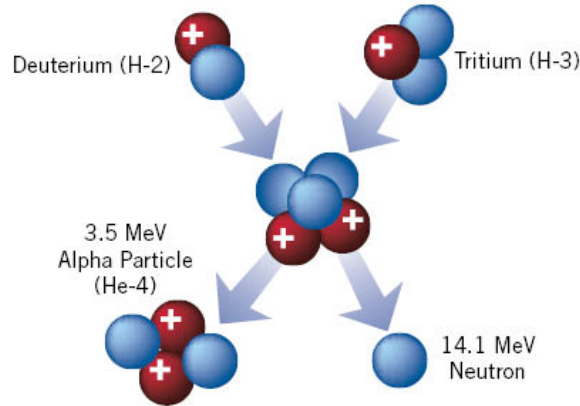
Figure 1.4: Schematic illustration of the nuclear fusion process, where two light nuclei collide together to form a single, heavier nucleus releaseing energy [28].

This fusion results in a release of energy because the mass of the new nucleus is less than the sum of the original masses. Based on the principle of mass-energy equivalence, this mass difference means that some mass has been converted into energy in analogy with fission process. For elements lighter than iron, fusion yields energy. For elements heavier than iron, it is instead a process of fission that results in a yield of energy. Although there is a large yield in energy from the nuclear fusion process, there are forces that must be overcome to initiate this process. All nuclei are charged and an initial amount of kinetic energy is necessary to increase their probability of penetrating the Coulomb barrier, which normally, keeps them apart and prevents fusion from taking place. In Fig. 1.5 the trend of the potential between two nuclei is represented.
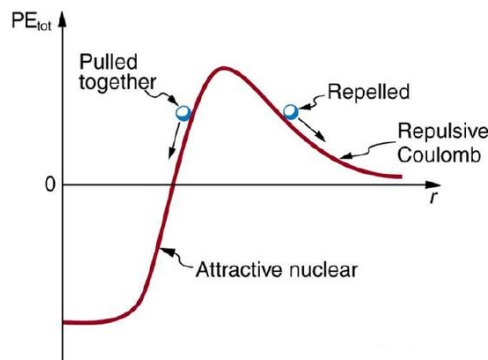
Figure 1.5: Dependance of potential energy on the distance between two nuclei. If the nuclei have enough kinetic energy to get over the Coulomb repulsion hump, they could combine, release energy, and drop into a deep attractive well. Tunneling through the barrier is important in practice. The greater the kinetic energy and the higher the particles get up the barrier, the more likely the tunneling [29].

The magnitude of the Coulomb barrier could be estimated using the following relation

$$V_c = \frac{1}{4\pi\epsilon_0}\frac{Z_1 Z_2 e^2}{R_1 + R_2},$$ (1.3)

19

where Z_1 and Z_2 are the atomic numbers of the two nuclei and R_1 and R_2 are their effective radii. The quantity $R_1 + R_2$ is therefore classically the distance of closest approach. Assuming Enrico Fermi's nuclear distribution for medium nucleous, the radius of a nucleus can be determined via the atomic mass A as,

$$R = r_0 \cdot A^{\frac{1}{3}} \qquad \text{with} \qquad r_0 = 1.21 \ fm, \tag{1.4}$$

then, substituting these approximation in the previous equation gives

$$V_c = \left(\frac{e^2}{4\pi\epsilon_0 \hbar c} \right) \frac{\hbar c Z_1 Z_2}{1.21 \left[A_1^{\frac{1}{3}} + (A_2)^{\frac{1}{3}} \right] fm} \approx 1.198 \frac{Z_1 Z_2}{A_1^{\frac{1}{3}} + (A_2)^{\frac{1}{3}}} \text{MeV}, \tag{1.5}$$

where e is the magnitude of the electric charge carried by a single electron (elementary charge) and $\hbar = \frac{h}{2\pi}$ where h is the Planck's constant. Considering $A_1 = A_2 \approx 2Z_1 = 2Z_2$ with $A \approx 4$, the value of Coulomb potentian is $V_c \approx 1.6$ MeV, which is the energy necessary to overcome the Coulomb barrier and obtain fusion reaction. Although this is a relatively small amount of energy it might be thought that it would be enough accelerate groups of light nuclei, but the only working technic is to provide enough thermal energy to carrying near nuclei, overcoming the Coulomb barrier. Otherwise, approaching nuclei would be elastically scattered. The necessary temperature may be estimated from the relation $E = k_b T$, where $k_b = 8.6 \cdot 10^5$ eV K^{-1} is the Boltzmann's constant and T is the temperature in K. Calculations lead to a temperature of $\approx 10^{10}$ K, which is well above Sun' nucleus temperature (10^8 K). Fusion process is actually possible at less stringent conditions than this estimated temperature due to a combination of two effects. The most important is the phenomenon of *quantum tunneling*, which means that the full height of the Coulomb barrier does not have to be overcome, against classical physics prediction. The probability of barrier penetration depends strongly by the *Gamow factor* ($G(E)$), which depends on the nuclear species of the reaction products. In particular, the probability is exponentially proportional to this factor as

$$G = \sqrt{\frac{E_G}{E}}, \tag{1.6}$$

where

$$E_G = 2 m_r c^2 (\pi \alpha Z_1 Z_2)^2, \tag{1.7}$$

is the *Gamow energy*, $m_r = m_1 m_2/(m_1 + m_2)$ is the the reduced mass and α the Sommerfeld's constant. Anyway, despite the increasing of barrier penetration probability connected with energy increase, it is still small. Therfore, second cause is that fusion occurs at a lower temperature than expected is that a collection of nuclei at a given mean temperature will have a Maxwellian distribution of energies about the mean and so there will be some with energies substantially higher than the mean energy. However the product of the increasing barrier penetration factor with energy and the Maxwellian decreasing exponential actually means that fusion takes place over a rather narrow range of energies. This topics will be discussed in more detail in section 2.2. Therefore, the purpose of a fusion reactor is to obtain the necessary conditions by heating the reactants.

Thermonuclear fusion has been achieved in laboratory, but it is proving exceedingly difficult to create and maintain the required conditions stably and efficiently. This is part of what makes controlled nuclear fusion (NCF) difficult to achieve.

1.2.3 Annihilation

One can say that fission process is less efficient in converting mass into energy than fusion because in the first case there is a lower defect mass which, as previously discussed, is directly proportional to the energy released. However, there is a physics process, known as annihilation, that occurs when a subatomic particle collides with its respective antiparticle to produce other *particles*, such as an electron colliding with a positron to produce two photons. In this case all the inital mass of the particles is converted into energy because the annihilation products do not have mass and could be used to heat a working fluid, which would be expelled to produce thrust.

Actually, all the annihilated mass is converted into energy, but it is not easy to use 100% of this energy release. Although charged and neutral subatomic particles produced have no mass (such as pions), they own great kinetic energy and have small mean life ($\approx 10^{-17}$ s to 10^{-5} s) during which time they would travel significant distances in free space (from tens of meters to several kilometers). Of course, it is essential to contain this energy into a small volume of the engine for as long as it is possible so that the energy is transferred to the working fluid. It has been estimated that the usable amount of energy is represented by the kinetic energy of charged pions which is about 40% of the inital rest mass energy [30]. In order to use antimatter for propulsion purpose it will be necessary to produce large quantities of antiprotons, combining pairs of these with positrons to produce antihydrogen atoms (production efficiency of 17 ± 2 %) [31], which combining in pairs form antihydrogen molecular gas and, finally, condensing this gas into blocks of solid antihydrogen. Moreover it is necessary to store it with strong magnetic fields to avoid its annihilation with the storage material. Both production process and storage technique are extremely complicated and some proposed solutions have been discussed. One can say that the main criticality for this kind of power source is represented by the amount of antimatter required for a modest interstellar mission will be of the order of at least several hundred kilograms.

1.3 Objectives for this thesis work

The first objective for this thesis work is to understand how the direct fusion drive works, starting from the physics behind it and underline the main differences with chemical and electric propulsion solutions and the great advantages related to time travel and payload capability. This required a general analysis on the basics of nuclear fusion processes, which ended up with the thrust generation process inside the direct fusion drive. The main objective was to perform an analysis of trajectories that makes it possible to reach the Saturn's largest moon - Titan for a robotic space mission, which is extremely important to collect precious scientific data that will be discussed later in Sec. 4.3. The spacecraft consists of an orbiter vehicle and an atmospheric probe which will accomplish the mission through the atmosphere and on the surface of Titan. Therefore, characteristics of the

engine and of the scientific objectives were necessary. The calculations presented in this work are supposed to show what kind of missions can be achieved with an engine like the DFD, explaining why it is so attractive.

This thesis work is organized as follows. First of all, a nuclear physics section explains the basics behind a fusion reactor and the possible combination of technology that will make those easier. After that, the physics of the direct fusion drive is presented, along with the thrust generation process and its performances. In the third chapter it is explained the basic approach to orbital mechanics and low thrust trajectory, and also the software used for the trajectory design is presented. This software, Satellite Tool Kit, was necessary to calculate the possible trajectories feasible with the direct fusion drive, because it enabled us to customize the engine and the maneuvers. In the last chapter calculations and results are discussed for missions in which the spacecraft will randezvous with Titan after the Saturn orbit insertion maneuver which allows to begin to study the Saturn system and its magnetosphere and starts the real scientific mission.

2 Nuclear fusion drive

The fusion reaction rate is defined as the number of fusion reactions that occour in the unit time and volume. As mentioned above in Sec. 1.2.2, quantum tunneling and Maxwellian distribution of energies for particles combine to enable fusion process at a lower temperature than might at first be expected. Consequently, fusion process takes place over a rather narrow range of energies because of the proportionality to the Maxwellian distribution and the Gamow Factor, before dealing this topic is necessary to introduce the crucial concept of a cross section for a nuclear reaction.

2.1 Cross section

Every nuclear interaction or reaction take place within a certain probability, which is directly proportional to a cross section σ. In nuclear or subatomic particle physics, the cross section is related to the probability that a given atomic nucleus or subatomic particle will exhibit a specific reaction (for example fusion, fission or scattering) in relation to a particular species of incident particle. Considering two flows of different particles a and b with number densities n_a and n_b (i.e. the number of particles per unit volume, concentration)

$$\dot{N} \ = \frac{dN}{dt} = \ \phi_a \cdot N_b \cdot \sigma_{b_{tot}}. \tag{2.1}$$

where $\dot{N}$ is the number of particles interacting in the unit time, $N_b = n_b \cdot Vol$ the number of target particles and finally $\sigma_{b_{tot}}$ is the total cross section which represents the interaction of all the particles a with the targets b. The cross section is expressed in terms of area, and its numerical value is chosen so that, if the bombarding particle hits a circular area of this size perpendicular to its path and centered at the target nucleus or particle, the given reaction occurs; and, if it misses the area, the reaction does not occur. The reaction cross section is usually not the same as the geometric cross-sectional area of the target nucleus or particle. The unit of reaction cross section is the *barn* equal to 10^{-24} cm^2. Values of cross sections depend on the energy of the bombarding particle and the kind of reaction. Bombarding Boron with neutrons traveling $1,000,000$ cm/s, has a cross section for the neutron-capture reaction of about 120 barns, and the cross section increases to $\approx 1,200$ barns for slow neutrons traveling at $100,000$ cm/s, while boron's cross-sectional area is only about 0.1 barns [32]. In fact, boron is a good absorber of neutrons because of its large cross section and it is usually used as a neutron moderator in many nuclear engineering applications. In contrast, neutrinos emitted in the nuclear reactions that fuel the Sun have cross sections as small as 10^{-21} barns, which accounts for their very low rates of interaction.

2.2 Conditions for achieving fusion

Considering the fusion between two types of nuclei a and b having number densities n_a, n_b, at a temperature T high enough so that the nuclei form a plasma, with uniform values of number densities and T. Leveraging the Maxwell-Boltzmann distribution the velocities

of the two nuclei can be calculated, so that the probability of having two nuclei with a relative speed v in the range v to $v + dv$ is

$$P\left(v\right)dv = \left(\frac{2}{\pi}\right)^{\frac{1}{2}} \cdot \left(\frac{m_r}{k_b T}\right)^{\frac{3}{2}} \cdot e^{\left[\frac{-m_r v^2}{2k_b T}\right]} \cdot v^2 dv, \tag{2.2}$$

where m_r is the reduced mass of the pair. The fusion reaction rate per unit volume is then

$$R_{ab} = n_a n_b \langle \sigma_{ab} v \rangle, \tag{2.3}$$

where the product $n_a n_b$ is the number of pairs of nuclei that can fuse and

$$\langle \sigma_{ab} v \rangle = \int_0^\infty \sigma_{ab} \cdot v \cdot P\left(v\right) dv, \tag{2.4}$$

is the average over the Maxwellian velocity distribution at temperature T. The fusion cross-section may be written as

$$\sigma_{ab}\left(E\right) = \frac{S\left(E\right)}{E} e^{-\left[\left(\frac{E_G}{E}\right)^{\frac{1}{2}}\right]}, \tag{2.5}$$

where the exponential term follows from discussion of the Gamow energy E_G given by Eq.(1.7) and quantum tunnelling mentioned in the previous section and $S(E)$ is the astrophysical factor. $S(E)$ contains the details of the nuclear physics and in most reactions is assumed as constant. The term $1/E$ is conveniently factored out because many nuclear cross sections have this behaviour at low energies. Using Eq.(2.2) and (2.5) in (2.4) gives, from Eq.(2.3):

$$R_{ab} = n_a n_b \left(\frac{8}{\pi m}\right)^{\frac{1}{2}} \left(\frac{1}{k_b T}\right)^{\frac{3}{2}} \int_0^\infty S\left(E\right) e^{\left[-\frac{E}{k_b T} - \left(\frac{E_G}{E}\right)^{\frac{1}{2}}\right]} dE. \tag{2.6}$$

Because the factor $1/E$ has been taken out of the expression for $\sigma(E)$, the quantity $S(E)$ is very slowly varying and the behaviour of the integrand is dominated by the exponential term. With increasing temperature the falling exponential of the Maxwellian energy combines with the rising exponential of the quantum tunnelling effect to produce a maximum in the integrand at $E = E_0$ which can be calculated setting the first derivative equal to zero, in which the greatest number of reactions per unit volume and time occour.

$$E_0 = \left[\frac{1}{4} E_G \left(k_b T\right)^2\right]^{\frac{1}{3}}, \tag{2.7}$$

and fusion occours over a relative narrow range of energies $E_0 \perp \Delta E_0$ [33, 34] where

$$\Delta E_0 = \frac{4}{3^{\frac{1}{2}} 2^{\frac{1}{3}}} E_G^{\frac{1}{6}} \left(k_b T\right)^{\frac{5}{6}}. \tag{2.8}$$

Therefore the range of energy, which determines the range of temperature needed for fusion, strongly depends on Gamow energy E_G.
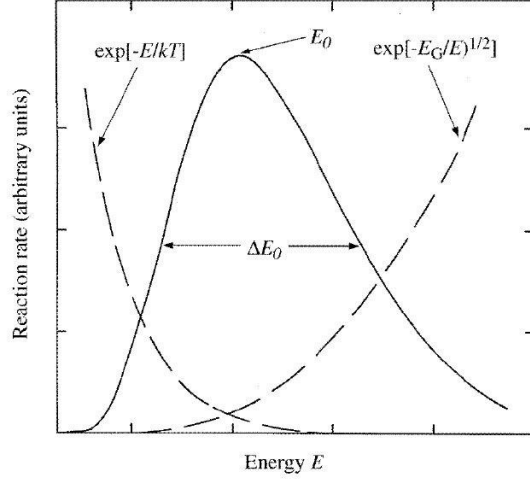
Figure 2.1: Dependance of the reaction rate on the energy E. The dashed curve on the right side is proportional to the barrier penetration factor and the dashed curve on the left to the Maxwell distribution. The solid curve, the combined effect, is proportional to the overall probability of fusion with a peak at E_0 and a width of ΔE_0 [34].

A schematic illustration of combination between these two effects is shown in Fig 2.1. Therefore, the importance of the temperature and the Gamow energy $E_G = 2m_r c^2 \left(\pi \alpha Z_1 Z_2 \right)^2$ is clear. In the approximation where $S(E)$ is taken as a constant $S(E_0)$, the integral in Eq. (2.6) may be solve and gives

$$< \sigma_{ab} v > \approx \frac{8}{9} \cdot S\left(E_0\right) \cdot \left(\frac{2}{3mE_G} \right)^{\frac{1}{2}} \tau^2 \cdot e^{-\tau}, \qquad (2.9)$$

where $\tau = 3 \left(\frac{1}{2} \right)^{\frac{2}{3}} \left(\frac{E_G}{k_b T} \right)^{\frac{1}{3}}$.
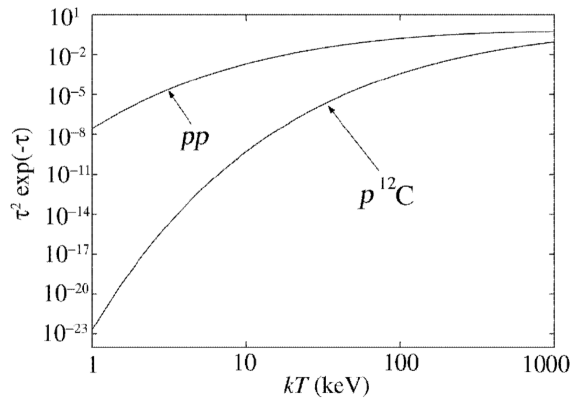
Figure 2.2: The function $\tau^2 exp(\tau)$ for the $p - p$ and $p -^{12} C$ reactions as a function of the temperature [34].

In summary, the rate depends very strongly on both the temperature and the nuclear species because of the factor $\tau^2 \cdot exp[-\tau]$ related to E_G, as shown in Fig. 2.2.

2.3   Energy gain from fusion process

In order to achive controlled thermonuclear fusion, with a positive energy balance, it is necessary to heat a plasma at very high temperatures (≈ 100 *million* °C, more than six times the temperature inside the sun). It is also important to emphasize that plasma must be confined in a limited space for a sufficiently long time such that the energy released by the fusion reactions can compensate for both the losses and the energy used to produce it. The notion just mentioned could be summarized by Lawson criterion conditions [35], which depends on the plasma temperature. As previously said, the kinetic energy which maximizes the reaction rate is

$$E_0 = \left[\frac{1}{4} E_G \left(k_b T \right)^2 \right]^{\frac{1}{3}} \qquad with \qquad E_G = 2mc^2 (\pi \alpha Z_1 Z_2)^2, \qquad (2.10)$$

where the Gamow energy suggests to consider only elements with low Z, otherwise, very high energies are needed, since the increase of Z increases the Coulomb barrier to overcome. Unfortunately, not all the energy released by nuclear reactions is exploitable, because between the products there may be penetrating particles that steal a large amount of energy (such as neutrons) and other not negligible losses, which will discussed in the next sections. For instance, considering deuterium-tritium reaction

$$^2_1 D + \, ^3_1 T \quad \longrightarrow \quad ^4_2 He(3.49 MeV) + n^0(14.1 MeV) \qquad (2.11)$$
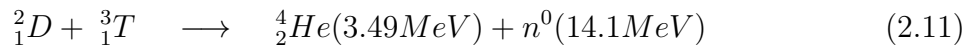
the useful form of energy is only about 3.5 MeV, the kinetic energy of $^4_2 He$ and most of energy is drown by the neutron.

2.3.1   Bremsstrahlung and Synchrotron radiations

Another fundamental aspect concerns radiation losses which occour in nuclear fusion reactions, known as *Bremsstrahlung radiation* (*braking radiation*, or from plasma *free/free radiation*). *Bremsstrahlung* is the radiation given off by a charged particle (often electrons) when deflected by another charged particle (nuclei, protons, etc.), or by an electric field, such as emissions from Coulomb interaction of electrons with the helium nuclei produced in the thermonuclear fusion reactions. More specifically, if the charged particles in motion are decelerated they lose kinetic energy which is converted into radiation. This loss, which is proportional to $Z^2 \cdot \sqrt{T}$, force to work at sufficiently high temperatures in order to have an energy gain, as could be observe in Fig. 2.3. Another unpleasant factor is that at the high temperatures present in a thermonuclear fusion reaction, the production of *Bremsstrahlung* emissions due to electron–electron interactions are very distinct from those resulting from the electron–ion interactions. Although the relativistic effects should not occur and there should not be any electron–electron *Bremsstrahlung* emissions, at high electron velocities this form of radiation could be present.
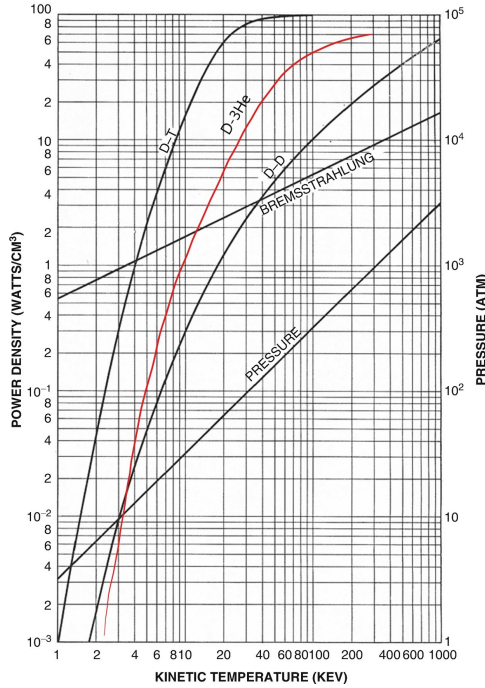
Figure 2.3: Characteristics of thermonuclear fusion reactions and the ideal ignition temperature [36].

In addition to power densities, Fig. 2.3 reveals the pressures at the various temperature stages [36], based on the ideal gas equation $p = (n_i + n_e)k_b T$, where $(n_i + n_e)$ is the total number of particles of nuclei and electrons, respectively, per cm^3 and T is the presentation of kinetic temperature in Kelvin. It is important to note that, although the energy emitted as *Bremsstrahlung* emissions may be lost as far as maintaining the temperature of the thermonuclear reacting system is concerned, it would not be a complete loss in the operating fusion reactor. Zohuri [37] and Glasstone and Lovberg [38] demonstrate that the energy distribution of the electron velocities is Maxwellian or approximately so and dependence of the *Bremsstrahlung* energy emission on the wavelength or photon energy. Another important issue that has to be considered is the so-called Synchrotron radiation, which is the electromagnetic radiation emitted when charged particles are accelerated radially (acceleration perpendicular to the velocity) [39]. High-energy particle machines are usually known as devices into which charged particles are injected into roughly circular orbits for further acceleration or storage and frim which they are eventually ejected. Another aspect comes into play, looking from the side at a charged particle going around in the orbit. Then the accelerator or storage ring behaves like a huge excited antenna. Such an antenna radiates energy according to fundamental laws of physics. This radiation is called Synchrotron radiation, but it is not unique to synchrotrons (it could as well be called betatron radiation) [40].

2.3.2 Lawson criterion

The Lawson criterion is an important general measure of a system that defines the conditions needed for a fusion reactor to reach what is known as ignition temperature, which is the heating of plasma by the products of the fusion reactions to be sufficient to maintain the temperature of the plasma against all losses with external power input [35]. As discussed in section 2.2, the total amount of energy emitted per unit time and unit volume could be obtained by $R \cdot Q = n_1 n_2 \langle \sigma v \rangle$ and represents the power per unit volume. In order to heat plasma and maintain it at temperature T and number density n, which is a concentration, is necessary to provide certain energy

$$\varepsilon_i = \frac{3}{2} n_i k_B T \quad for \ ions(i),$$

$$\varepsilon_e = \frac{3}{2} n_e k_B T \quad for \ electrons(e),$$

where n_i and n_e are concentration of the ions and electrons, respectively. Considering for plasma $n_i = n_e = n$, it results in a total energy $\varepsilon_{TOT} = 3 n k_B T$. In order to meet Lawson criterion, the emission of energy must be greater of the energy supply to maintain plasma temperature and, when enough of that energy is absorbed by the system, it is said to be *ignited* if

$$n_1 n_2 \langle \sigma v \rangle \cdot Q \cdot \tau_E \ > \ 3 \cdot n k_B T. \tag{2.12}$$

The *energy confinement time* $\tau_E = \frac{W}{P - \frac{dW}{dt}}$ measures the rate at which a system loses energy to its environment, where W is the global plasma energy content and P is the applied total heating power. Then, with the assumption of equal particle density of the reactants $n_1 = n_2 = n$ (n plasma number density), Lawson criterion [35] is given

$$n \tau_E > \frac{12 k_B T}{\langle \sigma v \rangle Q}. \tag{2.13}$$

This criterion gives a minimum required value for the product of the particle plasma density such as electron n_e and the energy confinement time τ_E. In the figure below is represented a typical Lawson criterion, or *minimum* value of electron density multiplied by energy confinement time required for self-heating in fusion reactions. To summarize, the temperature at which the reaction rate takes place is proportional to the square of the number density and the time during which confinement can be secured turns out to be limited to a small fraction of a second. Therefore, the density needed in order to achieve a useful power output is very high. Although this criterion has had considerable importance in the past, nowadays the most modern ignition criterion is used. Experiments demonstreted that the Lawson criterion makes too rough approximations on the characteristics of the real processes that take place in a reactor. In the ignition criterion different nature of products is taken into account and bring to the conclusion that is essential to consider not negligible losses, such as neutrons products which cannot help to heat the plasma and other issues.
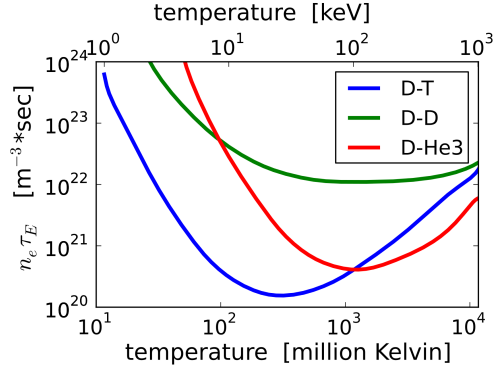
Figure 2.4: Minimum value of $(n_e \cdot \tau_E)$ required for self-heating fusion in the case of D-T, D-D and D-^{3}He nuclear reactions [35].

Finally, another extremely useful figure of merit is the *triple product* of density, temperature, and confinement time $(nT\tau_E)$, also known as fusion product.

$$nT\tau_E \geq \frac{12k_B}{E_{ch}} \cdot \frac{T^2}{\langle \sigma v \rangle}, \tag{2.14}$$

where $E_{ch} \neq Q$ is the energy of the charged fusion products, which can be exploit. Fusion devices must satisfy this fundamental relation, which underline the importance of having both high density and high temperature, and also long enough confinement time. Unfortunately, this threshold has not yet been achieved, although the latest generations of reactors have been improved considerably. In most cases, density and temperature vary quite widely, while pressure beyond a certain threshold remains constant. Then, one can say that fusion power density is proportional to $\frac{p^2 \langle \sigma v \rangle}{T^2}$ and the maximum of fusion power is achievable at T where $\frac{\langle \sigma v \rangle}{T^2}$ is a maximum.
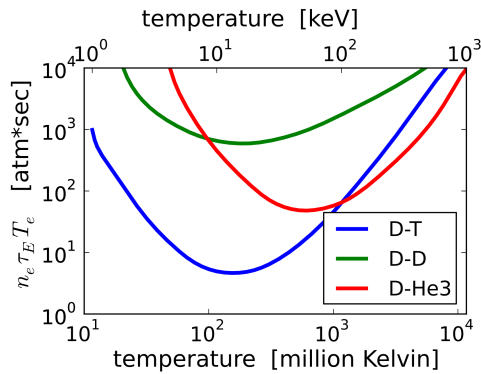
Figure 2.5: The fusion triple product condition for three fusion reactions in the case of D-T, D-D and D-^{3}He nuclear reaction [35].

Moreover, considering magnetic confinement devices, such as Tokamak, τ_E is proportional

to $n^{1/3}P^{2/3}$ and for ignited plasma, the heating power P equal to fusion power, then is proportional to $T^2 n^2$. Therefore, the triple product become proportional to $T^{-1/3}$.

2.4 Basic reactions and Q values

In the previous section Eq. (2.10) reccomends to consider only light elements for the purpose of CNF. Then, the following is a list of fusion reactions which might be considered for thermonuclear power production. Of course, they are exothermic reactions and the energy released Q in MeV is indicated in each case.

$$p + {}_1^2\text{D} \longrightarrow {}_2^3 He + \gamma + 5.49 \text{ MeV}, \tag{2.15}$$

$$\begin{matrix}2\\1\end{matrix}\text{D} + {}_1^2\text{D} \longrightarrow {}_2^4\text{He} + \gamma + 23.85 \text{ MeV}, \tag{2.16}$$

$$\begin{matrix}2\\1\end{matrix}\text{D} + {}_1^2\text{D} \longrightarrow {}_2^3\text{He} \ (0.82 \text{ MeV}) + n^0 \mid 50\%, \tag{2.17}$$

$$\begin{matrix}2\\1\end{matrix}\text{D} + {}_1^2\text{D} \longrightarrow {}_1^3\text{T} \ (1.01 \text{ MeV}) + p \ (3.02 \text{ MeV}) \mid 50\%, \tag{2.18}$$

$$\begin{matrix}2\\1\end{matrix}\text{D} + {}_1^3\text{T} \longrightarrow {}_2^4\text{He} \ (3.49 \text{ MeV}) + n^0 \ (14.1 \text{ MeV}), \tag{2.19}$$

$$\begin{matrix}2\\1\end{matrix}\text{D} + {}_2^3\text{He} \longrightarrow {}_2^4\text{He} \ (3.6 \text{ MeV}) + p \ (14.7 \text{ MeV}), \tag{2.20}$$

$$\begin{matrix}3\\1\end{matrix}\text{T} + {}_1^3\text{T} \longrightarrow {}_2^4\text{He} + 2 \ n^0 + 11.3 \text{ MeV}, \tag{2.21}$$

$$\begin{matrix}3\\2\end{matrix}\text{He} + {}_1^3\text{T} \longrightarrow {}_2^4\text{He} + p + n^0 + 12.1 \text{ MeV} \mid 57\%, \tag{2.22}$$

$$\begin{matrix}3\\2\end{matrix}\text{He} + {}_1^3\text{T} \longrightarrow {}_2^4\text{He} \ (4.8 \text{ MeV}) + {}_1^2 D \ (9.5 \text{ MeV}) \mid 43\%, \tag{2.23}$$

$$\begin{matrix}3\\2\end{matrix}\text{He} + {}_3^6\text{Li} \longrightarrow 2 \ {}_2^4\text{He} + p + 16.9 \text{ MeV}, \tag{2.24}$$

$$\begin{matrix}3\\2\end{matrix}\text{He} + {}_2^3\text{He} \longrightarrow {}_2^4\text{He} + 2 \ p + 12.9 \text{ MeV}, \tag{2.25}$$

$$\begin{matrix}2\\1\end{matrix}\text{D} + {}_3^6\text{Li} \longrightarrow 2 \ {}_2^4\text{He} + 22.4 \text{MeV}, \tag{2.26}$$

$$p + {}_3^6\text{Li} \longrightarrow {}_2^4\text{He} \ (1.7 \text{ MeV}) + {}_2^3\text{He} \ (2.3 \text{ MeV}), \tag{2.27}$$

$$p + {}_5^{11}\text{B} \longrightarrow 3 \ {}_2^4\text{He} + 8.7 \text{ MeV}. \tag{2.28}$$

For some reactions considered, the same reactants result in multiple reactions. In this case the percentage written refers to the likelihood of the reaction to occur, and those

number depends on the cross section of the different reactions. Most of the interacting nuclei, with a few exceptions, are isotopes of hydrogen ($Z = 1$) because this minimizes the Coulomb repulsive force, which hinders fusion. Proton-proton fusion (p-p) is the primary astrophysical reaction, but here is not listed because it occurs at much too slow a rate for it to be considered as a source of thermonuclear power in a spacecraft's reactor. Reactions in Eq. (2.16) and (2.17) have a small cross section and it is not ideal because essentially all the energy output would be carried by gamma rays, which are penetrating. They would escape, taking their energy from the reaction zone, and an external source of power would have to be used to maintain the temperature of the reacting material. However, reactions in Eq. (2.18) and (2.19) are also possible when deuterons interact with each other. These are known as the D-D reactions and are much more likely than either the reactions in Eq. (2.16) or (2.17), they are suitable candidates for fusion process because part of the output energy is carried by charged particles, which can be retained within the reactor to compensate for energy losses and maintain the temperature. Even more promising is the deuteron-triton reaction (D-T), that have a Coulomb barrier similar of D-D, but its cross section is larger. Also there is a much greater release of energy because one of the final products is the very tightly bound α particle. The energy efficiency of the reaction is $17.6/5 = 3.5$ MeVu^{-1}, which is about four times that of uranium fission [35]. Unfortunately, it requires tritium as a fuel component, which is radioactive and would have to be produced in a fusion reactor since it does not occur naturally. Reaction 6 is attractive because it also has a high Q value and both final products are charged (aneutronic reaction), which makes it relatively easy to contain more of the energy in the reactor if required. Also, the fuel is not radioactive, no neutrons are produced which, in D-T reactor will produce some radioactivity. The disadvantage is the higher Coulomb barrier and the reactor temperature to achieve a given reaction rate, using a D-^{3}He mixture, would need to be about six times higher than in a D-T reactor. More specifically, the reactions are the following:

1. **tritium - tritium**

$$^3_1\text{T} + \, ^3_1\text{T} \; \longrightarrow \; ^4_2\text{He} + 2 \, n^0 + 11.3 \text{ MeV},$$
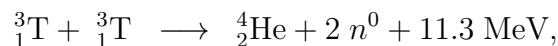
   This is a relatively simple reaction to obtain, where two neutrons are produced per fusion reaction. Another problem is related to the fact that tritium half-life is about 12 years, rendering unfit for long-term missions.

2. **deuterium - tritium**

$$^2_1\text{D} + \, ^3_1\text{T} \; \longrightarrow \; ^4_2\text{He} \, (3.49 \text{ MeV}) + n^0 \, (14.1 \text{ MeV})$$

   As of 2008, the United States Department of Energy (DOE) and other federal agencies have spent approximately USD 18 billion [41] on energy devices using the fusion reaction between deuterium and tritium (such as Tokamak). The hydrogen isotope deuterium (with one "extra" neutron) collides with the tritium (with two "extra" neutrons) to form an alpha particle (a helium nucleus) and a neutron. The energy required to make the D–T reaction happen is lower (in keV) than the energy

required for any other nuclear fusion reaction and at the proper activation energy, it is much more likely to happen than any other fusion reaction. Unfortunately, there are also a several disvantages:

- tritium is both radioactive and expensive to produce (although it is a naturally occurring radioactive form of hydrogen produced by cosmic rays in the atmosphere);
- This kind of reaction has low efficiency due to highly energetic neutrons, in addition to the problem related to the half life of tritium. The neutrons released can damage material walls and make some materials radioactive.

3. **helium-3 - tritium**

$$^3_2\text{He} +^3_1\text{T} \longrightarrow {}^4_2\text{He} + p + n^0 + 12.1 \text{ MeV} \mid 57\%,$$

$$^3_2\text{He} +^3_1\text{T} \longrightarrow {}^4_2\text{He} \ (4.8 \text{ MeV}) +^2_1\text{D} \ (9.5 \text{ MeV}) \mid 43\%.$$
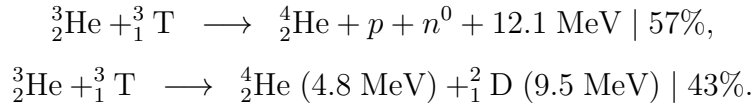
The likelyhood of the reaction to occurr with the exact same reagents is represented by the percentage beside. Similar considerations are possible as for reactions (2.20) and (2.22) with tritium.

4. **deuterium - helium-3**

$$^2_1\text{D} +^3_2\text{He} \longrightarrow {}^4_2\text{He} \ (3.6 \text{ MeV}) + p \ (14.7 \text{ MeV})$$
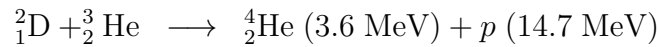
In this reaction no neutrons are produced and all products are ionized particles that could be used in a reaction drive, by the use of electromagnetic fields. These characteristics improve system performance by providing a larger fraction of energy in charged particles going to the thrust-nozzle and by drastically reducing neutron induced damage to structural components. There are two main problems related to this reaction:

- Never achieved fusion with D-^{3}He until now;
- ^{3}He is a rare element on Earth.

5. **helium-3 - lithium-6**

$$^3_2\text{He} +^6_3\text{Li} \longrightarrow 2 \ ^4_2\text{He} + p + 16.9 \text{ MeV}$$
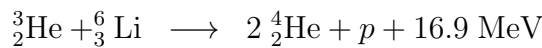
Since it requires lithium-6, the main problem is the poor availability. ^{6}Li is an isotope of lithium, which represents about 8% of all lithium resource.

6. **deuterium - deuterium**

$$^2_1\text{D} +^2_1\text{D} \longrightarrow {}^3_1\text{T} \ (1.01 \text{ MeV}) + p \ (3.02 \text{ MeV}) \mid 50\%,$$

$$^2_1\text{D} +^2_1\text{D} \longrightarrow {}^3_2\text{He} \ (0.82 \text{ MeV}) + n^0 \mid 50\%.$$
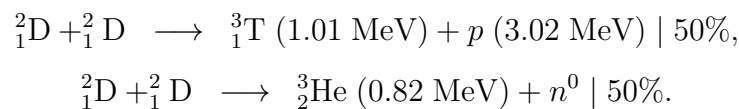
The possible reaction (2.18) produces a neutron that leads to loose around 30% of the energy generated. The main advantage related to this solution consists in the great availability of deuterium and its low production cost.

7. **deuterium - lithium-6**

$$^2_1 D + ^6_3 Li \quad \longrightarrow \quad 2 \, ^4_2 He + 22.4 \text{ MeV},$$

$$^2_1 D + ^6_3 Li \quad \longrightarrow \quad ...$$
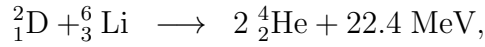
Although this reaction could lead to 4 different kind of products, only the first is relevant. The great part of energy is released along with 2 alpha particles, hence it is ideal for a direct drive engine. The disadvantages are the shortage of ^{6}Li and the fact that the secondary reactions, which come along with the first one, produce neutrons.

8. **proton - boron-11**

$$p + ^{11}_5 B \quad \longrightarrow \quad 3 \, ^4_2 He + 8.7 \text{ MeV}$$
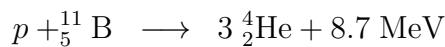
The products are again alpha particle, but the Coulomb barrier is higher than the previous reactions considered, requiring higher temperatures in order to achieve fusion. Although boron-11 is quite uncommon on Earth, an interesting characteristic is the possibility to store it in a solid state.

2.4.1 Nuclear fusion resources

As just mentioned, a complication for nuclear propulsion is represented by the lack of resources on Earth necessary for some of the nuclear reactions detailed above. In particular, taking into account the promising D-^{3}He reaction, it is worth noting that unfortunately there are several issues to be solved. Firstly, ^{3}He available in Earth's atmosphere is extremely limited, although it is immune to natural chemical processes, and is a stable nuclide, which is both primordial and also continually produced in the sun, its abundance is about $1/10,000$ that of ^{4}He. The partial pressure of helium in the Earth's atmosphere is about 0.52 Pa, therefore helium accounts for 5.2 *parts per million* of the total pressure ($\approx 10^5$ Pa) in the Earth's atmosphere, and ^{3}He thus is present with a concentration of 7.2 *parts per trillion*. Furthermore, is very expensive to produce (millions of dollars per kg), from the radioactive decay of tritium (half-life of 12.3 years) that has been produced in nuclear fission reactors. Suffice it to say that since 1955 only 150 kg of non-radioactive isotope of ^{3}He has been obtained from US production [42] and roughly only 30 kg of ^{3}He exist in human hands at the moment [43]. The scarcity of naturally occurring ^{3}He is due to low level production by processes that occour on Earth such as the already mentioned beta decay of tritium, solar wind or spallation of new nuclei caused by bombardment with energetic nuclear particles, such as cosmic rays through the atmosphere. Moreover, ^{3}He emission from the mantle to the atmosphere has been estimated to be 4.2 atom/cm^2−s or 3 kg/year for the entire Earth's surface [44] and is not simple to collect. Nowadays, the total estimated amount in Earth's mantle may be from $100,000$ tonnes to 1 *million* tonnes, but most of it is not accessible and it has been predicted that extracting this precious gas from these sources consumes more energy than fusion would release, by a ratio of 10 to 1 [45]. A possible solution could be to exploit resources present in our Solar System. Actually, there is a closer large source of relatively easily extractable ^{3}He on the lunar surface that have been deposited by solar wind. Apollo lunar samples and analysis

made by space probes indicate that the moon's surface soil, which has been receiving solar wind particles for more than $4 \cdot 10^9$ years, contains 10^9 kg of ^{3}He. The lunar surface is covered by *regolith*, a layer of loose which includes dust, soil, broken rock, and other related materials. Its extremely fine grain size(μm), due to constant meteorite impact, makes it an effective ^{3}He collector. It is important to note that solar wind particles are braked by *regolith* granules to a depth of μm. Consequently, a great amount of ^{3}He is presented in the outermost layer of lunar soil and in particular, soils of the lunar *maria* have a higher helium content than soils in the highlands because the solar wind particles appear to be concentrated in ilmenite granules ($FeTiO_3$) [45, 46].

Many studies were conducted to determine the economic viability of mining the moon for ^{3}He taking into account the energy cost required to produce it from lunar soils and also dollars of profit. Other solutions are represented by gas giants such as helium-rich atmosphere of Jupiter and Saturn or Neptune [43].

3 Main features of nuclear propulsion

There are many missions that can be accomplished with a small amount of ^{3}He from terrestrial sources, and enormous reserves are available on the moon for future missions. As discussed in Sec. 1.1.2, there are many studies about several projects, which are focused on controlled nuclear fusion (CNF), to propel a spacecraft. As seen, in order to generate thrust with nuclear fusion, is necessary to heat greatly a working fluid and consequently to handle an extremely hot plasma, meaning a fully ionized gas, a sea of positive ions and negative electrons. These essential high temperatures involved in this process lead to a series of engineering issues that have to be addressed.

3.1 Heating methods

As precedently discussed, heating is required because the positive fuel ions repel each other and increasing temperature thermal velocity increases let them to become close enough for the fusion reactions to occur. There are different heating methods used on Earth for fusion and usually, several of them work concurrently to bring the plasma in the core of the machine to extremely high temperature, such as the international thermonuclear experimental reactor (ITER) ($150,000,000$ °C). One way, known as ohmic heating, via magnetic fields generate high intensity current through plasma. Therefore collisions with energized electrons and ions create a sort of resistance, then heat and consequently an increase of temperature. Unfortunatly, as the temperature of the plasma rises, this resistance and therefore the heating effect decreases, resulting in a limit of heat obtainable. In order to obtain higher temperatures and reach the threshold where fusion can occur, two types of heating methods complement ohmic heating and must be applied from outside of the fusion device. neutral beam injection and high-frequency electromagnetic waves, Neutral beam injection (NBI) consists in a beam of high energy neutral particles that can reach the plasma penetrating the magnetic confinement which will be discussed in next section. From outside, charged deuterium particles can be accelerated to the required energy level. These accelerated ions then pass through an "ion beam neutralizer" where their electrical charge is removed. The high velocity neutral particles can then be injected into the heart of the plasma where, by way of rapid collision, they transfer their energy to the plasma particles. When these neutral particles are ionized by collision with the plasma particles, they are kept in the plasma by the confining magnetic field, and can transfer most of their energy by further collisions with the plasma. This technique overcomes the limitation previously mentioned delivering millions of watts to the plasma, reaching temperature closer to the threshold.

Another solution provides for the use of high frequency electromagnetic waves, where the energy carried by high-frequency waves introduced into the plasma is transferred to the charged particles, increasing the velocity of their chaotic motion. Following this principle three types of waves will be employed in ITER, each matching a frequency of plasma ions and electrons in the interior of the ITER machine to maximize heat transfer. As precedently mentioned, these three different methods often work together in nuclear fusion devices to bring the plasma to a temperature where fusion can occur. Moreover, the current purpose of several research is to obtain a "burning plasma", in which the energy of

the fusion products is enough to maintain the temperature of the plasma, so that external heating can then be strongly reduced resulting in a decrease of external power demand. In order to achieve the fusion power generation is crucial the idea of a burning plasma where more than 50% of the energy to drive the fusion reaction is self-produced. A self-maintained plasma, where all necessary energy to maintain fusion conditions is produced internally, is termed *in ignition*. Another operational condition is called *break even* and it happens when the total power generated by the plasma is equal to the external heating power.

3.2 Confinement methods

The heating of the plasma and the great energy released by the fusion process means that very high temperatures are reached, as it happens in the nuclei of the stars. It is not technologically feasible to design walls of the reactor that contains this extremely hot plasma with contact, regardless of the material choice. Therefore, it is necessary to recreate vacuum condition and the plasma must be confined in some way. Even the stars, exploiting gravity, likewise confine their plasma. Unfortunately, this efficient method is infeasiblel due to the enormous mass demand necessary to obtain such intense gravitational forces. It is clear that perfect containment of a fusion plasma is impossible and is very important the design of components which are in line of sight of the hot plasma, that are called plasma-facing components (PFCs or materials PFMs) and interact with the plasma edge. There are several techniques:

Inertial confinement fusion (ICF) is one of two major branches of fusion energy research: high-energy beams of laser, electron or ions can compress and heat a small fuel pellet to extremely high density, such as 1030 ions/m^3 (almost all ICF devices have used lasers).
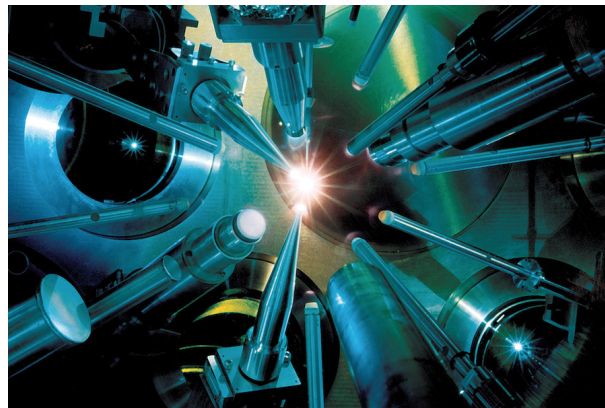
Figure 3.1: Inertial fusion confinement: The Omega laser's 40 kilojoule output is used to crush hydrogen pellets and initiate nuclear fusion, Credit: University of Rochester, USA.

The heated outer layer explodes, producing a reaction force against the inner one, accelerating it inwards and compressing the target. Consequently, shock waves are generated and if sufficiently powerful they can compress and heat the fuel at the center obtaining

fusion conditions. Inertia limits the expansion rate of the compressed fuel plasma, providing confinement for times $\smile 1 \; ns$, which is sufficient for ignition and fusion to occur. In the direct-drive method of inertial confinement fusion, laser beams directly strike the fuel pellet. An alternative approach is represented from the indirect-drive method, in which the laser light is first converted into x-rays in a gold enclosure called a *hohlraum*, as shown in Fig. 3.2, and then achieve fusion ignition heating and compressing the fuel. Symmetrically compressing the capsule with radiation forms a central "hot spot" where fusion processes start in the plasma ignites and the compressed fuel burns before it can disassemble.
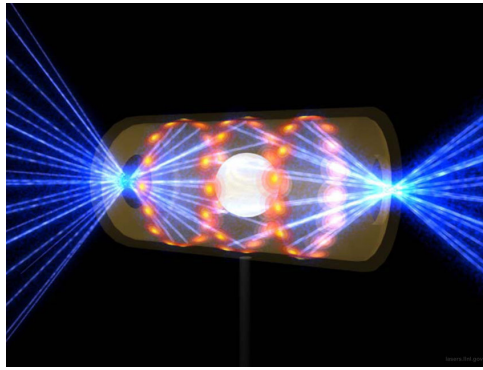
Figure 3.2: In the "indirect drive" method, the lasers heat the inner walls of a gold cavity containing the pellet, creating a superhot plasma which radiates a uniform "bath" of soft X-rays. The X-rays rapidly heat the outer surface of the fuel pellet, causing a high-speed ablation, or "blowoff," of the surface material and imploding the fuel capsule in the same way as if it had been hit with the lasers directly [47].

Scientists have made significant progress in understanding the physics and developing innovative approaches to indirect drive fusion, although *ignition* has not yet been completely achieved. The other fundamental method is the magnetic confinement fusion. This approch exploits the Lorentz force resulting from the interaction between magnetic fields and the charged particles that compose plasma. The Lorentz force is

$$\mathbf{F_L} = q\mathbf{v} \times \mathbf{B}, \tag{3.1}$$

where, $\mathbf{v}$ is the velocity of the charged paricle and $\mathbf{B}$ is the magnetic field. As well known, this force causes electrons and ions to spiral around magnetic field lines and prohibits them from easily penetrating across the reactor. The property of charged particles to cover helical paths around the magnetic field lines, reppresents the basis of magnetic confinement methods. There are some important magnetic effects that have to be considered for plasma confinement. Assuming infinite conductivity, the magnetic field lines can be considered glued to the fluid, so, if the fluid does moves, even the field lines will move and vice versa. Otherwise, there may be a relative motion between fluid and field lines (diffusion effect). This is a very important phenomenon that affects all machines that employ magnetically confined plasmas. The physics behind it concern the rate of collisions related to plasma motion, from which the resistivity of a plasma depends. If no

collisions happen, the resistivity would be zero and the more frequent the collisions are, the higher resistivity is. When a particle collides, its spiral motion is abruptly interrupted and resumes shifted to another magnetic field line. Then, it is easy to realize that, due to the collisions, a progressive expansion will occur in directions perpendicular to the magnetic field lines. Therefore, plasma diffusion through magnetic field lines represents a loss, which must absolutely be contained in order to achieve fusion process and is directly proportional to resistivity and strongly drops as the magnetic field increases.

Starting from the Navier-Stokes equations [48], the equations of magnetohydrodynamics (MHD) are obtained, by adding the magnetic terms:

$$\mathbf{J} \times \mathbf{B} = \nabla p, \tag{3.2}$$

$$\nabla \times \mathbf{H} = J, \tag{3.3}$$

$$\nabla \cdot \mathbf{B} = 0. \tag{3.4}$$

MHD allows to study the equilibrium conditions of a magnetically confined plasma. From these relations, it is possible to obtain the following balance of pressures equation:

$$\nabla \left(p + \frac{B^2}{2\mu_0} \right) = \frac{1}{\mu_0} \left(\mathbf{B} \cdot \nabla \right) \mathbf{B}. \tag{3.5}$$

The magnetic pressure $\frac{B^2}{2\mu_0}$, which is the density of magnetic field, plays the same role as the fluid pressure p, but is carried by the magnetic field rather than by the kinetic energy of gas molecules. One can say that if the magnetic field lines have no curvature, the right term in the Eq. (3.5) is zero and the relation becomes:

$$\nabla \left(p + \frac{B^2}{2\mu_0} \right) = 0. \tag{3.6}$$

Then, it is easy to understand that with this assumptions the total pressure, which is the sum of ordinary pressure p and magnetic pressure $\frac{B^2}{2\mu_0}$ is constant moving in space. It is possible to demonstrate that the pressure gradient is perpendicular to both $\mathbf{J}$ and $\mathbf{B}$, therefore

$$\mathbf{J} \cdot \nabla p = 0, \tag{3.7}$$

$$\mathbf{B} \cdot \nabla p = 0. \tag{3.8}$$

From the latter equation it is clear that the pressure must be constant along the magnetic field lines and both magnetic field and current lines lie on isobaric surfaces (magnetic surfaces). Thus, these isobaric surfaces (perpendicular to ∇p) are both "magnetic surfaces" and "current surfaces". As well known, since both $\mathbf{B}$ and $\mathbf{J}$ have divergence-free (solenoidal vectors), the magnetic and current lines stretch to infinity or are closed lines and considering a finite volume of plasma this surfaces are closed and nested one inside another. It can be demonstrated that, if the variations are quite gradual and $\mathbf{B} \neq 0$, $\mathbf{J} \neq 0$ in this finite volume, the magnetic surfaces assume the form of toroids. The pressure increases moving from the outside towards the axis and the currents are such that the force $\mathbf{J} \times \mathbf{B}$ is directed towards the axis. The important fact then is that a plasma

can be confined entirely by magnetic forces and if a plasma with $\nabla p = 0$ is in equilibrium condition with a $\mathbf{B}$ applied from the outside, a current J must necessarily be generated in the plasma compatible with $\nabla p = \mathbf{J} \times \mathbf{B}$ which accounts, on a macroscopic scale, of the effect of diamagnetism, for which the internal field is weaker than the external field. This current is known as diamagnetic current and it can be calculated from the Eq. (3.2) by multiplying $\mathbf{B}$

$$\mathbf{B} \times \nabla p = \mathbf{B} \times (\mathbf{J} \times \mathbf{B}), \tag{3.9}$$

obtaining the perpendicular component $J_\perp$ ($J_\parallel = 0$)

$$J_\perp = \frac{\mathbf{B} \times \nabla p}{B^2}. \tag{3.10}$$

This current can be experimentally measured and provides a measure of the internal energy of the plasma (∇p).

3.2.1 Magnetic mirror

Plasma particles are influenced by magnetic mirror effect, a configuration of the magnetic field in which the intensity of the field changes in parallel, along the field line. Charged particles, within a limited range of velocities and angles of approach, experience an increasing force that eventually causes them to reverse direction and return to the confinement area. Then under certain requirements, the particles are confined to the region with the less intense magnetic field: for this reason one of these configurations are also called *magnetic bottles*.
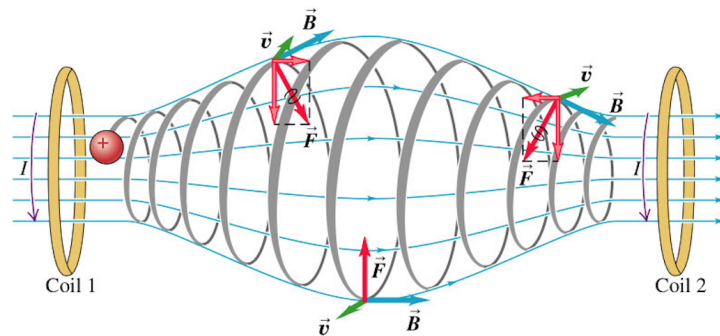
Figure 3.3: Schematic illustration of a basic magnetic bottle machine including a charged particle's motion. Sometimes it is possible to find rings in the centre which extend the confinement area horizontally, but are not strictly needed.

One can say that according to the kinetic energy conservation law with increasing $\mathbf{B}$ the parallel velocity must decrease. In practice, as the particle advances towards the

more intense magnetic field regions, the velocity component parallel to the field line decreases, while the perpendicular increases. Then it could happens a critical situation in which the parallel velocity disappears, and the particle is rejected back towards the region with the smallest magnetic field. Unfortunately, charge particles with a pitch angle smaller than a critical angle pass are not arrested. The fact that, for a given magnetic configuration there is always a cone of loss, was the reason why magnetic bottles configurations were abandoned as early as 1980. However, considering the second coil of the Fig. 3.3, it is important to take into account another aspect related to the same principles just mentioned, that forms the basis of magnetic nozzles. The carghed particles, which have enough energy to overcome the magnetic mirror, are magnetically accelerated. A divergent magnetic field is used to convert the thermal energy of the plasma into kinetic energy. Thanks to the nozzle, the plasma flow is expanded. Being **B** divergent, the density of the field decreases and consequently there is an increase in the axial energy of the plasma $(v_\parallel)$ at the expense of the rotational motion of the particles, meaning a decrease of $v_\perp$.
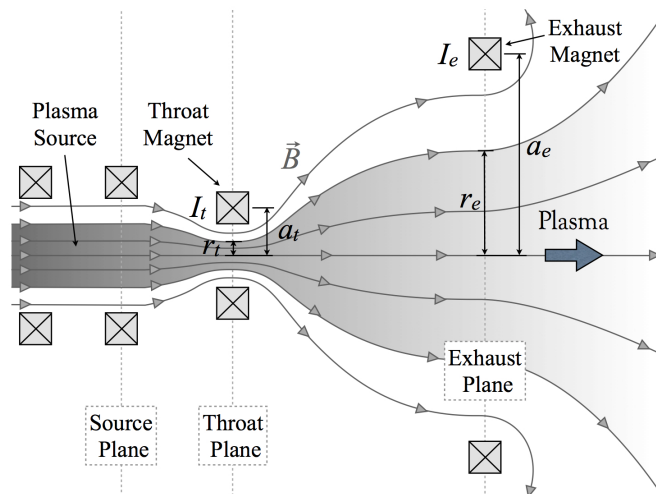
Figure 3.4: A magnetic nozzle showing the magnetic field strength along the axis of the nozzle. Currents in the field coils generate the magnetic field **B** and the related magnetic forces act on the plasma and allow to generate thrust [49].

Furthermore, the magnetic field allows to confine the hot plasma away from the walls of the magnetic nozzle, which represents a valid instrument of acceleration of a plasma since not require the presence of electrodes, which are components prone to deteroration and limit the life of the engine.

3.2.2 Pinch effect

The pinch effect consists of the interaction between the current that constitutes a generic electric arc **J** and the magnetic field **B**, induced by the current itself. There are different pinches in litterature that differ in their geometry and operating forces, considering cylindrical geometry for example:

θ-**pinch:** A discharge tube inserted in a solenoid constituted by a series of coils or simply constituted by metallic conductor, with a strong rapidly variable current, obtained by the discharge of a bank of capacitors. In the ideal case of infinite solenoid which, as is known, produces a constant axial magnetic field with straight lines of force along the axis of the solenoid, the time-variable axial magnetic field B_z, induces an azimuthal currents (J_θ) in the plasma, which flow in the opposite direction to those that pass through the coil.
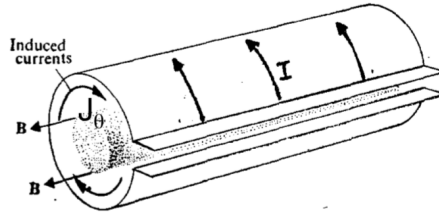
Figure 3.5: Represantation of θ-pinch effect, in the ideal case of infinite solenoid which, produces a constant axial magnetic field with straight lines of force along the axis of the solenoid.

Assuming that the plasma behaves like a perfectly conductive fluid with constant kinetic pressure, $\mathbf{B_z}$ appears only in the region between the plasma and the metallic conductor, since it cannot penetrate the plasma, for the conservation of the magnetic flux inside the fluid. Then, on the plasma surface an azimuthal diamagnetic current is generated, which compresses (pinch) the fluid until magnetic and kinetic pressure are equal

$$\beta = \frac{P}{\left(\frac{B_0^2}{2\mu_0}\right)} = 1. \tag{3.11}$$

Therefore, β_θ is a measure of the system's ability to confine a plasma having a certain kinetic pressure (or temperature). Actually, the magnetic field penetrates (or diffuses) part of the plasma, due to its finite conductivity, which diffuses through the magnetic field lines. In a real case there will be diffusive effects, with a generally increasing kinetic pressure and a decreasing magnetic pressure towards the center of the solenoid. Using the MHD equations for a cylinder of infinite length

$$(J \times B)_r - (\nabla p)_r = 0, \tag{3.12}$$

$$(\nabla \times B)_\theta = (\mu_0 J)_\theta, \tag{3.13}$$

and because of symmetry it is possible to consider that $\mathbf{B}$ has only one axial component, $\mathbf{J}$ has only one azimuthal component and ∇p has only radial component

$$J_\theta B_z - \frac{\partial p}{\partial r} = 0, \tag{3.14}$$

$$-\frac{\partial B_z}{\partial r} = \mu_0 J_\theta, \tag{3.15}$$

then

$$\frac{\partial}{\partial r}\left(\frac{B_z^2}{2\mu_0} + p\right) = 0. \tag{3.16}$$

Therefore,

$$\frac{B_z^2}{2\mu_0} + p = const = \frac{B_{z_{ext}}^2}{2\mu_0}. \tag{3.17}$$
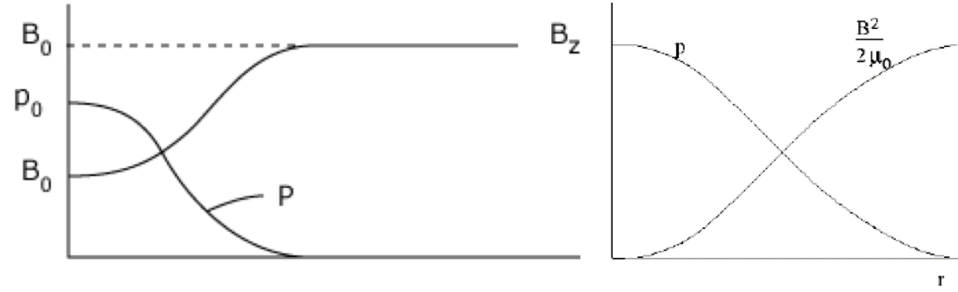
Figure 3.6: θ-pinch effect: The dependance of pression and magnetic field magnitude on the radial distance are shown. It is possible to observe the maximum value of pression in the center of the solenoid and the higest value of B_z related to the maximum radius.

Z-pinch: A type of plasma confinement system, based on the Lorentz force, Eq. (3.18), that uses axial electrical current in the plasma to generate the azimuthal magnetic field that compresses it.

Screw pinch: A combination of a Z-pinch and θ-pinch (stabilized Z-pinch).

Taking into account the Z-pinch effect, it is clear that $\mathbf{B}$ is self-induced, r_1 is the radius of the arc and as already mentioned, the magnetic field generates the Lorentz force

$$\mathbf{F_L} = q\mathbf{v} \times \mathbf{B}, \qquad \mathbf{f} = n\mathbf{F} = \mathbf{j} \times \mathbf{B}. \tag{3.18}$$

Assuming that the charge density j is uniform on the arc area $j = \frac{J}{\pi r_1^2}$ and a stationary magnetic field, therefore it is possible to apply the Ampére-law from a path integral along a circumference of radius r

$$\int_l \mathbf{B} \cdot u dl = \mu J_c, \tag{3.19}$$

where J_c is the concatenated current. Solving the integral

$$B \cdot 2\pi r = \begin{cases} \mu J \cdot \frac{r^2}{r_1^2} & \text{for } r < r_1, \\ \mu J, & \text{for } r > r_1. \end{cases} \tag{3.20}$$

then substituting $\mathbf{J}$

$$B = \begin{cases} \frac{\mu}{2}jr & \text{for } r < r_1, \\ \frac{\mu J}{2\pi r} & \text{for } r > r_1. \end{cases} \qquad (3.21)$$
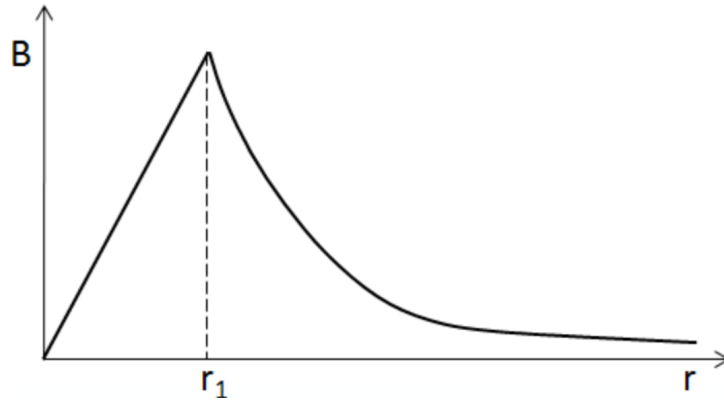
Figure 3.7: Intensity distribution of the magnetic field induced by the electrical current along the radial direction r, where the parameter r_1 refers to the radius of the arc.

The magnetic force is given by

$$\mathbf{f_B} = \mathbf{j} \times \mathbf{B} = \begin{cases} \frac{\mu}{2}j^2r & \text{for } r < r_1, \\ 0 & \text{for } r > r_1 (j = 0). \end{cases} \qquad (3.22)$$

This force generated by the magnetic field self-induced by the arc current compress the arc itself and create a strong pressure gradient between the edge and the center of the current.
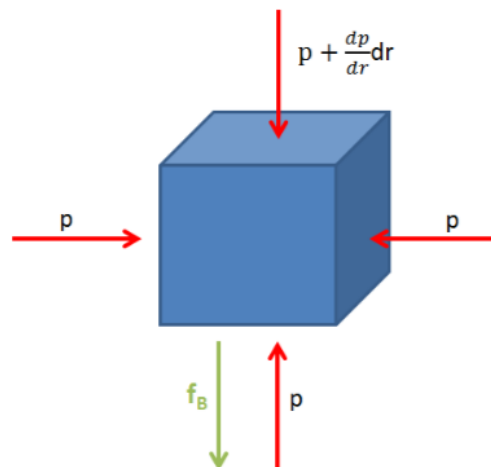
Figure 3.8: The balance of forces for an infinitesimal booklet within the arc

43

Considering an infinitesimal booklet within the arc

$$-\frac{dp}{dr} = f_b = \frac{\mu j^2}{2} r, \tag{3.23}$$

and integrating

$$p - p_{ext} = \frac{\mu j^2}{4}\left(r_1^2 - r^2\right) = \frac{\mu j^2}{4\pi}\left[1 - \left(\frac{r}{r_1}\right)^2\right]. \tag{3.24}$$

Therefore the qualitative trend of the pressure inside the arc is shown in the following graph
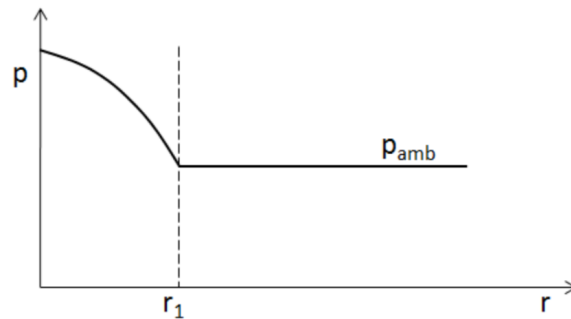
Figure 3.9: The pression distribution within the electric arc.

The pinch effect keeps the current particles in the central area, away from the walls but unfotunately it is a self-sustaining phenomenon that is unstable. This instability is due to the fact that if the pressure increases, the conductivity also increases and result in an instability known as *sausage*, where the pressure increase leads to an increase of current J and consequently to an increase in the intensity of the magnetic field.
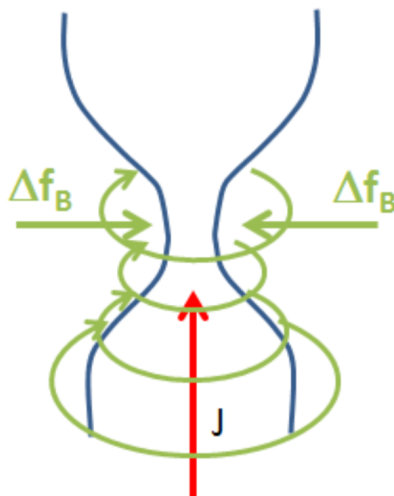
Figure 3.10: Simple representation of the so-called sausage instability that in the worse cases results in the exhaustion of the arc itself [4].

Then, the stronger magnetic forces bring the transversal section of the arch to be drastically reduced, until it closes.

Another important instability, commonly known as *kink* is a current-driven plasma instability characterized by transverse displacements of a plasma flow's cross-section from its center of mass. If a *kink* arise in a column plasma, the magnetic forces on the inside of the kink become larger than those on the outside, which leads to growth of the perturbation.
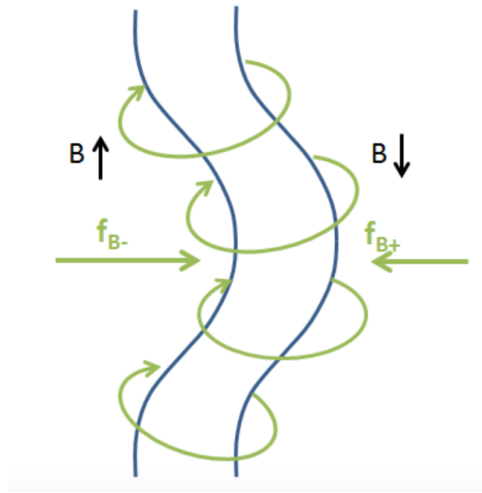
Figure 3.11: Schematic representation of the so-called kink instability that in the worse cases results in the exhaustion of the arc itself [4].

Unfortunately, other several instabilities could also be present, such as tilt mode instability, then it is clear that plasma stability is a crucial issue in the study of every plasma device, and it determines if the perturbations will grow, oscillate, or be damped. However, a plasma can be treated as a fluid (in many cases) and it is possible to analyze its stability with magnetohydrodynamics theory (MHD). Criteria that determine whether a magnetized plasma is fluid-like are the ratio of particle gyro-radii to machine size and collisionality. Fluid-like plasmas are highly collisional, cold and dense and it is also true when the ion gyro-radii, ρ_i, are small compared to the plasma radius, r_s. Several technical solutions have been developed, such as constrictor, application of corrective magnetic fields, swirl motion, and others are under study.

3.3 Magnetic confinement concepts

First magnetic confinement machines were based on the fact that an electric current generates a magnetic field (Biot-Savart law), and that the currents flowing in the plasma will "pinch" the plasma, containing it within its own magnetic field. This magnetic field wrapped around the plasma (current) in what is called the poloidal direction which is illustrated in Fig. 3.12. In a pinch experiment the plasma current flows around inside the torus (toroidal direction) and generates a magnetic field wrapped around the plasma (poloidal direction).
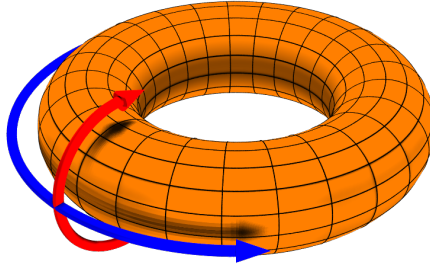
Figure 3.12: Schematic illustration for the poloidal (red arrow) and toroidal (blue arrow) directions around a *torus*.

Considering circular magnetic field lines, as in a torus, then the plasma can, in principle, be well confined, although many phenomena can destroy confinement. Starting from this idea, Russian scientists conceptualized the Tokamak, a toroidal shape device which confine the hot plasma in a vacuum vessel by means of powerful magnetic fields which keep it away from the machine walls.
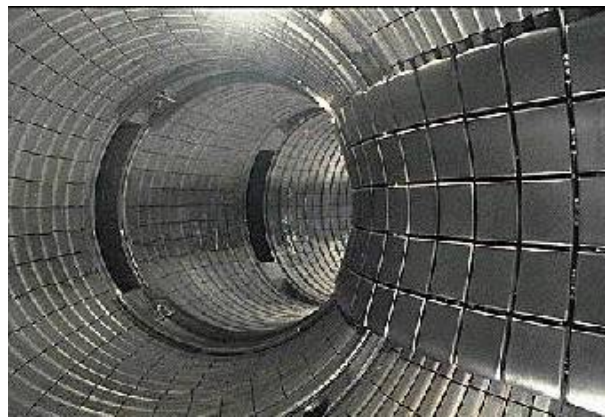
Figure 3.13: View of the innner structure of the Frascati Tokamak Upgrade (FTU) operating at Frascati, Italy [50].

A plasma current is induced by a central solenoid transformer, with the central magnetic coil acting as the primary winding and the plasma as the secondary winding. There are three different types of magnetic fields that provide confinement and stability to the plasma: a poloidal magnetic field, created by the plasma current itself and other two magnetic fields applied externally. The combination of two sets of magnetic coils (toroidal and poloidal coils) creates a field in both vertical and horizontal directions, acting as a magnetic "cage" to hold and shape the plasma.
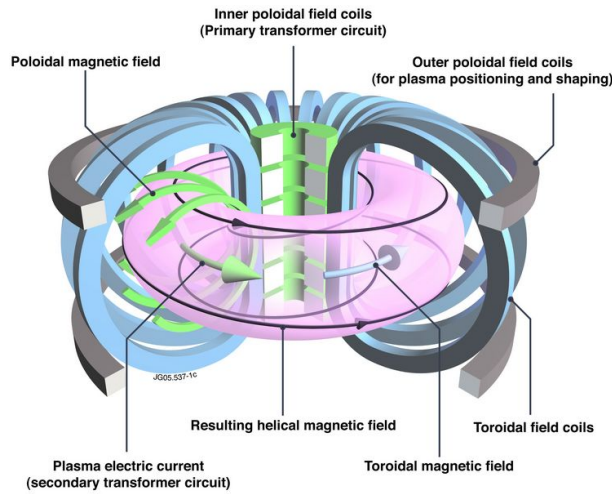
Figure 3.14: Magnetic fields involved in a Tokamak device. It is possible to observe the inner and outer poloidal field coils (green) which generate a magnetic cage to confine and shape the plasma.

The first ensures the balance of the plasma while the second, generated by means of toroidal coils, allows to generate a direct field around the symmetry axis of the torus that constrains the charged particles to flow along that direction. The third, generated by means of coils, allows the position control of the plasma. In 1951, Princeton astrophysicist Lyman Spitzer Jr. guessed a process for confining hot, charged plasma gas inside magnetic fields in a figure-eight shaped device that came to be called a *stellarator*. Unlike the zeta pinch machine, a type of confinement where the magnetic field was generated mainly by currents flowing in the plasma itself, the magnetic field in the *stellarator* was produced entirely by external coils.
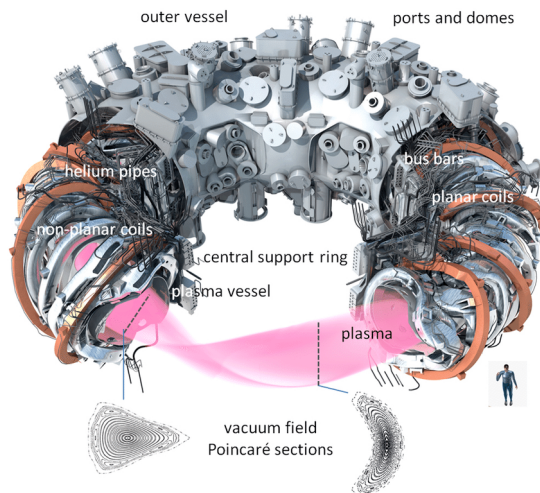
Figure 3.15: High-detailed scheme of the superconducting stellarator-Wendelstein-7-X (Germany).

The configuration is characterized by a *rotational transform*, such that a single line of

magnetic force, followed around the system, intersects a cross-sectional plane in points which successively rotate about the magnetic axis [51]. In addition to pinches, tokamaks and stellarators, other alternative magnetic confinement concepts are being developed, such as spheromaks, rotating plasmas, tandem mirrors and magnetized target fusion. These methods are described in [52, 53]. In particular, an intersting promising alternative is represented by the field-reversed configuration (FRC) which will be discussed in the next section.

3.4   Field-reversed configuration

The field-reversed configuration (FRC) is a particular magnetic-field geometry, accidentally discovered in θ-pinch machines in the $'$60s [54], in which a toroidal electric current is induced inside a cylindrical plasma, creating a poloidal magnetic field, reversed in respect to the direction of an externally applied magnetic field. The label FRC derived from the original plasma-formation method, not the shape of the field, as commonly thought. The use of FRC potentially offers several advantages over "main line" fusion devices, although the physics for this concept lags behind that of the Tokamak and provides good confinement and higher β, with high power densities, a relatively compact design and the possibility for steady-state operation. The high β, coupled with the FRC's quasi-linear geometry, reduces the required peak magnetic field by about a factor of 3 compared to a tokamak's [1]. Both FRCs and spheromaks are together known as compact toroids, as they are self-stable and do not require magnet coils running through the center of the toroid. Unlike spheromaks ($\beta \approx 0.1$), FRCs are typically more elongated without toroidal magnetic field externally-applied.
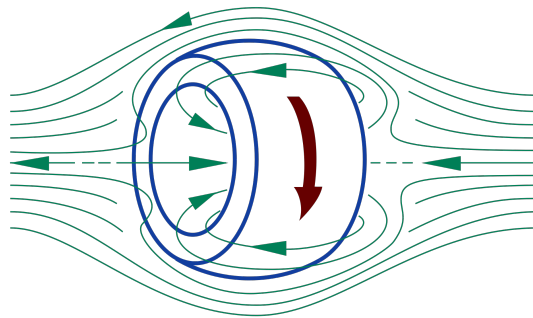
Figure 3.16: The field-reversed configuration (FRC) [55].

The resultant high-β axisymmetric compact toroid, illustrated conceptually in Fig. 3.16, is self-confined and uses diamagnetic ion currents to maintain the configuration. In order to well confine the hot plasma, it is important to have closed field lines, or more precisely, the magnetic field lines must be inside the chamber without crossing walls. Compact Toroids consist of two distinct regions: a closed field line region inside a magnetic *separatrix*, with radius r_s and an open field line sheath outside the separatrix. Then, hot plasma is confined inside the separatrix and exhausted through the open field line region and fusion conditions are achieved by compressing and heating the plasma. The reversed field is

maintained by a combination of fuel pellet injection and energetic fusion products which create an azimuthal plasma current.

FRC main characteristics are:

- no appreciable toroidal field.

- values of beta of order unity.

- no rotational transform.

- all the equilibrium current maintained by diamagnetism.

- a scrape-off layer (SOL) exhausting heat and particles outside the coil system.

FRCs have no toroidal field, dramatically reducing instability problems. Suffice to say that in order to evaluate the FRC plasma stability two dimensionless parameters are used: $s \approx 0.3 r_s / \rho_i$ and $S^* r_s \omega_{pi} / c$, where ω_{pi} is the ion plasma frequency and c the speed of light and more detail and explaination are discussed in [56].

3.5 Direct Fusion Drive

Direct Fusion Drive is a revolutionary fusion propulsion concept that would produce propulsion and electric power from a single, compact fusion reactor [57]. The project, funded by NASA (recent NIAC I and II grants and STTRs) is based on the overwhelming advantages offered by the Princeton Field Reversed Configuration (PFRC) concept, that will be discussed in the next section. The purpose of Princeton research is to find solutions to the critical scientific and technological problems related to fusion devices mentioned in the previous sections and lead to the development of compact low-radioactivity DFD propulsion systems, suited to several kind of space missions: heavy cargo, Mars manned missions and also to the outer solar system or the near interstellar space.

3.5.1 The Princeton Field-Reversed Configuration experiment

The DFD concept is related to the ongoing fusion research at Princeton Plasma Physics Laboratory (PPPL). The Princeton Field-Reversed Configurationan (PFRC), shown conceptually in Fig. 3.17, is ideally suited to be a steady-state MW-level rocket. PFRC is an experimental program, where the current second generation machine (PFRC-2) employs a unique radio frequency (RF) plasma heating method, known as "*odd-parity* heating".
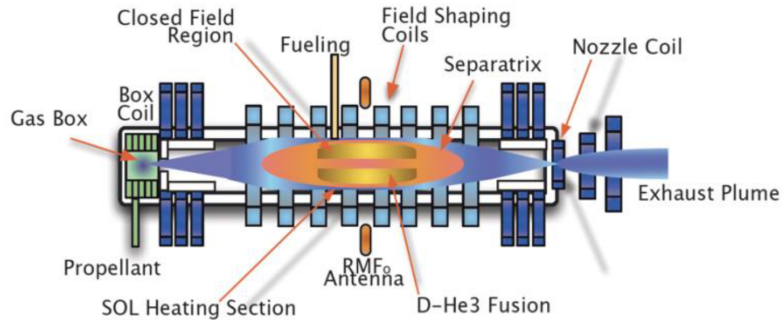
Figure 3.17: Schematic of a PFRC machine with its simple linear configuration and directed exhaust stream. Fusion occurs in the closed-field-line region. Propellant is added in the gas box where it is ionized; that plasma then flow along field lines in the open-field-line region (SOL) and across the *separatrix* surface of the CFR where its electrons are heated. The propellant ions are accelerated axially as they pass through the nozzle coil. Fuel is injected into the FRC core by neutral beams.
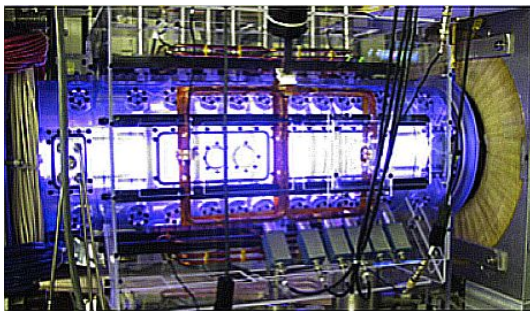
(a) PFRC-2 experiment.
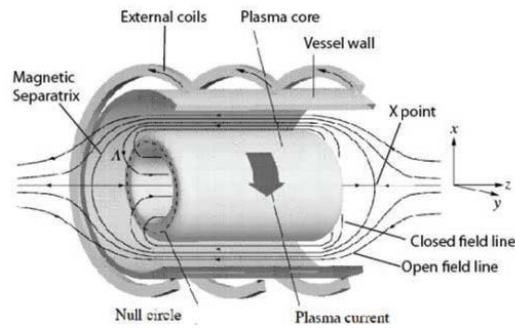
(b) FRC sketch

Figure 3.18: Figure(a): Real picture of the PFRC-2 experiment in the Princeton Plasma Pyshics Laboratory. Figure(b) is a simple scheme that shows the several different field surfaces in the core of the DFD.

The region where abundant fusion reactions take place is the high temperature (≈ 100 keV), moderate density ($5 \cdot 10^{14}$ cm^{-3}) plasma region named the core. For the FRC, this region is inside the magnetic *separatrix*, see Fig. 3.18, an imaginary closed surface that demarcates open magnetic-field lines, those that leave the device, from closed magnetic-field lines, ones that stay fully inside the device. The open field-line region is also called the scrape-off layer, SOL. To form the closed magnetic-field lines, a strong plasma current is needed, perpendicular to the FRC's magnetic field. On axis, the direction of the magnetic field created by the plasma current, is opposite to that of the "open" field lines which are created by external coils. If the axes of the two fields are not exactly parallel, MHD theory [58] predicts that the configuration will strongly tilt and destroy itself. S. A. Cohen and R. D. Milroy found that a magnetic field that is antisymmetric about the axial midplane can be added to a FRC and maintain its closed field line structure. It was first

theorized in 2000 [59] and subsequently demonstrated in the PFRC-1 experiment in 2006 [60]. Several attempts have been made in the past to heat FRC plasmas with RF, but always obtaining a near-FRC plasma with "open" field lines (even-parity heating due to the symmetry of the induced magnetic field). This is a crucial point, because the "open" field lines let the plasma to escape and consequently reduce confinement time τ_E, which is tightly bound to optimal fusion conditions, as discussed in Sec. 2.3.

3.6   Confinement and heating

More specifically, PFRC exploits a rotating magnetic field (RMF_o) with *odd-parity* symmetry, produced by the oscillation of the current in four quadrature-phased radio-frequency (RF) antennae, which can be seen in Fig. 3.18 wrapped in orange Kapton tape. Two pairs operate 90 degrees out of phase on adjacent sides of the plasma and generate RMF_o which is about $0.1 - 5\%$ the strength of the axial magnetic field. Then, the magnetic field on one side of each figure-8 is in the opposite direction as the other side and closed field lines in the generated FRC. The closed field lines keep the plasma trapped when it is heated. A toroidal current is induced, by RMF_o, in a cylindrical plasma confined by the externally-applied axial magnetic field. Then, this current induces a poloidal closed magnetic field, which confine high-β plasma.
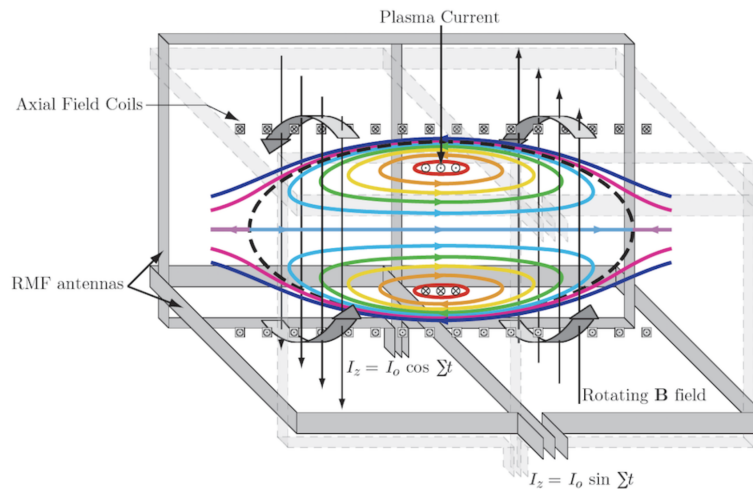
Figure 3.19: PFRC-2 rotating field scheme. External antenna produce rotating magnetic fields. The azimuthally rotating electric field results in a plasma current.

Therefore, RMF_o generates the current and heats the plasma ions and electrons, leading to compact devices and excellent stability due to the fact that a small, high-temperature FRC plasma, it is said to be *kinetic* rather than *fluid-like* and is stable against the tilt mode. The reason for the stability of a kinetic plasma against the tilt mode can be understood by considering the axis-encircling orbit of a single charged particle in a magnetic field, a stand-in for a hot plasma. An axial push to the particle, in an attempt to tilt its axis, causes the particle to translate along B, not to tip over. No tilt occurs. More complicated explanations can be extracted from Steinhauer's review [61]. Both current drive and FRC

plasma formation is obtained by *odd-parity* RMF_o [62]. The time variation of magnetic field generates an azimuthal electric field (E_ϕ) near the O-line magnetic null, shown in Fig. 3.20, which rotates with the RMF_o. The E_ϕ is created near the O-line magnetic null and charged particles are directly accelerated into punctuated betatron orbits, separated by periods in cyclotron motion.
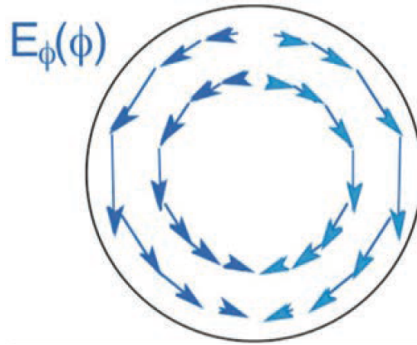
Figure 3.20: A representation of the azimuthal electric field in the midplane of FRC plasma, created by RMF_o. This field rotates with RMF_o.

Therefore, the charged particles accelerated along the null gain and lose energy due to the topology of the slowly rotating E_ϕ, which reverses direction halfway around. The more energetic they become, the further they can move away from null. In the RMF_o's rotating frame, Fig. 3.21, it has been observed that punctuated betatron orbit electrons move with an azimuthal velocity approximately equal to that of the RMF_o [63].
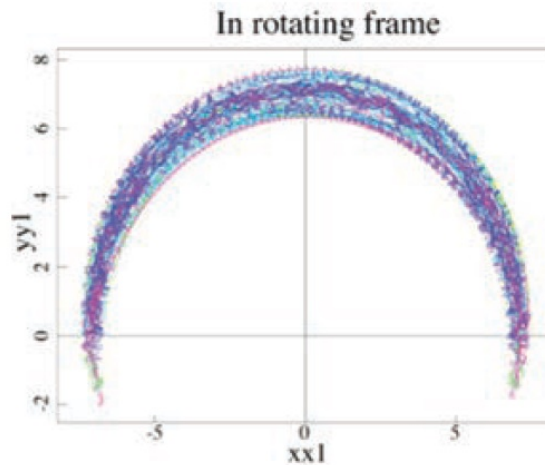
Figure 3.21: In the frame rotating with the RMF_o, the punctuated betatron trajectory appears as a crescent, with the betatron segments "inside" the cyclotron segments [1].

In an FRC reactor, these current-carrying electrons will have very high peak energy, about 5 times greater than in D-T tokamak fusion reactors [1], consequently their collisionality

will be more than 10x less. This contributes strongly to the high efficiency of RMF_o for driving current. Away from the O-line null, the more massive ions will carry an appreciable part of the current and diamagnetism will also provide a substantial part of the required current. Ion heating results from the same physical process, acceleration by E_ϕ, with an additional contribution from the RMFo-created z and r electric fields. Importantly, for both electron and ion heating, the non-uniformity of the FRC's magnetic field, especially the presence of nulls, causes orbits to lose track of the phase of the RMF_o, introducing stochasticity into the motion hence net energy gain [64]. In summary, the RMF_o method improves energy confinement, current drive, plasma heating, and plasma stability.

3.7   Fuel choice and neutron production

The production of neutrons by fusion is particularly problematic for spacecraft propulsion. Neutrons cause damage and activation of nearby materials and structures, limiting their lifetime, necessitating maintenance, and increasing the mass needed for shielding. Neutrons are hard to "direct" in such kind of magnetic device due to the fact that they have no charge and they do not interact with electric or magnetic fields. Therefore, it is very important to reduce the neutron fluxes and the most common method suggests to use the primary fuel mixture of D-^{3}He for the reason explained in Sec. 2.4. The D-^{3}He reaction already mentioned is

$$_1^2\text{D} + {}_2^3\text{He} \quad \longrightarrow \quad {}_2^4\text{He (3.6MeV)} + p \text{ (14.7MeV)}. \tag{3.25}$$
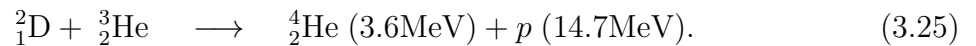
Althought, this is an aneutronic fusion reaction is not the only fusion reaction that can take place. It is essential to consider also the side reactions

$$_1^2\text{D} + {}_1^2\text{D} \quad \longrightarrow \quad {}_2^4\text{He} + \gamma + 23.85 \text{ MeV}, \tag{3.26}$$

$$_1^2\text{D} + {}_1^2\text{D} \quad \longrightarrow \quad {}_2^3\text{He (0.82MeV)} + n^0 \mid 50\%, \tag{3.27}$$

$$_1^2\text{D} + {}_1^2\text{D} \quad \longrightarrow \quad {}_1^3\text{T (1.01MeV)} + p \text{ (3.02MeV)} \mid 50\%, \tag{3.28}$$

$$_1^2\text{D} + {}_1^3\text{T} \quad \longrightarrow \quad {}_2^4\text{He (3.49MeV)} + n^0 \text{ (14.1MeV)}. \tag{3.29}$$
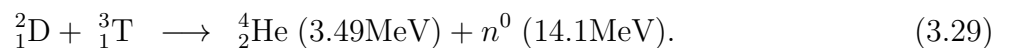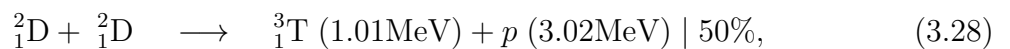
$$\tag{3.30}$$

Deuterium-deuterium side reactions will produce small numbers of moderate energy neutrons and some tritium. If the tritium fuses with deuterium, high energy neutrons are produced which are very damaging. The small size of the machine facilitates the rapid exhaust of tritium ash thus eliminating these harmful deuterium-tritium side reactions. The production of neutrons is reduced further by altering the fuel ratio to have three times the ^{3}He as deuterium, i.e. a ratio of 3:1, favoring the helium-3 reactions. An excelent neutron reduction results in a great mass save for the entire engine, the PFRC can be

shielded simply with boron carbide, a chemically stable solid. The ^{3}He fuel consumption, in general, is very complex to calculate and it depends on multiple factors related to the fuel reaction. In order to evaluate the order of magnitude of the consumption, we interpolated data from previous missions. Multiple preliminary studies have been proposed, and some of them are in a very early stage: this means that the fuel consumption is usually neglected because of its small mass, but for some of them the fuel consumption it has been simulated, based on the duration of the mission, the power and the efficiency of the fusion reaction. As can be seen in Table 3.1 the fuel consumption is around 0.000147 kg/(MW×day). This means that, for a 2.5 years mission, under the hypothesis of a 2-MW class engine always on, the mass of ^{3}He required would be about 0.27 kg. This fuel mass value, on a spacecraft of multiple tonnes, can be neglected in all trajectories calculations. Although, the amount of ^{3}He on the surface of Earth is limited as seen in Sec. 2.4.1, this value is well below the maximum availability.

Table 3.1: In this table, taken from Ref. [65], the fuel consumption has been calculated by dividing the total fuel consumption by the days of mission and the fusion power. In this way it has been found a fuel consumption per day per MW of power.

Mission	Fusion power, MW	Travel time, days	Total fuel, kg	Fuel consumption, kg
Mars	60	110	0.98	0.000148
Pluto	0.6	1826 [5 years]	0.16	0.000146
125 AU	0.8	3653 [10 years]	0.43	0.000147

In summary, the simple geometry of the machine, low radiation, and moderate magnetic field strength all contribute to lowering development and maintenance costs. There are no hazardous fuels or materials required. The DFD has been designed to be safe and affordable.

3.8 DFD Engine

The power and mass budget for a complete direct fusion drive system has been developed for previous works made by PPPL and PSS. Since the first studies of the DFD, it has been taken into account the mass of the various components of the engine. In this section it will be introduced the approach to the mass budget, without focusing on the details, which go beyond the purpose of this thesis. These works are important to better estimate the specific power of the technology. For our work puprose a conservative value for the specific power has been chosen. 0.75 kW/kg results in an engine mass of about 2660 kg, which is the estimated mass used for our calculation.
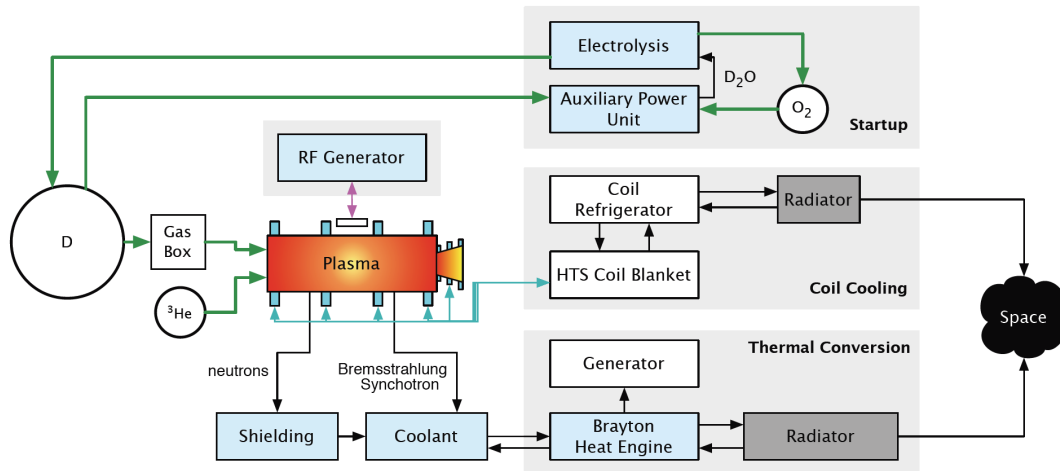
Figure 3.22: Direct fusion drive subsystems block diagram. Credit: Princeton Satellite Systems.

A Brayton cycle was chosen for electric power generation, where a fluid is compressed, heated, passed through turbines, and then cooled. Whereas jet engines employ open-loop Brayton cycles using air as the working fluid, all space applications must employ the closed-loop version to contain the working fluid (70/30 mole fraction mixture of helium and xenon). As discussed in Sec. 3.6, the DFD is RF heated and the efficiency of the RF subsystem is really crucial. Current space-qualified radiators will be too heavy but there are upcoming radiator materials that will make the radiators mass a small fraction of the engine total. NASA is currently supporting research in this area, such as the work on carbon-carbon radiators performed by the University of Massachusetts with the support of the MSFC Center Innovation Fund [66]. The goal is to reduce the areal mass of radiators from about 10 kg/m^2 currently to 2 kg/m^2 or less and an average temperature of 625 K. Other essential topics are the superconducting coils and the shielding design, that are discussed in [66] but available data suggests that research in all these areas has made tremendous progress and no roadblocks have been identified. Therefore, based on the estimations made in [66, 67, 1], engine data related to spacecraft mass and power are used as input for our work.

(a) Power flow for 1-MW engine. (b) Power flow for 2-MW engine.
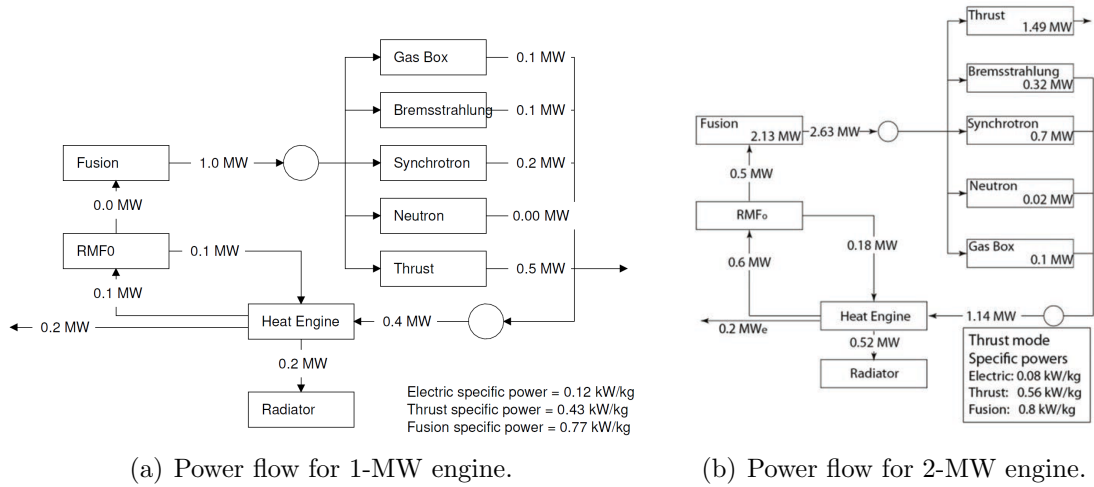
Figure 3.23: Figure(a): Power flow for the 1-MW class engine. Figure(b) is a simple scheme that shows the power flow for the 2-MW class engine. Credit: Princeton Satellite Systems.

The fusion power generated by the DFD core can be further decomposed in many parts, some of which are about dissipation, while others about power conversion. The product of the fusion is decomposed in the features from Fig. 3.23.

- Neutron. This is the power lost because of the neutron emission.

- *Bremsstrahlung* and *Synchrotron*. These are the power dissipated because of the breaking and *Synchrotron* radiations.

- Gas box. It is the power that goes to the ionization of the propellant.

- Thrust. This is the power converted to thrust in the SOL.

Among the losses, part of that power is recovered by a cooling system that ends with a heat engine, which generates electrical power from heat. Part of that heat has to be radiated towards the space by the radiators, while the electrical power will feed the spacecraft subsystems and also the rotating magnetic field unit, that is fundamental to achieve the fusion.

3.9 Thrust Augmentation

Researchers at PPPL performed simulations using UEDGE software [68], a 2D multi-species fluid code, in order to model the cylindrically symmetric FRC SOL region of the DFD. UEDGE finds a steady-state self-consistent solution to continuity equations, momentum equations, and energy equations for each species. This software also calculates ionization and recombination rates, and has scripts to calculate the flow of power and particles in a simulation. This included determining the SOL parameters (temperature, density, velocity, etc) and power flow within the SOL, each as a function of heating power

and gas input. It also included assessing the degree of detachment obtained for varying inputs. Starting from gas input and heating power the performance of an FRC as a DFD rocket engine have been evaluated, determining typical values of thrust, efficiency and specific impulse (exhaust velocity). Figure 3.24 shows the SOL simulation under the assumption that the FRC core is generating fusion power. The left of the image represents the gas box, the right of the image represents the magnetic nozzle and expansion region, and the center of the image represents the SOL field lines surrounding the core. This heated plasma will expand in a magnetic nozzle, converting the thermal energy of the plasma to kinetic energy, thus providing thrust to the system. This works exactly as a physical nozzle, with the difference that the fluid does not directly hit any physical wall. It is also possible to see where the fusion products are expected to deposit energy (red arrows) in a FRC reactor as well as where power is deposited in the electrons in this simulation.
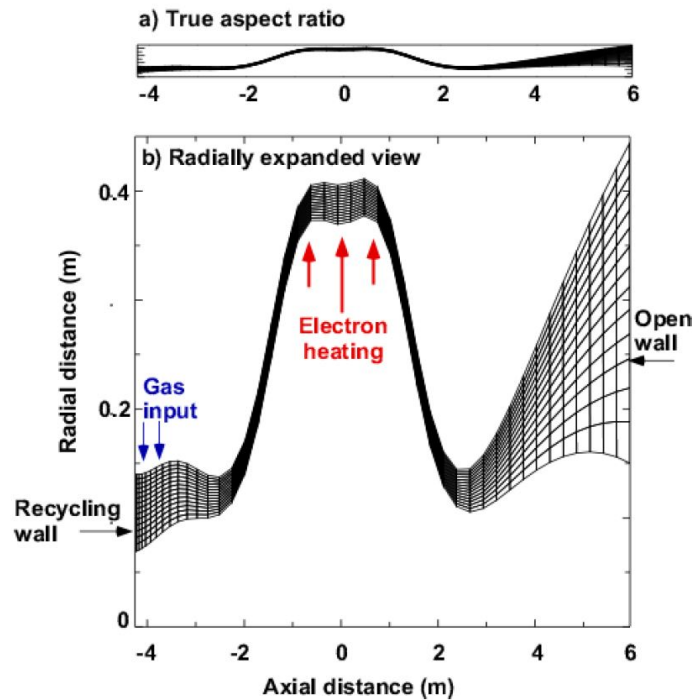
Figure 3.24: UEDGE magnetic geometry used for the simulations. (a) gives the true aspect ratio of the simulation, while (b) is a radially expanded view. Credit: Princeton Satellite Systems.

Deuterium plasma is used in this simulation, along with two types of deuterium gas: atomic deuterium (D) and molecular deuterium (D_2). Molecular deuterium is what is puffed into the simulation. UEDGE allows for a molecule to dissociate into two atomic deuterium. When this happens, 10 eV is transferred from the electron thermal energy into the ion/atomic neutral thermal energy. For instance, when an atomic deuterium is ionized, 13.6 eV is taken from the electron channel and when a deuterium ion recombines, 13.6 eV is radiated as a photon. For more details, see Ref. [68].
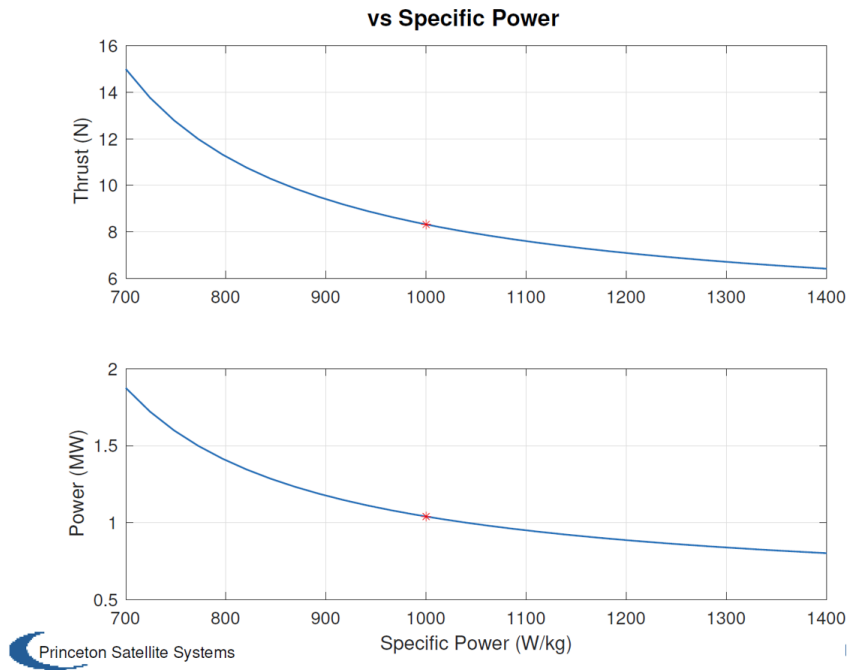
Figure 3.25: Variation of the thrust and power with engine specific power considered. Credit: Princeton Satellite Systems.
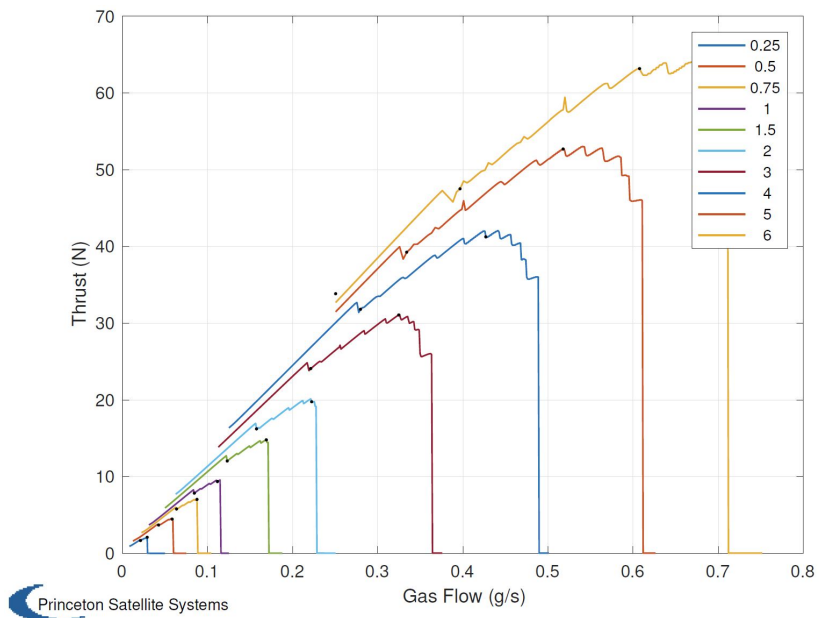
Figure 3.26: Thrust data from UEDGE simulations of SOL input power (MW) and gas flow rate. Credit: Princeton Satellite Systems.

Resarchers at Princeton Satellite Systems consider this data to produce a functional model of the thrust and specific impulse of the engine as a function of input power and gas flow

58

rate. Figure 3.26 shows the latest data. It is essential to underline that the power levels in the legend are for power P into the SOL, which is only a portion of the total fusion power. Mainly, for this kind of engine there are two inputs: the power inside the SOL and the propellant mass flow, not the fuel mass flow responsible for the fusion itself, which is negligible. The first is of the order of $40-50\%$ of the total power generated by the fusion, while the latter is of the order of $0.01-0.1$ g/s. The small dots mark the operating range of interest. For each power level, there is a fairly narrow range of flow rates which can absorb the power and provide the maximum thrust. These regions have been modeled as linear, with the slope and intercept as a function of input power. It is also important to notice that specific impulse and efficiency rapidly fall down for a particular gas input. This is because from simulations appears that increasing the propellant flow for the fixed input power leads to detachment of plasma from outer boundary walls and this causes a drop in all values. This has resulted in the model shown in Fig. 3.31.
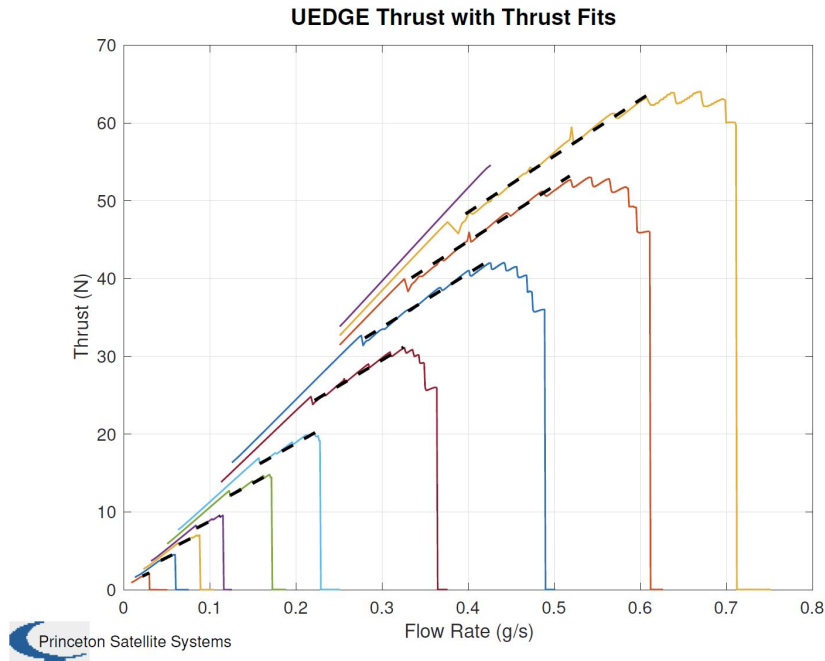
Figure 3.27: Thrust model verses UEDGE simulation data. Credit: Princeton Satellite Systems.

Once the continuity equations of energy and momentum are solved through the UEDGE code, the exit velocity together with mass flow are used to compute typical rocket parameters, the thrust and specific impulse:

$$T = \dot{m}v_{\parallel}, \tag{3.31}$$

where $v_{\parallel}$ is the velocity of particles parallel to the axis of the engine and

$$I_{sp} = \frac{T}{\dot{m}g_0}, \tag{3.32}$$

59

where $g_0 = 9.806$ m/s^2 is the acceleration of gravity on the surface of Earth. Moreover the propulsion efficiency is defined as the ratio of kinetic energy involved to thrust generation to the input power to the SOL P and can be written as

$$\eta = \frac{\dot{m}v_\parallel^2}{2P}. \tag{3.33}$$

In summary, thrust augmentation is the process by which additional ionized gas flows through the PFRC and produces thrust. The fusion products alone, if ejected directly from the engine, would have a velocity of 25,000 km/s and produce negligible thrust [66]. In the PFRC, these products interact with cool ionized gas in a region called the scrape-off-layer (SOL). Energy is transferred from the hot products to the SOL electrons, and this energy is in turn transferred to the ions as they traverse and exit the magnetic nozzle. The result is an exhaust with a bulk exist velocity of about 100 km/s and a thrust of about 2.5 to 5 N per MW of fusion power. As reported in the PSS studies [66, 1] a feasible performance space is 5 to 10 N of thrust per 1 MW of thrust power, with a specific impulse of about 10,000 s. Figure 3.28 shows the thrust model for a 1 MW power input. The specific impulse ranges from 8500 to 9600 seconds. Figure 3.29 shows a 4 MW power input. The specific impulse now ranges from 10,000 to 12,000 seconds.
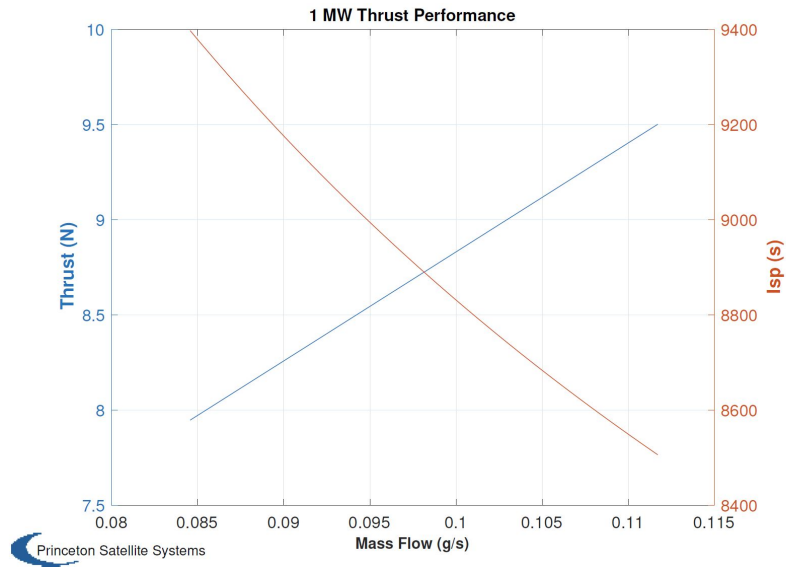
Figure 3.28: Thrust performance for a 1 MW power input. Credit: Princeton Satellite Systems

60
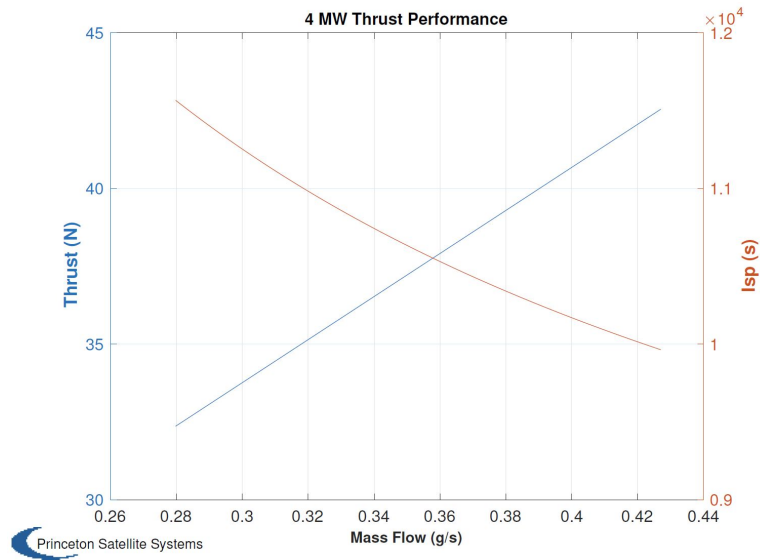
Figure 3.29: Thrust performance for a 4 MW power input. Credit: Princeton Satellite Systems

The trend of higher specific impulse for higher power level is clearly related to the greater energy available to the propellant. The efficiency increases both as the flow rate increases, at any given power level, and for higher power levels. Figure 3.30 shows the efficiency (conversion of output power to thrust), calculated by the PSS, from the model for 1 MW, 2 MW, and 4 MW power levels.
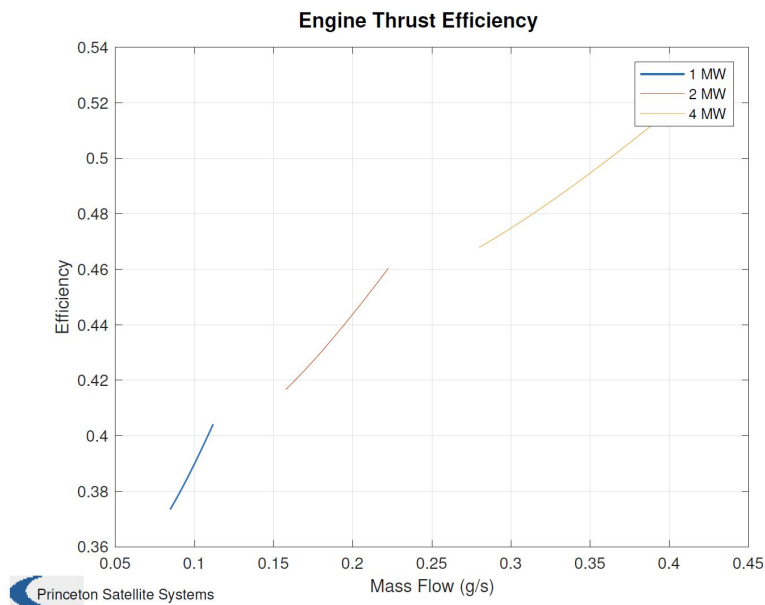
Figure 3.30: UEDGE thrust efficiency from input power. Credit: Princeton Satellite Systems
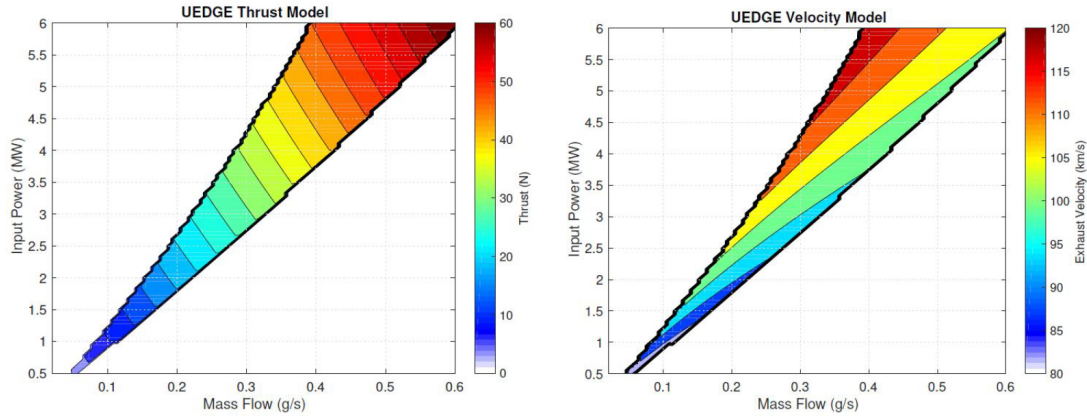
Figure 3.31: Dependence of thrust and exhaust velocity on propellant flow and SOL power. An increase of power input would require an increase of propellant mass input, but it would lead to higher thrust and I_{sp}. An increase of power input would also increase the range in which T and I_{sp} vary.

The overall results are reported in Table 3.2 for the low and high power configurations. It is important to emphasize that the specific power is higher for the low power configuration. However, the DFD can be fully scaled in configuration and reach the power required. Many estimations have been made about the exact specific powers for this engine, but at this point of the development only ranges can be estimated.

Table 3.2: Direct Fusion Drive characteristics for low and high power configuration [1].

	Low power configuration	High power configuration
Fusion Power, MW	1	10
Specific Impulse, s	8000 - 8500	9900 - 12000
Thrust, N	4 - 5	35 - 55
Fusion Efficiency	0.17 - 0.18	0.27 - 0.31
Thrust Power, MW	0.46	5.6
Specific Power, kW/kg	0.75	1.25

Due to the compactness of this engine, multiple modular DFDs can be combined into a cluster of many engines: it will result in a total thrust that is the sum of the thrusts from the single engines. The I_{sp}, though, will remain the same, because multiple engines will not affect the propellant consumption of each DFD.

4 Orbital mechanics and trajectory design

Trajectory design for low-thrust propulsion systems represents a complex problem and in this section only a qualitative description will be given. As well known, spacecraft motion is governed by a sensitive system of non-linear differential equations and, incorporating low-thrust forces into this system, adds complexity to the problem of modelling the trajectory.

Starting from the equations of motion it is possible to describe the Keplerian trajectory of a spacecraft taking into account the two-body problem:

$$\mathbf{a} = \frac{d^2\mathbf{r}}{dt^2} + \frac{\mu}{r^3} \cdot \mathbf{r} = \frac{\mathbf{F}}{m}, \tag{4.1}$$

where $\mathbf{r}$ is the radius vector of the orbit and μ is the gravitational parameter of the central body in the approximation of taking into account only the mass M related to the main body, defined as

$$\mu = GM, \tag{4.2}$$

where G is the gravitional constant ($6.67408 \cdot 10^{-11}$ m^{3}kg^{-1}s^{-2}). Eq.(4.1) relates instantaneous acceleration to the position at time t, to gravitational constant of the central body and to all perturbation forces which acts on the spacecraft. Considering the simple case of $\mathbf{F} = 0$ the acceleration $\mathbf{a}$ of the body only depends on the gravitational interaction with the main body. In order to deduce the spacecraft position r as a function of time, Newton's second law must be solved for whatever forces may act on the body. The exact solution of this equation, which results in a circular, ellitical, parabolic, or hyperbolic geometry, depends on the assumption that there were only two point particles interacting by the inverse square force ("gravitational two-body problem"). Only in this simplified case, in fact, the problem has an exact solution that reproduces Kepler's laws [69]. Though, it is essential to emphasize that if one or more additional interactions are taken into account, such as the small propulsive acceleration, no exact solution for the differential equations of motion of any of the bodies involved can be obtained. It is then convenient to treat this kind of motion as slightly perturbed elliptical motion and to determine the changes in the parameters of the orbital geometry that result from the small perturbating forces acting. As well known the orbital parameters, shown in Fig. 4.1 are univocally determined by the six initial conditions (three components of the position vector and three components of the velocity vector) relative to a coordinate system that is fixed with respect to the reference plane.
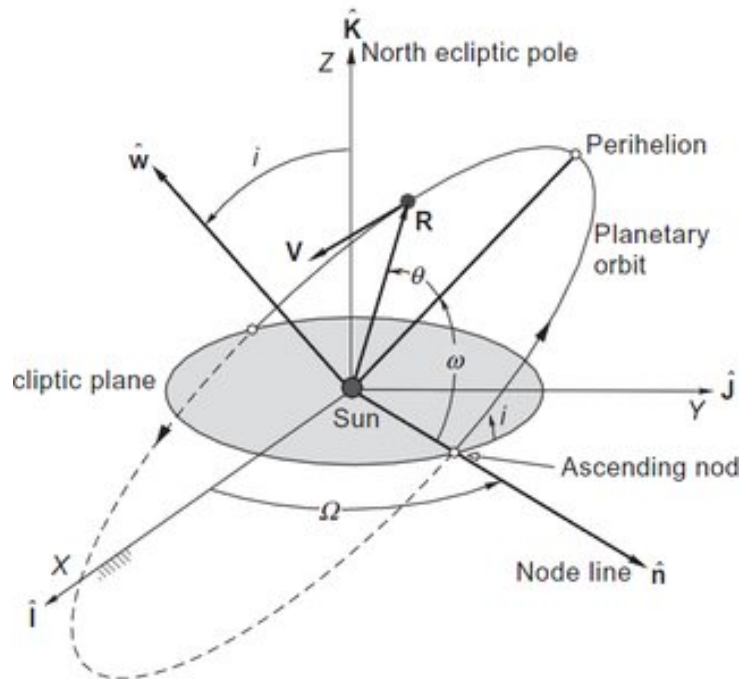
Figure 4.1: Main Keplerian orbital parameters represented using a heliocentric reference system (Sun mean ecliptic J200). The plane x,y is the ecliptic plane, which is the mean plane of the Earth's path around the Sun over the course of one year.

The Orbital elements are the parameters required to uniquely identify a specific orbit:

- the semi-major axis a, the sum of the periapsis and apoapsis distances divided by two;

- eccentricity e, determines the amount by which its orbit around another body deviates from a perfect circle. A value of 0 is a circular orbit, values between 0 and 1 form an elliptic orbit, 1 is a parabolic escape orbit, and greater than 1 is a hyperbola;

- inclination i is the tilt angle measured perpendicular to line of intersection between orbital plane and reference plane;

- argument of periapsis ω defines the orientation of the ellipse in the orbital plane, as an angle measured from the ascending node to the periapsis;

- true anomaly θ is the angle between the position vector $\mathbf{R}$ and the periapsis vector;

- longitude of the ascending node Ω is the angle from a reference direction, called the origin of longitude, to the direction of the ascending node, measured in a reference plane.

When small perturbations are taken into account, it is convenient to consider the orbit as an instantaneous ellipse whose parameters are defined by the instantaneous values of the

64

position and velocity vectors. Perturbations cause the six formerly constant parameters to vary slowly from the Keplerian solution, and the instantaneous perturbed orbit is called an osculating ellipse, which is the elliptical orbit that would result if all perturbing accelerations could be suddenly removed. The Lagrange planetary equations are first-order differential equations, which enable to calculate the rates of change of the orbital parameters, arise from the second-order differential equations that result by equating the mass times the acceleration of a body to the sum of all the forces acting on the body, as previously discussed.

As well known, considering a system in which only conservative forces act and do not depend on the velocities, there is no loss of the mechanical energy. Therefore, the forces involved can be derived from partial derivatives of a function which depends from spatial coordinates only, called the *potential energy*, whose magnitude depends on the relative distances of the masses. Whereas a simple two-body case the equation expressing conservation of the specific orbital energy is

$$\frac{V^2}{2} - \frac{\mu}{r} = -\frac{\mu}{2a} = constant. \tag{4.3}$$

The specific kinetic energy of a single body is one-half the square of its velocity, and the total kinetic energy is the sum of such expression for all the particles being considered. The conservation of energy equation relates the velocities of all the masses involved to their positions at any time. The partial derivatives of the potential energy with respect to spatial coordinates are transformed into partial derivatives of a disturbing function with respect to the orbital elements in the Lagrange equations, where the disturbing function vanishes if all the perturbing effects are removed. Like Newton's equations of motion, Lagrange's differential equations are exact, but they can be solved only numerically or analytically by successive approximations [70]. Lagrange planetary equations are:

$$\dot{a} = -\frac{2a^2}{GMm}\frac{\partial R}{\partial T}, \tag{4.4}$$

$$\dot{e} = -\frac{a(1-e^2)}{GMme}\frac{\partial R}{\partial T}, \tag{4.5}$$

$$\dot{i} = -\frac{1}{\sqrt{GMm^2a(1-e^2)}\sin i}\frac{\partial R}{\partial \Omega} - \frac{1}{me}\sqrt{\frac{1-e^2}{GMa}}\frac{\partial R}{\partial \omega}, \tag{4.6}$$

$$\dot{\omega} = \frac{1}{me}\sqrt{\frac{1-e^2}{GMa}}\frac{\partial R}{\partial e} - \frac{1}{\sqrt{GMm^2a(1-e^2)}\tan i}\frac{\partial R}{\partial i}, \tag{4.7}$$

$$\dot{\Omega} = \frac{1}{\sqrt{GMm^2(1-e^2)}\sin i}\frac{\partial R}{\partial i}, \tag{4.8}$$

$$\dot{T} = \frac{2a^2}{GMm}\frac{\partial R}{\partial a} + \frac{a(1-e^2)}{GMme}\frac{\partial R}{\partial e}. \tag{4.9}$$

This equations describe the rates of change for the orbital elements, where R represents the perturbation, T is the orbital period, M and m are the masses of the body involved. In general, incorporating low-thrust forces into the system results into a variation of the total energy. Low thrust problems can be treated using a perturbation approach like

Encke or variation of parameters, but high thrust should be treated using the Cowell technique since the thrust is no longer a small perturbation, but a major force [69]. As just mentioned, it is possible to make use of the perturbation theory to model the motion of the propelled spacecraft, considering the continuous and small propulsive acceleration as a perturbing effect. Therefore, as previously anticipated, the perturbation (thrust) makes the real orbit differ from the keplerian solution.

4.1 Gauss planetary equations

Starting from the Lagrange planetary equations, containing partial derivatives of the perturbing potential with respect to osculating elements, it is possible to obtain the Gauss planetary equations which contains the perturbing forces instead of the derivatives of the potential. It is generally assumed that these Gaussian equations are suitable even if the perturbating forces are not derivable from a potential (Drag would be an example), as in Ref. [71]. Let us consider a cylindrical reference system for the orbit. We can still use Eq. (4.1), and now we consider that

$$\frac{\mathbf{F}}{m} = \mathbf{a} = a_r e_r + a_\theta e_\theta + a_z e_z, \tag{4.10}$$

where e_r, e_θ and e_z are the unit vectors in the cylindrical reference system. The perturbing force (thrust) is decomposed into three main components i.e. along velocity (V, e_θ), normal (N, e_z), co-normal(C, e_r) directions, shown in Fig. 4.2.
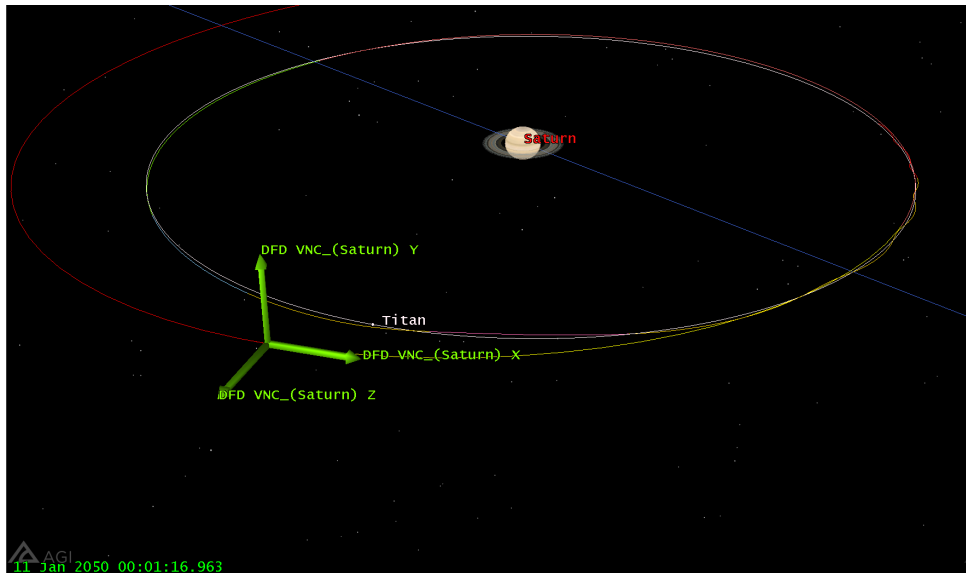
Figure 4.2: The VNC reference system (green), body ceneterd and the along velocity (V), normal (N), co-normal(C) directions are shown. The plane x - z is the orbital plane, and the y axes is parallel to the angular momentum h.

Gauss planetary equations:

$$\dot{a} = \frac{2ah}{\mu(1-e^2)} \left[e\sin\theta F_r + (1+e\cos\theta)\cdot F_\theta \right], \tag{4.11}$$

$$\dot{e} = \frac{h}{\mu} \left[\sin\theta\cdot F_r + (\cos\theta + \cos E)\cdot F_\theta \right], \tag{4.12}$$

$$i = \frac{\cos(\omega+\theta)r\cdot F_z}{h}, \tag{4.13}$$

$$\dot{\omega} = -\frac{h}{\mu}\frac{1}{e} \left[\cos\theta\cdot F_r - \left(\frac{2+e\cos\theta}{1+e\cos\theta}\right)\sin\theta\cdot F_\theta \right] - \frac{\cos i\sin(\omega+\theta)r}{h\sin i}\cdot F_z, \tag{4.14}$$

$$\dot{\Omega} = \frac{\sin(\omega+\theta)r}{h\sin i}\cdot F_z, \tag{4.15}$$

$$\dot{M}_0 = \frac{h}{\mu}\frac{(1-e^2)^{1/2}}{e} \left(\left[\cos\theta - \frac{2e}{(1-e^2)\frac{r}{a}}\right]\cdot F_r - \left[1 + \frac{1}{(1-e^2)}\frac{r}{a}\right]\sin\theta\cdot F_\theta \right), \tag{4.16}$$

where F_r is the co-normal component of the perturbation, F_θ is the along velocity component, and F_z is normal to the orbital plane, E is the eccentric anomaly, that is related to the true anomaly by

$$\tan E = \frac{\sqrt{1-e^2}\sin\theta}{e+\cos\theta}. \tag{4.17}$$

The eccentric anomaly can be also used to define the mean anomaly M by

$$M = E - e\sin E. \tag{4.18}$$

Also, we defined the mean motion as $n = \sqrt{\frac{\mu}{r^3}}$ and the mean motion at a certain epoch as

$$M_0 = M - \int_0^t n(t')dt'. \tag{4.19}$$

At any given instance in time, a perturbed orbit is completely determined by six osculating orbital elements. Finally, once all the initial conditions are defined, it is not possible to evaluate analytically the solution in the general case and the problem requires numerical methods as previously discussed, which are not analyzed in this work.

4.1.1 Thrust vector orientation

In most instances the targeting of a spacecraft during a maneuver is accomplished using the impulsive approach which does not involve any numerical integration. However, as advanced missions become more complex and depending on the considered performance of the engine, the impulsive analysis may not be adequate to calculate fuel requirements for a given maneuver. The impulsive maneuver approach can fail to produce the same results as a finite burn analysis for two reasons: one is the gravity gradient effect and the other is the effect due to non-constant thrust vector orientation during a maneuver. The gravity gradient effect is the contribution, to the motion of the spacecraft during a maneuver, of the time and position dependence of the gravitational acceleration. Consequently, algorithms which simulate the motion of a spacecraft during a maneuver are needed. This

need can be satisfied numerically integrating the nonlinear equations of motion through the burn, but the problem of how to treat the thrust vector arises and there are three options:

- keep the thrust vector orientation fixed throughout the burn interval;

- allow the thrust vector to pitch at a fixed rate;

- allow the thrust vector to have three degrees of freedom.

The problem of reaching prescribed boundary conditions is a matter of determining the correct thrust vector orientation and the best time or place to begin the maneuver. For our thesis work purpose, a finite maneuver analysis has been performed using Astrogator tool on STK software, which will be discussed in Sec. 4.2. Most of the time the thrust vector has been considered updated throughout the maneuver to maintain the required thrust direction. This choice forces the thrust vector to the specified direction at every instant during the burn. The thrust vector therefore rotates with the specified coordinate system or tracks with the spacecraft's inertial velocity vector, if the Along Velocity or Anti-Velocity Vector option is selected. In this calculation the finite maneuver is effectively an orbital propagation segment accounting for the acceleration due to thrust, which depends on the engine model. Like Propagate segments, each point calculated by the propagator is added to the ephemeris, and propagation continues until a stopping condition is met. Once a condition is met, Astrogator then finds the exact point, within tolerance, where the stopping condition is satisfied. The thrust vector will be determined by using the best estimate of the trajectory and a guess at the thrust vector orientation as the initial conditions in the nonlinear differential equations describing the motion of a thrusting spacecraft. This initial guess is an approximation, of the vehicle's orbital states, thrust attitude, and maneuver duration for the maneuver objective in question. The initial guess is iteratively refined by a numerical optimization library in its attempt to optimize the maneuver.

4.2 The software: Satellite Tool Kit (STK) analysis

Satellite tool kit is a physics-based software package from Analytical Graphics, Inc. that allows engineers and scientists to perform complex analyses of ground, sea, air, and space platforms, and share results in one integrated environment. It is possible to perform the entire desired space mission simulation, also analyizing the required maneuvers during the simulation thanks to the Astrogator tool.

4.2.1 Astrogator

STK Astrogator is a specialized analysis module for interactive orbit maneuver and spacecraft trajectory design, which calculates the satellite's ephemeris by executing a Mission Control Sequence, or MCS, defined according to the requirements of the mission. Astrogator provides the ability to model both impulsive and finite maneuvers as well as high-fidelity orbit propagation. It provides targeting methods, including a differential

corrector - which allows you to find the necessary values of control parameters (such as launch epoch or burn duration) to meet desired mission goals. Astrogator also utilizes a component catalog and editor in STK called the Component browser, that allows to define and customize engine models, force models, propagators, central bodies, and other elements of a space mission analysis scenario. In addition, the Component Browser contains a wide array of calculation objects.

- Propagator segment: By using the propagator segment, the software numerically integrates the equation of motion of the satellite from Eq. (4.1) until a user defined condition, that could be a duration, a distance from a reference system origin or plane, a vector magnitude (for example the velocity vector of a satellite) or many others. The solution of differential equations for the calculation of the trajectory can achieved via different methods, but the most used is a Runge-Kutta-Fehlberg method of order 7, and this means that at each step there are 7 terms in the numerical expansion. For further detail on those numerical methods see Refs. [72]. In addition to the choice of the propagator, the propagation segment needs to have one basic input, which is the stopping condition. Given the state of the spacecraft at which the propagator starts in terms of position vector and velocity vector, the propagator will calculate and plot the solution until the stopping condition, which is a numerical value with a tolerance.

- Maneuver: this segment enables the user to define a maneuver with a specific engine, that perturbs the motion of the spacecraft. Mainly, two kind of maneuvers can be used: impulsive and finite burn. The first case is not relevant to this study, since the subject is a low thrust engine. The finite meneuver enables the use of the same propagators used in the propagation segment, so multiple stopping condition can be used even in this case. The other fundamental input is the thrust vector. It is in fact user defined, and can be used as aligned with the velocity direction, opposite to it or it can have Cartesian coordinates to orient it in space. In most complex and advanced scenarios, it can be defined as variable in time. In most maneuvers, the most challenging part is to use the right thrust vector combined with a proper stopping condition. Moreover, the software itself does not converge very well if the thrust vector is defined in a translating and rotating reference system: for this reason, it has been mainly used inertially fixed in time. When necessary, multiple maneuvers in a pattern with different thrust vector direction were used.

- Target sequence: this fundamental structural element can be used to define maneuvers and propagations in terms of the goals they are intended to achieve at a defined instant at the end of a specified segment. A target sequence run the segments nested within it, and apply profiles to the run according to its configuration. When applying a search profile, the Target Sequence adjust the targeted values over user-defined multiple iterations in an attempt to converge at a solution within the defined tolerance. When applying segment configuration profiles, the Target Sequence alter the properties of the targeted segments to affect the course of the MCS run. The results of a Target Sequence can then be applied to the MCS to produce a trajectory that meets the goals you need to achieve using The differential corrector, which is an

algorithm that changes by a user defined step a set of user specified independent variables to obtain the requested value of the dependent variable chosen as a result. This algorithm works in an optimal way when very few (1-2) independent variables are used.

Impulsive thrust maneuvers are traditionally modeled as instantaneous, however the fundamental nature of low-thrust propulsion systems necessitates an alternative formulation. The fact is that a single low-thrust maneuver requires continuous thrust, and therefore, a continuous control history to define the pointing, and possibly the thrust level, at each instant during the maneuver. This difference in comparison to an instantaneous, impulsive thrust model results in many more design variables and a less intuitive problem overall. It is also true that an impulsive trajectory can be represented with a finite, small number of variables, the same can not be said about continuous-thrust trajectories which are in principal of infinite dimensions. While an analytical treatment of system dynamics is essential, many of the problems of interest are highly non-linear and do not admit analytical solutions, numerical study is the best approach. The challenges involved make the use of analytical solution ineffective and lead directly to the frequent introduction of numerical optimization techniques into the design process. Optimization methods yield state and control variables along a path that minimize a scalar cost function. These types of strategies are especially useful in the low-thrust trajectory design process because they offer guidance in the selection of values for numerous control variables. As previously said the problem is challenging and most nonlinear optimization methods require an initial guess that is "close" to an optimal solution, or at least "close" to a feasible solution.

However, developing a good initial guess can be as difficult as the optimization problem itself. For our work a real optimization process has not been performed but we tried to minimize fuel consumption for the entire mission in order to maximize the payload. Some of the most widely-used nonlinear programming (NLP) solvers in trajectory optimization include: SNOPT, MATLAB fmincon, KNITRO, NASA Goddard's GMAT (General Mission Analysis Tool) and its CSALT collocation tool; NASA Johnson's Copernicus Trajectory Design and Optimization System; and NASA JPL's MALTO (Mission Analysis Low Thrust Optimizer). High-performance NLP solvers are generally proprietary and each is set up as an "engineering black box".

On STK we used the sparse nonlinear optimizer (SNOPT), a software package for solving large-scale optimization problems, which employs a sparse sequential quadratic programming (SQP) algorithm with limited-memory quasi-Newton approximations to the Hessian of Lagrangian [73]. The SNOPT Optimizer search profile uses the SNOPT programming solver to achieve a certain goal - represented by a cost function and a set of constraint functions. The profile iteratively modifies a set of decision variables or controls to find a feasible, optimum solution. The SNOPT profile is mainly comprised of four tabs.

- Variables:

This tab allows the configuration of two types of quantities, the controls - optimizer decision variables - and the results - comprised of the objective function and the constraints. A profile must have at least one decision variable and one objective defined to execute properly. Objectives and constraints are derived from the same source and defined in the

same manner, but are different in terms of how they are applied to the problem; an objective is a quantity that the optimizer attempts to minimize or maximize, while constraints define the set of acceptable (feasible).

- Options

A few relatively common SNOPT options can be set through the interface under the options tab. These are the major and minor iteration limits and tolerances. If you require an extremely accurate solution, and are willing to wait for a longer amount of time, then the iteration values can be increased, and the tolerance values should be decreased. If you do not want to wait for a longer amount of time, and are willing to sacrifice accuracy for speed, then the tolerance values should be increased. The value for both iterations and tolerances is dependent on the problem that you are trying to solve, and if one set of values is not providing good enough answers, or is not converging, then they can always be changed to better suit the problem at hand.

- Log

The Log tab displays the detailed SNOPT iteration log, including the algorithm options. The log is made up of print and summary files, which are generated internally by SNOPT when it is run.

- Graphs

The graphs tab allows to define a variety of graphs of the optimizer profile's performance that can be generated manually when desired or automatically. The tab is divided into two general areas - a table that displays the graphs that have been assigned to the profile and the collection of properties that define the graph that is currently selected in the table. It is possible to find a more accurate explanation for all the math behind the problem in [74].

4.3   Scientific objectives of the mission

The mission is designed to explore the Saturn system, including its rings and moons, with a special focus on Titan. Saturn is predominantly composed of hydrogen and helium (97% molecular hydrogen and 3% helium by volume) and an admixture of heavier elements such as carbon and oxygen typical of "ices". These objects do no possess definite surfaces although they may have dense rocky or metallic cores. The average distance of Saturn from the Sun is about $1.427 \cdot 10^9$ km, approximately 9.4 times Earth's distance from the Sun. The light takes 8.3 minutes from the Sun to the Earth and 80 minutes to Saturn, even if Saturn is at the minimum distance from Earth, a signal takes more than an hour to reach us. Although, Jupiter (with an equatorial diameter of 142880 km) is almost 20% larger than that of Saturn (equatorial diameter of 120536 km), the ring system of Saturn has the incredible diameter of 274000 km, which is 70% the distance between the Earth and our Moon. The rings of Saturn are composed by a myriad of small particles, ranging in size from micrometers to meters, made almost entirely of water ice, with a trace

component of rocky material. It is possible to well observe from Earth both the northern and southern face of the rings due to the inclination of the rotational axis relative to the ecliptic plane (26° 44').

As previously mentioned, the mission studied has a particular focus on Titan, one of the most interesting moon in the Solar system. Titan was discovered on March 25, 1655, by the Dutch astronomer Christiaan Huygens, who was inspired by Galileo's discovery of Jupiter's four largest moons in 1610 and his improvements in telescope technology. It is the largest satellite of Saturn, only Ganimede (5268 km), which is one of Jupiter's satellites, has a larger diameter than Titan (5150 km). It is also interesting to underline that Mercury has a diameter of about 4878 km, then is smaller than both satellites.

Table 4.1: Titan mean orbital parameters considering for convenience the ecliptic plane as reference for the inclination.

Semi-major axis	$1.222 \cdot 10^6$ km
Radius of periapsis	$1.187 \cdot 10^6$ km
Radius of apoapsis	$1.257 \cdot 10^6$ km
eccentricity	0.02876
Inclination	0.3485°
Average orbital speed	5.5 km/s
Titan gravitational parameter	8978.52 km^3/s^2
Titan Radius	2574.73 km

Titan is the unique moon known to have a dense atmosphere, and the only body known in space, other than Earth, where clear evidence of stable bodies of surface liquid has been found [75]. The climate, including wind and rain, creates surface features similar to those of Earth, such as rivers, lakes, seas (probably of liquid methane and ethane), and deltas, and is dominated by seasonal weather patterns as on Earth. With its surface and subsurface liquids and a massive nitrogen atmosphere, Titan's methane cycle is analogous to Earth's water cycle, at the much lower temperature of about 94 K (−179.2°C). Because of the extremely cold temperatures typical of celestial bodies that are far away from the sun, the structure of Titan's chemical atmosphere is in a state of deep freeze. It is this chemical composition that interests scientists a great deal because Titan's atmosphere might consist of compounds similar to those present in the primordial days of the Earth's atmosphere. As reported by G. Tobie in [76]: "Before the Cassini-Huygens spacecraft arrived at Saturn, widespread liquid methane or mixed hydrocarbon seas hundreds of metres in thickness were proposed as reservoirs from which methane could be resupplied to the atmosphere over geologic time". Data from the international Cassini spacecraft that explored Saturn and its moons between 2004 and 2017 has revealed what appear to be giant dust storms in equatorial regions of Titan. The discovery, described in a paper published in Nature Geoscience [77], makes Titan the third body in the Solar system where dust storms have been observed (the other two are Earth and Mars). Titan fly-by observations [78, 79], rule out the presence of extensive bodies of liquid hydrocarbons at present, which means that methane must be derived from another source over Titan's history. Tobie, Lunine and Sotin, on the basis of their model, predict that future fly-bys

should reveal the existence of both a subsurface water ocean and a rocky core, and should detect more cryovolcanic edifices [76].

The scientific justifications for this kind of mission include a study of the Saturn system and can be grouped, as reported by European Space Agency (ESA) in [80], in 3 categories: Saturn, the magnetosphere, and Titan.

Saturn:

- "Observe seasonal variations in temperature, clouds, and composition, and in the winds at all accessible altitudes. By studying the temperatures, as well as the composition of features in the Saturnian system, scientists can study the miriad properties of Saturn's moons and can learn about how seasons affect Saturn's atmosphere and rings and also look at how light from the Sun and stars passed through atmospheres and rings in the Saturn system. Light is altered when it passes through gas or dust, and those changes tell scientists about the density and composition of the material through which the light passed."

- "Investigate the relationship between the ionosphere, the magnetic field, and the plasma environment. Scientists are interested to learn about the composition, density, flow, velocity and temperature of ions and electrons in Saturn's huge magnetosphere. By measuring the composition of the ions, is possible to determine the sources of plasma in the magnetosphere. During the Cassini-Huygens mission one of the major discoveries was that most of the ions in the Saturn system come from water ejected by Saturn's moon Enceladus. Before Cassini, some scientists thought most of the ions would be nitrogen-derived ions from Titan, but that turned out not to be the case. These kind of study was of vital importance at Titan, where instruments sensed large charged particles (which turned out to be negatively-charged ions) that play an important role in the formation of aerosols in the moon's atmosphere."

- "Investigate the relationships between the rings and the embedded moons and search for new ring-embedded satellites."

- "Study the interaction between the rings and Saturn's magnetosphere, ionosphere, and atmosphere. Moreover, miniscule particles of dust wander, orbit and race throughout the Saturn system. Some dust comes from outside the Saturn system, even from beyond our solar system. Other dust-sized particles arise from the surfaces of Saturn's rings and moons, and from the erupting plume of material at the moon Enceladus. By studying those particles scientists can better understand what produces them and how they interact with Saturn's rings, moons and magnetosphere."

As reported by NASA in [81] for the magnetosphere:

- "Use imaging and composition studies to determine the magnetosphere-satellite interactions at Saturn, and understand the formation of clouds of neutral hydrogen, nitrogen, and water products (such as protons, oxygen atoms or hydroxyl radicals)."
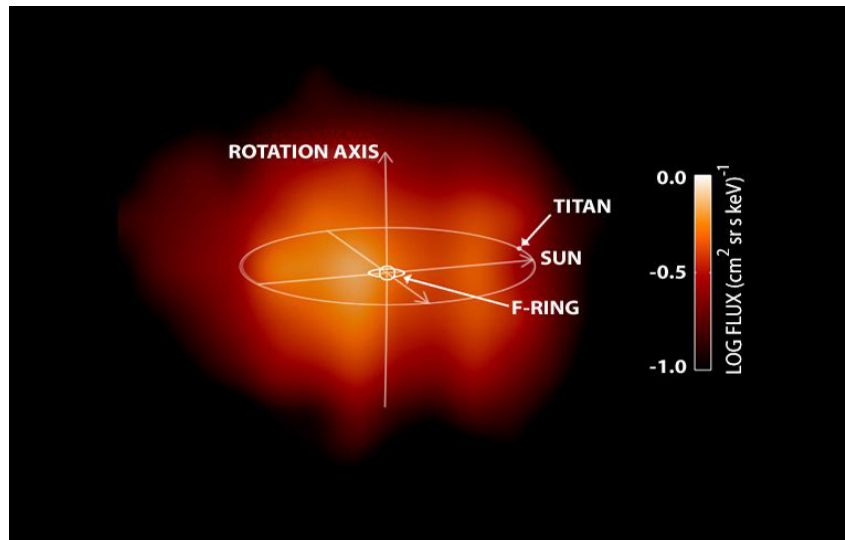
Figure 4.3: First image of a planetary magnetosphere, created by MIMI which is the first instrument ever designed to produce such kind of image. This sensational picture was produced in 2004, before orbit insertion, when Cassini spacecraft was about 6 million kilometers from Saturn [82]. Credit: NASA / Jet Propulsion Laboratory.

"This kind of study helps to determine the charged particle populations of Saturn's magnetosphere, as well as how the magnetosphere interacts with the solar wind. As well known, the sun constantly blasts the solar system with a torrent of charged particles called the solar wind, that can strip atmospheres from worlds, but like Earth, Saturn has a natural shield called magnetosphere. Magnetic fields easily influence particles that carry an electric charge, in other words, electrons and atoms that have lost or gained electrons. The solar wind has its own magnetic influence, and it pushes against Saturn's magnetic field, but Saturn's field is strong enough that it dominates a large region around the planet. That region, the magnetosphere, is the volume of space shielded from the solar wind by Saturn's magnetic field where the fast-moving charged particles floating around Saturn cannot easily escape. They are confined and must move according to the planetary magnetic field's force."

- "Determine the global configuration and dynamics of hot plasma in the magnetosphere of Saturn through energetic neutral particle imaging of ring current, radiation belts, and neutral clouds. As Cassini orbited Saturn, the magnetometer recorded the varying strength and direction of the planet's magnetic field in different locations."
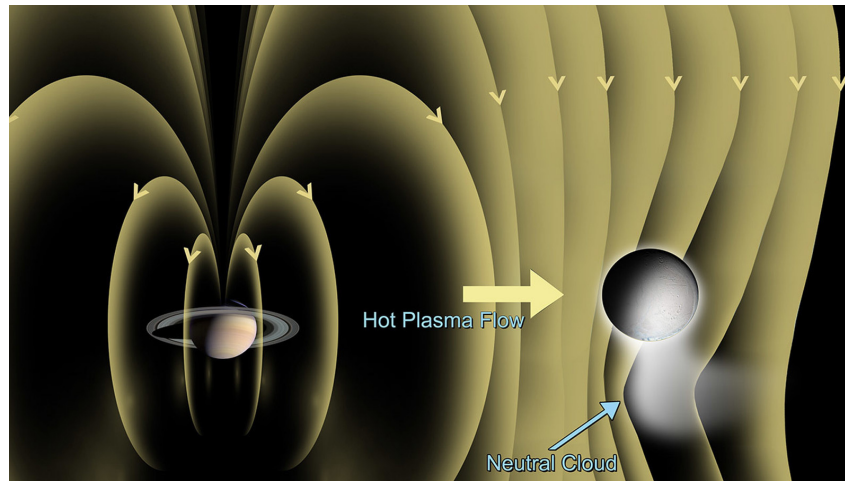
Figure 4.4: This artist concept shows the detection of a dynamic atmosphere on Saturn's icy moon Enceladus. The Cassini magnetometer instrument was designed to measure the magnitude and direction of the magnetic fields of Saturn and its moons. Credit: NASA / Jet Propulsion Laboratory.

"The knowledge of Saturn's magnetic field is poor if compared with Earth's field because to study a magnetic field, scientific instruments must be within that magnetic field. This helps scientists learn about the interiors of Saturn and its moons, along with the planet's magnetosphere, the giant region of space around the planet influenced by its magnetic field. Scientists used this data to produce 3-D models of the magnetosphere and to shed light on how the planet's magnetic influence affects the rings, moons, dust and gas within." "Anothre interesting point is that Saturn's core is a giant ball of unknowns, largely because it's impossible for even the strongest robotic spacecraft to reach. Hidden below thousands of miles of gases and crushing liquids, Saturn's deep interior is likely made of hydrogen and helium that's been forced, by the crushing mass of the planet, into a metallic liquid form. And like Earth's iron-core dynamo, because currents are swirling within this metallic fluid, it produces a magnetic field."

- "Study Saturn's magnetotail to determine its dynamics, conduct in situ studies of Saturn's ionosphere, and investigate magnetospheric periodicities. Cassini's instrument confirmed that Saturn's magnetic field is different from that of any other planet in the solar system and its magnetic poles actually match its axis of rotation. On Earth and Jupiter, for example, magnetic north wanders away from the planet's rotation axis by about 10 degrees, meaning that if you could see Jupiter's or Earth's magnetic field from space, it would appear to wobble like a hula hoop as the planet spins. Saturn's magnetic north pole, however, is essentially in line with the planet's axis of rotation, and it would appear to spin smoothly with no wobble. Given this orderly situation, MAG might be expected to observe a steady signal of strength and direction. This is not what was actually found at Saturn, where the instruments detected a signal in Saturn's magnetic field that repeats every 10 hours

and 47 minutes. The periodic signal, called a "periodicity", suggested that Saturn's magnetic field isn't really and truly aligned with the planet's axis of rotation, even though it would otherwise appear to be so."

- "Study magnetosphere-ionosphere coupling through remote sensing studies of the aurora and in situ measurements of precipitating energetic ions and electrons. Before Cassini, scientists knew that Saturn had radiation belts like Earth's Van Allen belts."
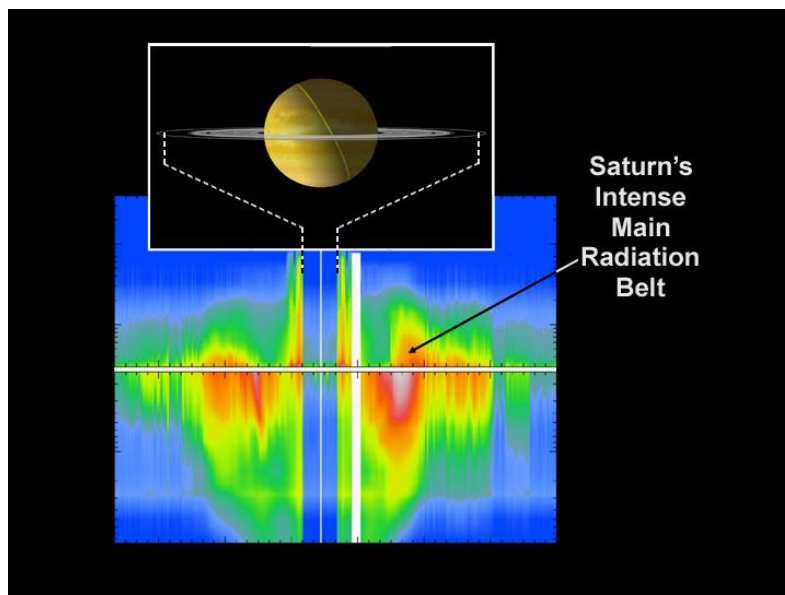
Figure 4.5: Saturn's main radiation belt as seen by Cassini on its first approach to Saturn in summer 2004. Credit: NASA / Jet Propulsion Laboratory.

"These are two doughnut-shaped regions (a larger one wrapped around a smaller one) encircling Earth where our planet's magnetic field traps charged particles. But at Saturn, scientists actually watched a radiation belt disappear. A transient radiation belt outward of the main belts was observed during the Cassini mission and scientists have noticed the amount of carbon ions increase in Saturn's magnetosphere, and discovered that "explosions" of plasma on Saturn's night side can produce sufficient pressure to cause the planet's magnetic field to inflate."

- "By studying radio and plasma waves around Saturn, scientists can better understand Saturn's relationship with its moons and rings, as well as how the planet interacts with the solar wind and investigate the sources of lightning. For example, Saturn's auroras emit radio waves in approximately the same frequency range as AM radio stations on Earth. Cassini was able to detect radio signals from lightning on Saturn. Lightning strokes emit electromagnetic energy across a broad range of wavelengths, including the visual wavelengths we see and long radio wavelengths that cause static on an AM radio during a thunderstorm. Some of the radio waves

propagate upwards and can be detected at long distances by the radio and plasma wave science instrument on Cassini."

Titan:

- "Determine the physical state, topography and composition of the surface and infer Titan's internal structure. In Cassini-Huygens mission radar instrument was built primarily for studying Saturn's moon Titan, which has a thick atmosphere that hides its surface."
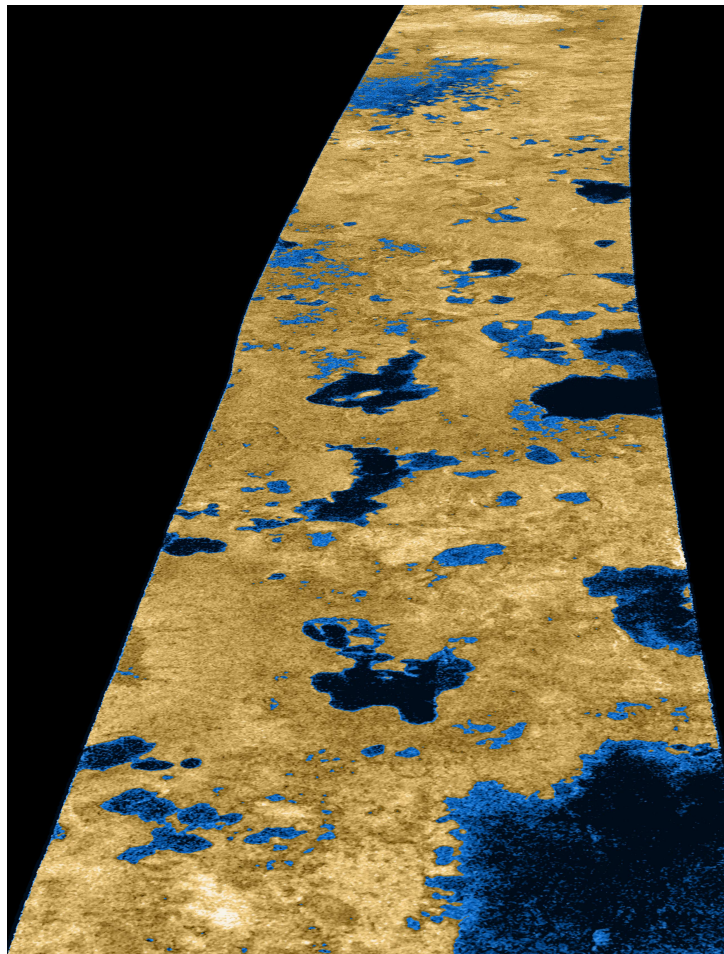
Figure 4.6: The existence of oceans or lakes of liquid methane on Saturn's moon Titan was predicted more than 20 years ago. But with a dense haze preventing a closer look it has not been possible to confirm their presence. Until the Cassini flyby of July 22, 2006, that is. Credit: NASA / Jet Propulsion Laboratory.

"The instrument bounced radio waves off of Titan and captured the reflected waves to see what's below Titan's haze, such as lakes, mountains, dunes. The instrument detected how smooth or rough surfaces are, making it useful for studying Titan's methane seas. Scientists also used it to study Saturn, its rings, and Saturn's other moons."

- "Follow-up on Huygens' in situ investigations by studying seasonal changes in Titan's methane/ hydrocarbon hydrological cycle, and in the high-latitude atmosphere."

- "Based on new knowledge, determine the types, composition, distribution, and ages of surface units, determine the internal and crustal structure, and measure aerosol and heavy molecule layers and properties."

- "Determine the abundance of the atmospheric constituents, including noble gases, establish isotope ratios for abundant elements, and constrain scenarios of formation and evolution of Titan and its atmosphere. During the Cassini-Huygens mission the ion and neutral mass spectrometer (INMS) was capable of determining the chemical, elemental and isotopic composition of the gaseous and volatile components of the neutral particles and the low energy ions in Titan's atmosphere and ionosphere, Saturn's magnetosphere, and the ring environment."

- "Measure the winds and global temperatures, investigate cloud physics, general circulation and seasonal effects in Titan's atmosphere, search for lightning discharges."

- "Investigate the upper atmosphere, its ionisation, and its role as a source of neutral and ionised material for Saturn's magnetosphere."

- "Study seasonal and temporal change with an emphasis on surface lakes and other materials, internal structure, aerosols and heavy molecules, upper atmospheric density, surface topography, surface temperature, clouds and winds. Considering also the seasonal changes in upper atmospheric properties, specifically the temperature and formation and break-up of the winter polar vortex."

- "Determine the internal structure of Titan - identify and understand origins of surface features and associated material (such as volcano-like formations with material apparently deposited around them that could support cryo-volcanism, or lakes and their surroundings)."

4.4   Previous Titan Saturn system missions

One can say that the exploration of Saturn system has been "poorly" performed and only three missions were flybys and the last space research mission (Cassini–Huygens) successfully sends the Cassini probe to study Saturn, including its rings and natural satellites. Orbiting Saturn and its several moons, the Cassini spacecraft had been a keystone of exploration of the Saturnian system and the properties of gaseous planets in our solar system. This remarkable mission involved a collaboration between NASA, the European Space Agency, and the Italian Space Agency (ASI). Launched aboard a Titan IVB/Centaur on 15 October 1997, Cassini was the fourth space probe to visit Saturn and the first to enter its orbit on 1 July 2004 [83].

Table 4.2: Previous space missions to the Saturn system

Pioneer 11	1974 flyby Jupiter and moons	1979 flyby Saturn and moons
Voyager 1	1979 flyby Jupiter and moons	1980 flyby Saturn and moons
Voyager 2	1979 flyby Jupiter and moons	1981 flyby Saturn and moons
Cassini–Huygens	2000 gravity assist Jupiter	2004–2017 orbiter Saturn 2005 lander Titan
Dragonfly	-	2034 planned rotorcraft lander mission on Titan

The Cassini orbiter had 12 instruments and the ESA's Huygens probe had six. Equipped to thoroughly investigate all the important elements that the Saturn system may uncover, many of the instruments had multiple functions. The spacecraft communicated through one high-gain and two-low gain antennas. It was only in the event of a power failure or other such emergency situation, however, that the spacecraft communicated through one of its low-gain antennas. Three radioisotope thermoelectric generators – commonly referred to as RTGs – provided power for the spacecraft, including the instruments, computers, and radio transmitters on board, attitude thrusters, and reaction wheels. Cassini's 12 science instruments were designed to carry out sophisticated scientific studies of Saturn, from collecting data in multiple regions of the electromagnetic spectrum, to studying dust particles, to characterizing Saturn's plasma environment and magnetosphere. In Table 4.3 are reported the main mission data and events related to the Cassini–Huygens mission [82].

Table 4.3: Summary of the Cassini-Huygens mission, launched by Cape Canaveral Air Force Station, Florida.

Launch date	15 October 1997
Initial mass (Cassini)	5712 kg
Payload mass	617.39 kg (including the Huygens lander)
Propellant mass	2950 kg used out of 2978 kg
Final mass	2125 kg
Venus flybys	26 April 1998 (234 km) and 24 June 1999 (600 km)
Earth flyby	18 August 1999 (1171 km)
Jupiter flyby	30 December 2000 ($10 \cdot 10^6$ km)
Saturn arrival	1 July 2004
Travel time	7 years (≈ 2500 days)

The Cassini orbiter alone weighed 2125 kilograms, and the total mass of the Huygens probe was 349 kilograms, including payload (49 kilograms) and probe support equipment

on the orbiter (30 kilograms) [84]. On the 14 January 2005, the Huygens probe provided a detailed study of Titan's atmosphere during its 2.5 hour descent to the surface, relaying data and images from Titan's surface for another hour and 10 minutes [82]. The probe support equipment (PSE) remained attached to the orbiting spacecraft. The support equipment included the electronics necessary to track the probe, recover the data gathered during its descent and process and deliver the data to the orbiter. The data was then transmitted or downlinked from the orbiter to Earth. Three Radioisotope Thermoelectric Generators (RTGs) provided power for the spacecraft, including the instruments, computers, radio transmitters, attitude thrusters and reaction wheels. During the mission in this immense region, the Cassini spacecraft extensively photographed these moons, and collected data that increased our understanding of their composition. The Cassini spacecraft had two completely isolated propulsion systems [81]:

- Monopropellant System - Hydrazine (N2H4)
  16 Redundant ≈ 1 Newton thrusters, 4 per "cluster" Used for attitude control and small (< 0.3 m/s) trajectory control maneuvers

- Bipropellant system- Nitrogen Tetroxide (NTO)/Monomethylhydrazine (MMH); Main (445 Newton) engine for propulsive maneuvers – Burns can be blow-down or pressurized (with Helium), 183 main engine burns.

The main engine was used for spacecraft velocity and trajectory correction changes. To be on the safe side, there were two identical main engines: One was in use and the other was a backup. There were also 16 monopropellant hydrazine thrusters of which eight were prime and eight were backups. The thrusters were used for attitude control and also for small velocity-change maneuvers. The mission takes about 7 years to arrive at Saturn, with the use of the VVEJGA (Venus-Venus-Earth-Jupiter Gravity Assist) trajectory. Exploiting the VVEJGA the spacecraft must be designed to withstand the thermal environment both inside the orbit of Venus ($\approx 130°$C) and at Saturn ($\approx -210°$C). The gravity-assist flybys of the different planets are designed to increase the spacecraft's velocity relative to the sun so it can reach Saturn. During these planetary flybys, there is an exchange of energy between the planet and the spacecraft which accelerates the latter and changes its velocity direction relative to the Sun.
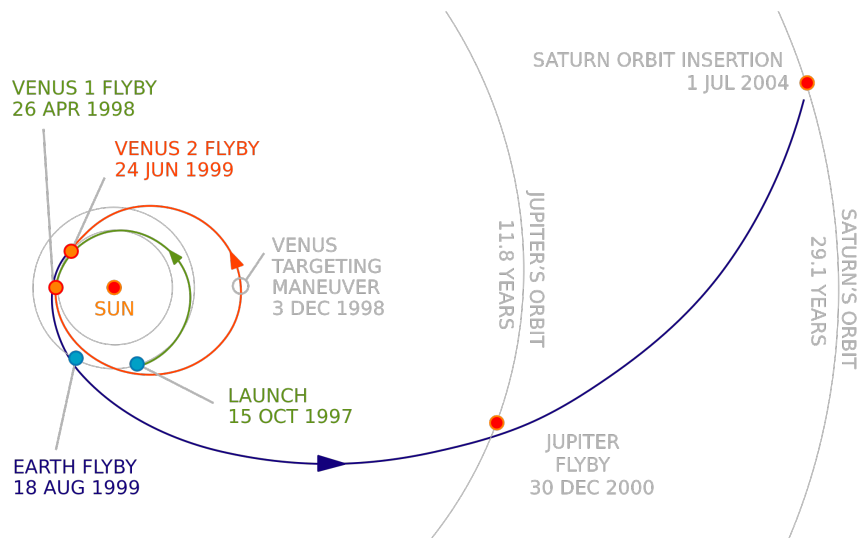
Figure 4.7: Cassini's interplanetary flight path beginning with launch from Earth on 15 October 1997, followed by gravity assist flybys of Venus (26 April 1998 and 21 June 1999), Earth (18 August 1999), and Jupiter (30 December 2000). Saturn arrival was on 1 July 2004. Credit: NASA / Jet Propulsion Laboratory - Caltech.

Cassini made its closest approach to Jupiter on 30 December 2000 ($9.6 \cdot 10^6$ km), receiving the final gravity boost needed to reach Saturn [85]. During the Saturn Orbit Insertion (SOI) maneuver the spacecraft reduced its velocity with respect to Saturn and crossed the Saturn's ring plane. This maneuver, which was approximately 90 minutes long, allowed Cassini to be captured by Saturn's gravity into a five-month orbit. Cassini's close proximity to the planet (24000 km) after the maneuver offers a unique opportunity to observe Saturn and its rings at extremely high resolution.
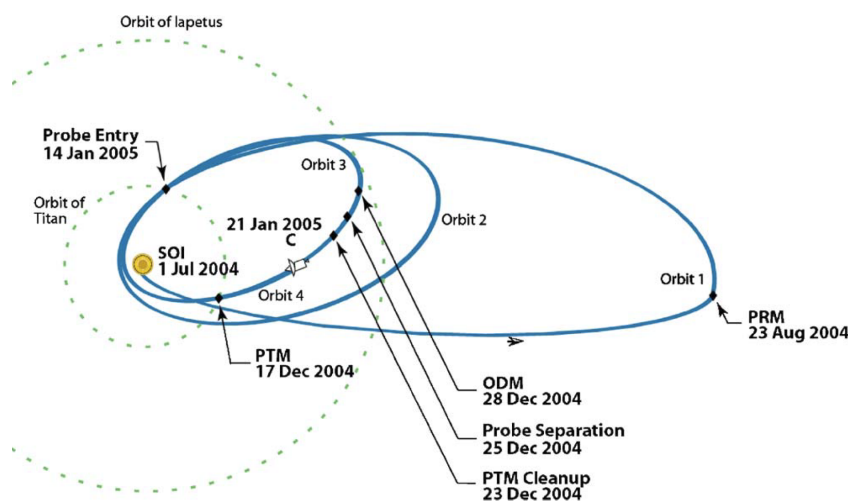
Figure 4.8: Cassini/Huygens' path from orbit insertion to probe entry [86].

4.5 Scenarios

In this section the philosophy adopted for the trajectory design for this thesis will be explained. Several approches have been taken into account to further analyze potential low thrust trajectories to Saturn-Titan system, starting from the estimated characteristics provided by PPPL and PSS related to the performance of the DFD. The purpose of the research was to study the feasibility of such kind of missions with a 2 MW class engine and to demonstrate the advantages related to this new propulsion system concept. The performance data shown in Table 4.4 have been considered.

Table 4.4: Performance of the Direct Fusion Drive

Fusion Power	2 MW
Specific Impulse	9600 s
Thrust	8 N
Specific Power	0.75 kW/kg
Thrust Efficiency	0.5

This section will focus on the several approches and the different scenarios considered.

4.5.1 Lambert impulsive trajectory

As a first step impulsive maneuvers have been considered, computing the solution for the Lambert problem using a MATLAB code [Appendix A], determining the impulse that produces the orbit connecting a departure state (inital position and velocity) with a subsequent arrival point related to the planet target (final position). Lambert's law is used for an array of start dates and time of flights (between 2 and 5 years for Titan mission), and a minimum ΔV is found. For instance, a 3-year trajectory with a start date in the next 30 years was found to require a ΔV between 37 and 46 km/s.
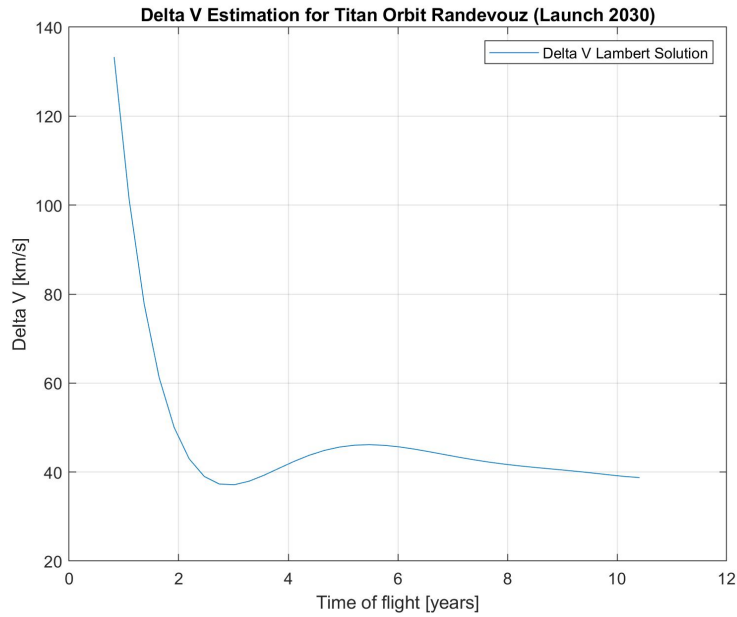
Figure 4.9: First estimation for total mission $\Delta - V$ required to reach Saturn.

Table 4.5 and Table 4.6 show the complete example mission, with the inputs in the first table and the outputs in the second. The planet positions are obtained for the date given using JPL's HORIZONS system which can be used to generate ephemerides for solar-system bodies.

Table 4.5: Lambert analysis example mission inputs

Launch Date	21 March 2045
Payload Mass	1000 kg
Flight Time	3 years
Total Fusion Power	2 MW
Thrust Efficiency	0.5
Engine Specific Power	0.75 kW/kg

Table 4.6: Lambert analysis example mission results

Lambert ΔV	39.1 km/s
Burn duration	280 days
Engine mass	2660 kg
Propellant mass	3250 kg
Total mission mass	7000 kg

The mass of the unburned propellant must be accelerated along the trajectory with the spacecraft itself. Minimizing the propellant mass required to achieve a given change in

83

velocity is essential. Therefore, an initial estimation of the mission masses has been calculated using a MATLAB code for iterations 5, using the Tsiolkovsky rocket equation:

$$\frac{m_f}{m_0} = e^{-\frac{\Delta V}{I_{sp}g_0}}. \tag{4.20}$$

As well known, Eq. (4.20) shows that for a rocket with a given empty mass and a given amount of fuel, the total change in velocity it can accomplish is proportional to the effective exhaust velocity. It is also important to consider that ncreasing the mission duration, thrust efficiency, exhaust velocity, or specific power all reduce the thrust and mass required for the mission. Increasing the payload obviously has the reverse effect. The following results have been obtained.
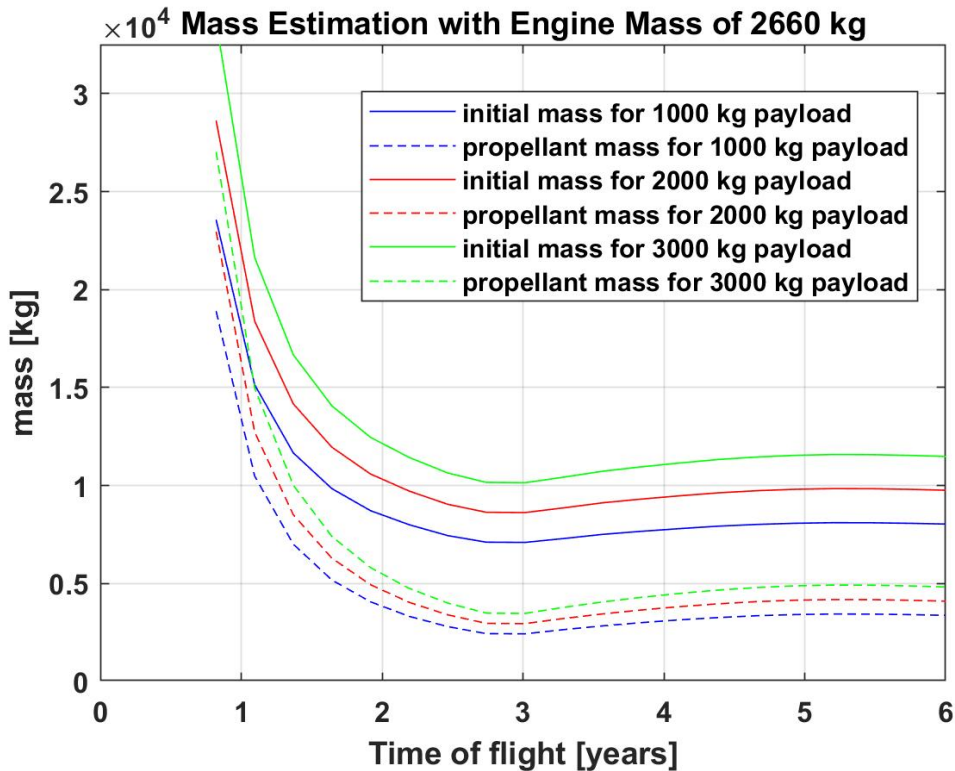
Figure 4.10: First mass estimation required to reach Saturn.

The mission masses are based on the estimations of specific power, thrust efficiency made by PPPL and PSS, and an initial payload estimation of 1000 kg. This requires an iteration on the thrust and fuel mass given a burn duration, for instance a 25% burn duration of the 3-year time of flight is 280 days. A $\Delta - V$ of about 40 km/s can be achieved with a thrust of 8 N and a specific impulse of about 9600 s with a total initial mass of less than 7000 kg, indicating initial feasibility. These first approximative estimations have been obtained in order to have good intial guess for the more precise finite maneuvers analysis necessary to obtain accurate results for this kind of low-thrust engine.

4.5.2 Titan mission

The scenarios related to the Titan mission are described in this section. The spacecraft consists of an orbiter vehicle and an atmospheric probe which will accomplish the mission through the atmosphere and on the surface of Titan. Two different profile missions have been considered: the first one is a thrust-coast-thrust profile with constant thrust and specific impulse and the second is a profile mission with continuous and constant thrust applied for the entire mission leading to a straight-line trajectory to Saturn. For the continuos thrust profile mission a switch in thrust direction is expected and operated in the second half of the trajectory. The objective of the mission is to reach Saturn near the descending node reffered to the ecliptic plane along its orbit around the Sun, in order to solve a nearly 2-D problem with huge advantage at numerical and computational level. Thereafter, when the spacecraft is orbiting around Saturn the Titan orbit insertion (TOI) maneuver concludes the mission scenario, enabling the Titan probe to enter in the atmosphere and land on the Saturn's moon surface.

4.5.3 Thrust-coast-thrust mission profile

The first scenario analyzed is a thrust-coast-thrust profile of the mission which has been analyzed and divided into four different phases: Earth departure, interplanetary trajectory, Saturn orbit insertion and Titan orbit insertion. Firstly, considering the simultaneous porpagation of both the Earth and Saturn orbits and taking into account the time constraint represented by the randezvous with the planet target, the mission start time has been estimated. For this randezvous problem the inputs are:

- Specific power;

- Thrust efficiency;

- Specific impulse I_{sp};

- Thrust T;

- Initial and final radii;

- Payload mass (initial guess);

- Spacecraft Total mass (initial guess).

After several iterations and considering some crucial constraints (related to the total mass of the spacecraft, for instance), estimations of travel time and the mission start time have been obtained.
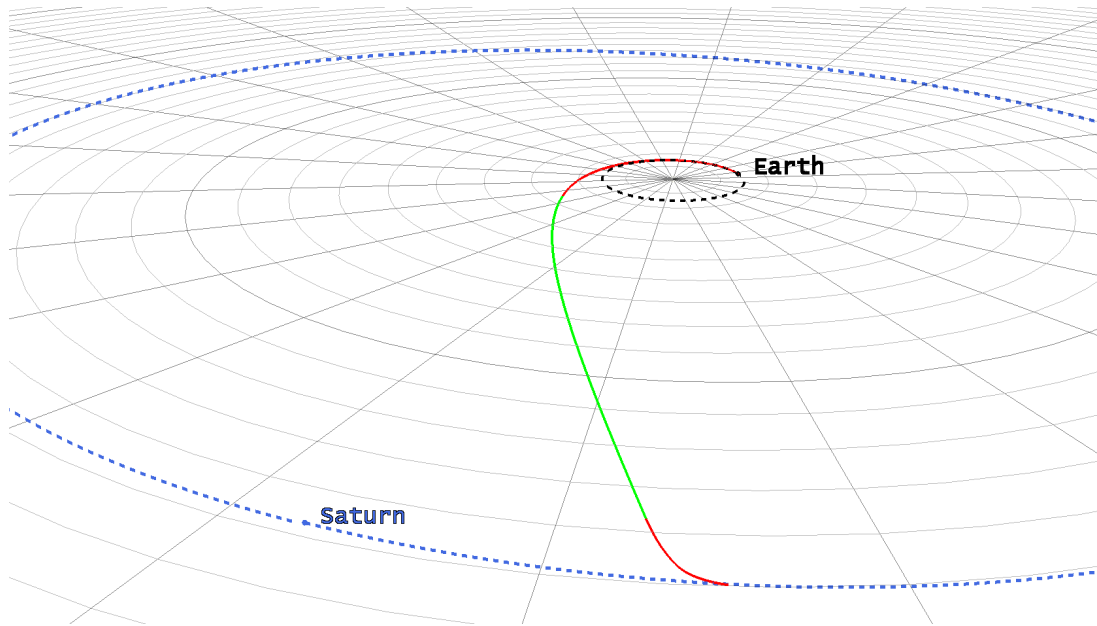
Figure 4.11: Thrust-coast-thrust profile for the Titan mission. It is possible to see three segments of the trajectory, the red curves suggest that the spacecraft thrust is active and the green line represents the coasting phase.

Figure 4.11 shows the three main phases of the mission which will be discussed apart. The first red curve starts from Earth initial position and contains both the escape maneuver from Earth and the burn which puts the spacecraft along the heliocentric hyperbolic trajectory to Saturn.

- Earth departure phase:

A logic solution for this first phase of the mission could be to insert the Titan spacecraft directly into heliocentric orbit. This required a Delta IV Heavy or other expendable heavy-lift launch vehicle. Our simulations show that an Earth departure from LEO uses little propellant mass and takes between 25 and 71 days depending on engine parameters and the initial mass considered. The results obtained are very close to those published by the PSS for the NASA innovative advanced concepts (NIAC) Program [66]. This alternative solution allows to use almost any launch vehicle, dramatically reducing launch and overall mission costs and also allows checkout and testing in low Earth orbit.
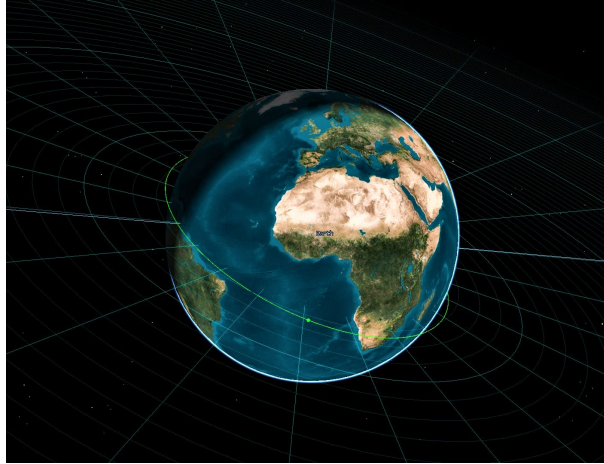
Figure 4.12: Initial LEO view.

The initial low Earth orbit considered is a circular orbit with an altitude of about 386 km and inclination of about 25 degree which allows to escape from Earth along the Ecliptic plane.

As a first step, we considered an Earth Point Mass model propagator which do not take into account Earth orbit perturbations and a simulation for the spiral trajectory has been performed in order to evaluate propellant mass consumption and maneuver time to escape from Earth gravitational sphere of influence. We obtained the following results related to the Earth escape maneuver using the Engine model "DFD definitivo" created on STK software with the performance listed in Table 4.4.

Table 4.7: Earth departure spiral results obtained considering a simple Earth point mass model on STK software.

LEO initial orbit start time	2 Nov 2046 12:03:59
First phase final time	17 Jan 2047 17:23:10
First phase maneuver duration	76.222 days
Initial spacecraft mass	7250 kg
Propellant mass used	559.65 kg
ΔV magnitude	7.562 km/s

Considering the Earth HPOP Default v10, a more accurate finite propagator, Earth perturbations have been taken into account. The conclusion of this analysis results in a negligible higher amount of propellant mass and maneuver time, as can be seen from the Table 4.8. Therefore, it was decided to neglect this kind of perturbation for this realitvly short maneuver.

Table 4.8: Earth departure spiral results obtained considering the Earth HPOP Default v10 finite propagator on STK software.

LEO initial orbit start time	2 Nov 2046 12:03:59
First phase final time	17 Jan 2047 17:23:10
First phase maneuver duration	76.39 days
Initial spacecraft mass	7250 kg
Propellant mass used	560.81 kg
ΔV magnitude	7.581 km/s

Moreover, an iterative process has been performed in order to minimize the amount of propellant mass necessary for the escape maneuver, using the sparse nonlinear optimizer (SNOPT), a software package for solving large-scale optimization problems. The thrust vector, updated during burn, has been obtained using the VNC Axes, discussed in Sec. 4.1, centrated in the barycenter of the spacecraft as the reference system for the the thrust vector, an optimal thrust direction has been obtained along the velocity vector with a small positive radial component.

Table 4.9: Earth departure spiral results achieved using the sparse non-linear optimizer (SNOPT) on STK software.

LEO initial orbit start time	2 Nov 2046 01:00:00
First phase final time	17 Jan 2047 17:19:16
First phase maneuver duration	76.2 days
Payload Mass	1800 kg
Initial spacecraft mass	7250 kg
Propellant mass used	559.5 kg
ΔV magnitude	7.562 km/s
Initial velocity (Earth)	7.676 km/s
Final velocity (Earth)	1.518 km/s

It is essential to emphasize that the spacecraft should escape from the Earth gravitational sphere of influence with a velocity, respect to Earth itself, parallel to the Earth's orbital velocity vector (with respect to the Sun), before entering in the interplanetary space. This tangential condition is essential in order to take full advantage of the Earth's orbital velocity ($V_{CE_1} \approx 30$ km/s). Therefore, as a consequence of a long iterative process which depends by several variables involved in all the mission phases, the maneuver start time has been obtained considering a given waiting time in LEO.
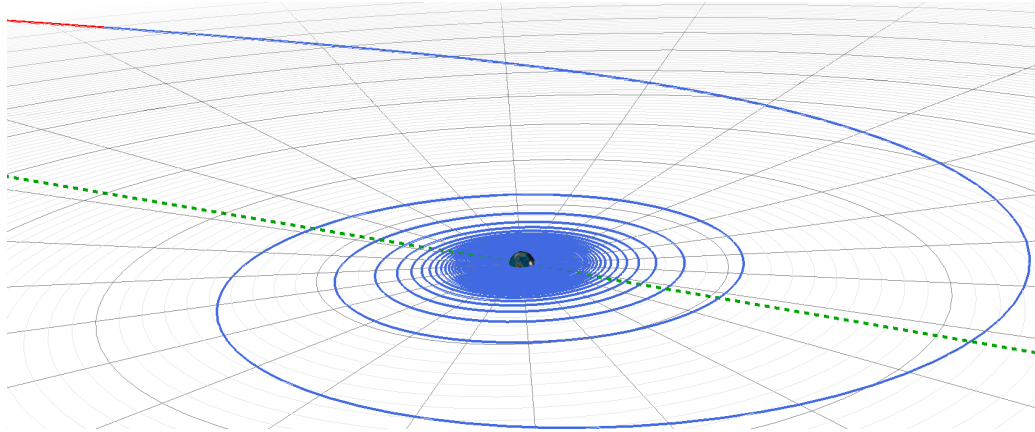
Figure 4.13: Spiral Trajectory for the escape maneuver (blue) in an Earth centered reference system. The red line starts when the spacecraft is outside the Earth gravitational sphere of influence, moving into interplanetary space.

Due to the electromagnetic nature of the engine and because of safety reasons for the spacecraft itself, is preferable to spend less time possible inside the Inner Van Allen Belt. The time spent in the Van Allen belt is about 17 days (inner radiation belt) and it is calculated as the time between 1000 and 6000 km altitude. One can say that lower thrust significantly increases the spiral time but only modestly affects the fuel consumption considering the same specific impulse (exhaust velocity). Besides, a lower specific impulse significantly increases the fuel consumed with a negligible influence on the spiral time. In order to perform the escape maneuver a fixed-step integration has been adopted, which stops when the spacecraft reachs the external surface of the gravitational sphere of influence of the Earth (whose radius $r_{\oplus_\infty} \approx 10^6$ km) with the constraint on the angle between the velocity vectors previously anticipated. The escape maneuver ends when the eccentricity $e = 1$ on 12 Jan 2047 08:10:50 after 71 days of burn with a propellant consumption of about 520 kg. Figure 4.14 shows the spacecraft velocity magnitude respect to the Earth and Sun, it is possible to evaluate the spacecraft velocity as a function of time and when, evading from Earth, is under the "only" influence of the Sun.
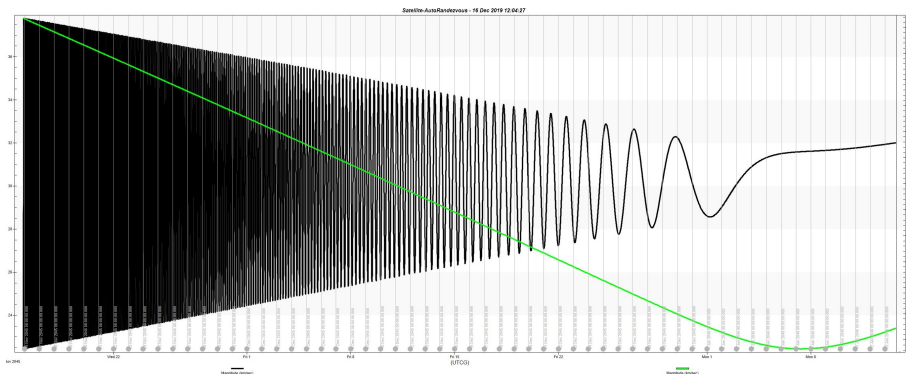
Figure 4.14: Spacecraft velocity magnitude respect to Earth and Sun during the Earth escape spiral trajectory.

The Saturn trajectory, the next mission phase, is the continuation of this first maneuver, since the engine still generates thrust exiting from the Earth gravitational influence, orbiting around the Sun. Subsequent to the exit from Earth sphere of influence, the spacecraft is in an elliptic orbit around the Sun. Many days of acceleration are needed at this point to obtain a Heliocentric hyperbolic orbit, and the thrust vector is once again aligned with the velocity of the spacecraft.

- Interplanetary trajectory & Saturn orbit insertion:

In order to perform a transfer from an orbit to another, a change in velocity ΔV is required. The most desirable maneuver could be the one that requires less time or the one that requires less fuel consumption (so minimum ΔV), depending on the mission needs. The first deep space maneuver (DSM) is essentially the continuation of the previous finite maneuver and it has been derived from an iteration process where the launch date, maneuver duration and thrust components were the indipendent variables and the main purpose was to find an optimal solution with the minimum fuel consumption. As a first step, the main goal was to reach a spatial region on the ecliptic plane, near to the descending node of Saturn's heliocentric orbit, simultaneously with the planet target disregarding any deceleration phase. As results of these iteration steps other estimations have been obtained involving also the first phase's iteration process (launch date, for instance). Moreover, it is necessary to include a proper deceleration maneuver relatively close to the planet target ensuring the spacecraft and Saturn velocities to be considered comparable. This means that because of the negative acceleration of the spacecraft and the relatively high Saturn's velocity a certain delay shall be taken into account. Then, it is essential to point at a temporally preceding target along Saturn orbit, preventing the delay, increasing the acceleration burn duration and/or modifying the thrust vector direction. This complex problem has been solved trying to minimize the propellant mass required to meet the time requirements just mentioned. A minimum time of burn for the acceleration phase has been obtained and in this case the thrust vector is alligned to the spacecraft velocity vector (reference Sun) and as a consequence it enables to perform a hyperbolic trajectory with respect to the Sun. Relatively close to Saturn, the second DSM (Saturn orbit insertion) conclude this mission phase and puts the spacecraft into a Saturn centered orbit. A 1.6-year-long coasting phase is expected between the initial and final maneuvers. More specifically, the results for each mission phases are shown in Tables 4.10, 4.11 and 4.15, respectively.

Table 4.10: Heliocentric orbit: results for the first deep space maneuver (acceleration phase) achieved using the sparse non-linear optimizer (SNOPT) on STK software in order to minimize the propellant consumption.

Propagator model	Heliocentric
DSM start time	17 Jan 2047 17:19:16
DSM final time	27 May 2047 19:43:16
Maneuver duration	130.1 days
Total mass at beginning	6690.4 kg
Propellant mass used	955.18 kg
ΔV magnitude	14.503 km/s
Initial velocity (Sun)	31.786 km/s
Final velocity (Sun)	34.560 km/s

Table 4.11: Heliocentric orbit: results for the coasting segment calculated with STK software.

Propagator model	Heliocentric
Coasting start time	27 May 2047 19:43:16
Coasting duration	1.67 years (610 days)
Total mass	5735.22 kg
Initial velocity (Sun)	34.560 km/s
Final velocity (Sun)	19.659 km/s

In the first trajectory estimation the spacecraft reachs Saturn's ascending node quite simultaneously without any deceleration. As previously anticipeted, in order to orbit around Saturn a deceleration phase is necessary. At arrival, however, the heliocentric transfer orbit usually crosses the target planet's orbit at some angle, ϕ as shown in Fig. 4.15. One can say that the spacecraft velocity and the orbital speed of the target planet should be comparable in magnitude and with a relatively small angle between them.
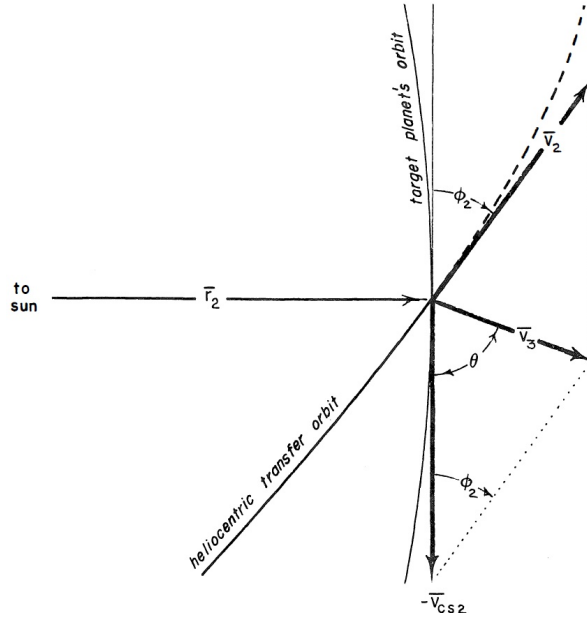
Figure 4.15: Fundamentals parameters for randezvous mission. The ϕ_2 angle is between the spacecraft velocity vector trlative to the Sun and the orbital speed of the target planet at arrival, V_{CS_2} is the orbital speed of the target planet and V_3 the velocity of the spacecraft relative to the target planet [69].

Otherwise, the spacecraft is not captured by the planet target but only a variation of the trajectory (fly by or gravity assist) occours with a net accelerative effect which could be positive or negative depending on the angle θ and the velocity of the spacecraft relative to the target planet. As a first step, a simple impulsive problem has been considered in order to evaluate the hyperbolic excess velocity V_3 on the approach hyperbola to Saturn and other physical parameters. This important estimations are necessary to have the more accurate possible initial guesses for the finite numerical analysis. Therefore, the angle θ in Figs. 4.15 and 4.16 may be determined from the law of sines as

$$\sin\theta = \frac{V_2}{V_3}\sin\phi_2. \tag{4.21}$$

In order to insert into Saturn's orbit, it is advantageous that the spacecraft cross the planet's orbit a distance x (miss distance) behind of the planet as shown in Fig. 4.16. Thereby, it is possible to perform a smaller decelerative maneuver (lower propellant consumption) reaching the target gravitational sphere of influence with a higher velocity and chasing it. Therefore, the hyperbolic excess velocity V_3 is offset a distance y from the center of the target planet and the distance of closest approach or periapsis radius may be computed. From Fig. 4.16 is possible to see that

$$y = x\sin\theta. \tag{4.22}$$

92
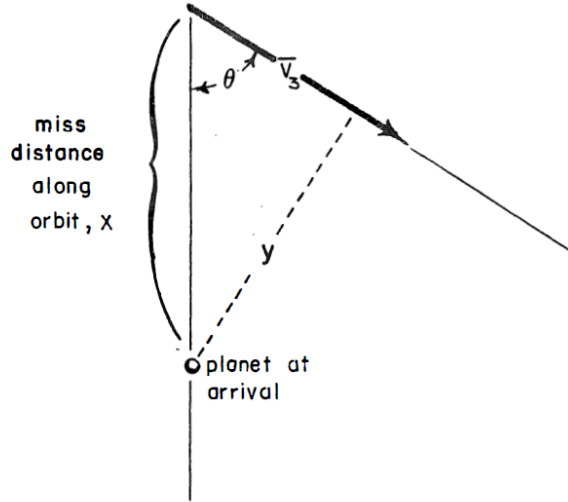
Figure 4.16: Offset miss distance at arrival in Saturn reference system [69].

In Fig. 4.17 a hyperbolic approach trajectory is shown, where V_3 is the velocity upon entrance to Saturn's gravitational sphere of influence ($r_{Hill} \approx 6.5 \cdot 10^7$ km) and y is the offset distance. As well known, considering the energy equation in the case of hyperbolic approach trajectory, Eq. (4.3), is possible to neglect the potential term

$$\varepsilon = \frac{V_3^2}{2} - \frac{\mu_t}{r_\infty} \approx \frac{V_3^2}{2}, \tag{4.23}$$

where μ_t is the gravitational parameter of the target planet. The angular momentum $\mathbf{h}$ is conserved along the orbit and it is obtainable as the product of the velocity and radius vectors as

$$\mathbf{h} = \mathbf{r} \times \mathbf{v} = constant, \tag{4.24}$$

and from simple geometric properties is easy to obtain

$$\mid h \mid = y \cdot V_3. \tag{4.25}$$

The *semi-latus rectum* p and eccentricity e and the periapsis radius r_p of the approach trajectory follow from

$$p = \frac{h^2}{\mu_t}, \tag{4.26}$$

$$e = \sqrt{1 + 2\varepsilon \frac{h^2}{\mu_t}}, \tag{4.27}$$

$$r_p = \frac{p}{1+e}. \tag{4.28}$$

Therefore, because the angular momentum is conserved, considering the periapsis

$$\mid h \mid = r_p V_p, \tag{4.29}$$

93

and the speed at periapsis is simply

$$V_p = \frac{y \cdot V_3}{r_p}.$$ (4.30)

Specifying the desired periapsis radius, the required offset distance y can be computed starting from Eq. (4.30) and equating the energy at periapsis with the energy upon entrance to the sphere of influence

$$\varepsilon \approx \frac{V_3^2}{2} = \frac{V_p^2}{2} - \frac{\mu_t}{r_p}.$$ (4.31)

Finally, solving Eq. (4.31) for V_p and substituting into Eq. (4.30), we obtain:

$$y = \frac{r_p}{V_3}\sqrt{V_3^2 + \frac{2\mu_t}{r_p}}.$$ (4.32)
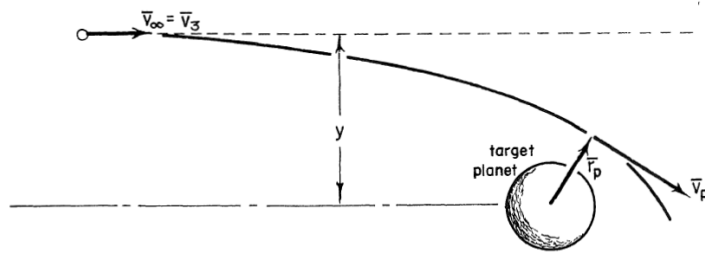
Figure 4.17: Hyperbolic approach orbit in Saturn reference system [69].

In particular, equating the periapsis radius to the radius of the target planet r_t in Eq. (4.32), it is possible to evaluate the so-called "impact parameter" b, since any offset lower than this will result in a collsion. Then, it is reasonable to assign to the target planet an impact size which is larger than its physical size. This concept is similar to the cross-section treatment employed by nuclear physicists and is called "effective collision cross section". The radius of the effective collision cross section is just the impact parameter, b. The impact parameter can be determined as

$$b = \frac{r_t}{V_3}\sqrt{V_3^2 + \frac{2\mu_t}{r_t}}.$$ (4.33)

The effective collision cross section of the planet represents a rather large target as shown in Fig. 4.18.
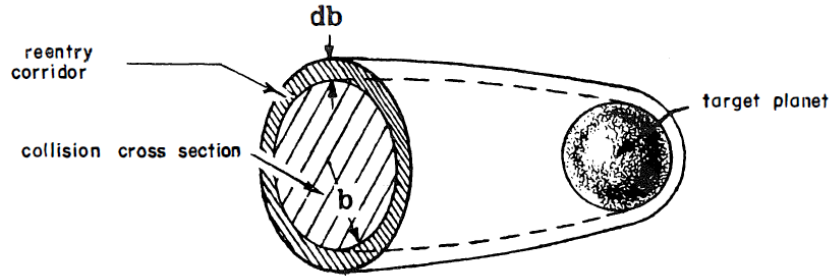
Figure 4.18: Effective cross section rapresentation, where b is the radius of the effective collision cross section (impact parameter) and the thin *annulus* of radius b and width db (*re-entry corridor*)is related to the possibility to take advantage of the target atmospheric braking [69].

Knowing the gravitational parameter of Saturn which is $\mu_s = 3.793 \cdot 10^7$ km^3/s^2, the planet radius $r_t = 60268$ km and assuming a hyperbolic excess velocity $V_3 \approx 12$ km/s the impact parameter is $b \approx 200000$ km. The Titan orbital parameters are listed in Table 4.12.

Table 4.12: Titan mean orbital parameters considering for convenience the ecliptic plane as reference for the inclination.

Semi-major axis	$1.222 \cdot 10^6$ km
Radius of periapsis	$1.187 \cdot 10^6$ km
Radius of apoapsis	$1.257 \cdot 10^6$ km
Eccentricity	0.02876
Inclination	13.8 deg
Average orbital speed	5.5 km/s
Titan gravitational parameter	8978.52 km^3/s^2
Titan Radius	2574.73 km

It is convenient to consider the Titan orbital parameter in order to initially define the periapsis radius r_p of the approach trajectory. Because of Titan mean distance from the center of Saturn, a comparable value has been assumed for the distance of closest approach ($r_p \approx 3 \cdot 10^6$ km). An iterative process is required in order to estimate the velocity respect to Sun when entering in the Saturn influence V_2 which is clearly strongly bound to the spacecraft velocity relative to Saturn V_3. As previously anticipated, a good intial guess for the arrival velocity is higher, but comparable to the descending node Saturn's orbital speed which is $V_{CS_2} = 9.17$ km/s. For instance, considering this kind of impulsive problem and starting with an hyperbolic excess velocity $V_3 = 12$ km/s and a distance of closest approch (radius) of about $3.5 \cdot 10^6$ km the periapsis radius velocity would be $V_p \approx 34$ km/s which is too high in order to stay in orbit around Saturn, especially if compared with the target velocity (Titan orbital speed). Considering an impulsive maneuver, the hyperbolic excess needed to achieved an acceptable orbital speed would be 1.5 km/s, meaning a change in velocity of about 10 km/s before entering in the Saturn sphere of influence.

This great change in velocity is not achieveable only decelerating the spacecraft, but also changing the direction of the velocity relative to the Sun, in fact, V_3 is the result of the product between vectors (Saturn orbital speed and spacecraft velocity relative to Sun). Finally, analysing the problem taking into account finite maneuvers, both deceleration and direction change have been studied. Starting with this higher entrance velocity, the main purpose of the orbit insertion maneuver, the second deep space maneuver (DSM), is to obtain a certain velocity vector which allows to orbit around Saturn at a radius comparable to those of Titan. During orbiting and interplanetary missions it is usually necessary to perform maneuvers so as to attain prescribed boundary conditions. Such boundary conditions result in an orbit or trajectory which the spacecraft must be on at the termination of the maneuver. In fact, the spacecraft is initially on a hyperbolic trajectory and it is required that after the maneuver it is in an elliptical orbit about the target planet. In order to evaluate the propellant consumption relative this kind of maneuver a numerical analysis, which takes into account finite maneuvers is required. As previously discussed, it is possible to achieve the desired hyperbolic excess velocity V_3 (relative to Saturn) not only decelerating but also turning the spacecraft velocity vector relative to the Sun $V_{S/C_{sun}}$, acting on the radial component of the thrust vector. If the angle between $V_{S/C_{sun}}$ and the Saturn orbital speed V_{CS_2} decrease, the resulting hyperbolic excess velocity rotates and decrease in magnitude as noticeble in Fig. 4.15. Therefore, in order to avoid an excessive deceleration which would extend the mission time, a trade-off between time requirements and propellant mass consumption allows to find a solution. The three components of the finite maneuver have been calulated, considering that this DSM shall start a certain time before the spacecraft enter in the Saturn's gravitational sphere of inluence. Near the end of the first maneuver segment the spacecraft is entering in the planet sphere of influence and starts to be increasingly attracted.

Table 4.13: Results for the first segment of DSM 2 achieved using the sparse non-linear optimizer (SNOPT) on STK software. The thrust components have been calculated using the VNC reference system relative to the Sun and are listed as components of a unit vector.

Propagator model	Heliocentric
DSM start time	26 Jan 2049 19:43:16
Maneuver duration	77 days
Velocity direction	-0.91497
Normal direction	0.027449
Co-Normal direction	-0.402587
Propellant mass used	565.330 kg
ΔV magnitude	9.769 km/s
Initial velocity (Sun)	19.659 km/s
Final velocity (Sun)	10.374 km/s

Table 4.14: Results for the second segment of DSM 2 achieved using the sparse non-linear optimizer (SNOPT) on STK software. The thrust components have been calculated using the VNC reference system relative to the Sun and are listed as components of a unit vector.

Propagator model	Heliocentric
DSM start time	13 Apr 2049 19:43:16
Maneuver duration	65.2 days
Velocity direction	0
Normal direction	-0.0099
Co-Normal direction	-0.9999
Propellant mass used	478.695 kg
ΔV magnitude	9.147 km/s
Initial velocity (Sun)	10.374 km/s
Final velocity (Sun)	13.780 km/s

Table 4.15: Results for the entire second deep space maneuver achieved using the sparse non-linear optimizer (SNOPT) on STK software.

Propagator model	Heliocentric
DSM start time	26 Jan 2049 19:43:16
Maneuver duration	142.2 days
Total mass at beginning	5735.22 kg
Propellant mass used	1044 kg
ΔV magnitude	18.9 km/s
Initial velocity (Sun)	19.659 km/s
Final velocity (Sun)	13.780 km/s

It is worth to underline that the spacecraft approachs Saturn shortly after the descending node in order to orbit very close to Titan with less propellant consumption, taking advantage of Saturn's vertical motion relative to the ecliptic plane. Notice that the SOI has a small normal component which allows to achieve the same inclination and RAAN of Titan orbit, as shown in Fig. 4.19 . Then, when the spacecraft orbits around Saturn on the same orbital plane of the target, the problem is once again bidimensional with the same numerical and computational advantages discussed before.
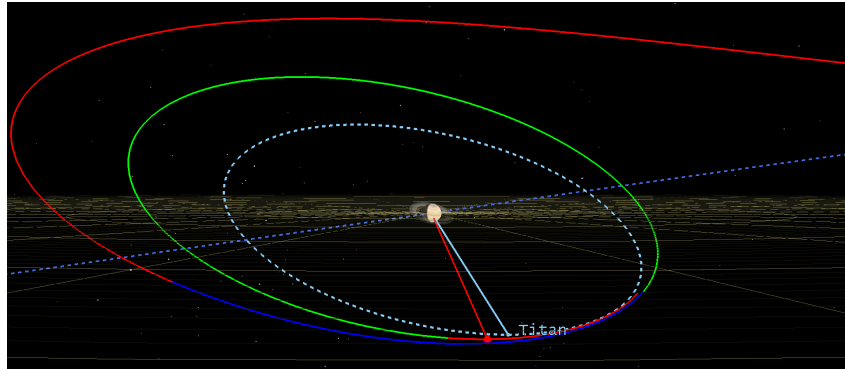
Figure 4.19: Saturn orbit insertion maneuver. The red segment rapresents the finite maneuver which let the spacecraft orbit (green) around Saturn very close to Titan. The blue line marks the start of the TOI maneuver.
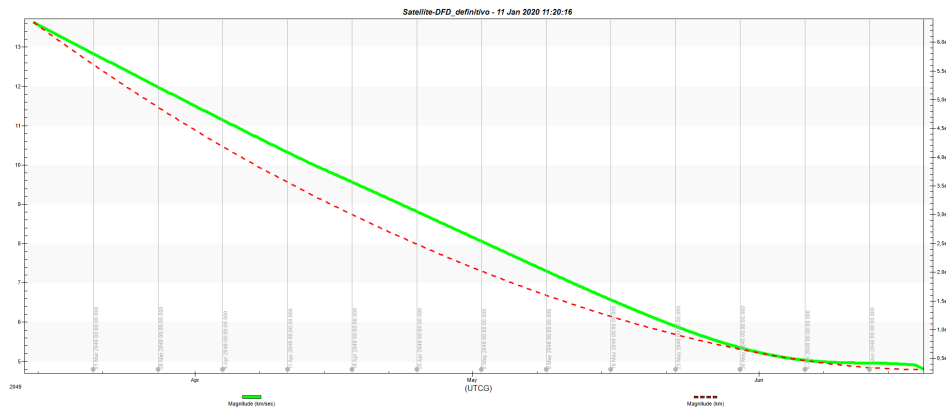
Figure 4.20: Spacecraft velocity relative to Saturn from the entrance in the gravitational sphere of influence (hyperbolic excess velocity V_3, green curve) to the radius of closest approach. The red dashed line represents the decreasing distance from Saturn.
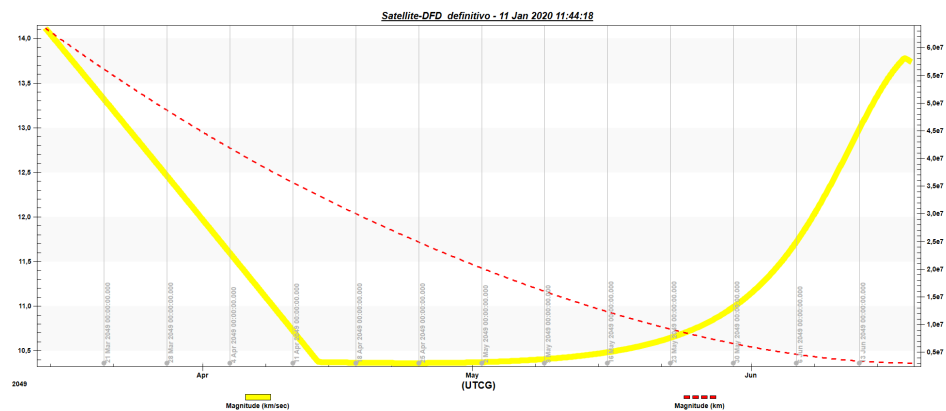
Figure 4.21: Spacecraft velocity relative to the Sun from the entrance in the gravitational sphere influence of Saturn V_2 (yellow curve) to the radius of closest approach. The red dashed line represents the decreasing distance from Saturn.

98

Once the spacecraft is captured by Saturn, a possible solution is to insert the spacecraft into a proper orbit and wait the optimal time to start the next DSM which inserts the spacecraft in a Titan centered orbit. The orbital parameters related to this "waiting" orbit around Saturn are shown in the following Table:

Table 4.16: Central body: Saturn, Orbital parameter after the orbit insertion.

Saturn gravitational parameter	$3.793 \cdot 10^7$ km^3/s^2
Radius of Periapsis	$3.05 \cdot 10^6$ km
Radius of Apoapsis	$9.4 \cdot 10^6$ km
Semimajor axis	$6.2 \cdot 10^6$ km
Eccenticity	0.5
RAAN	270.2 deg
Orbital Period	185 days
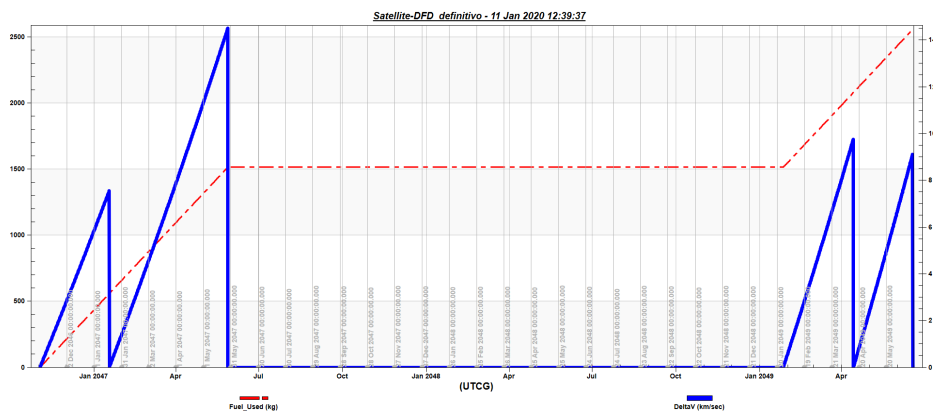
Figure 4.22: Propellant mass consumption and ΔV magnitude during mission time travel until Saturn orbit insertion.
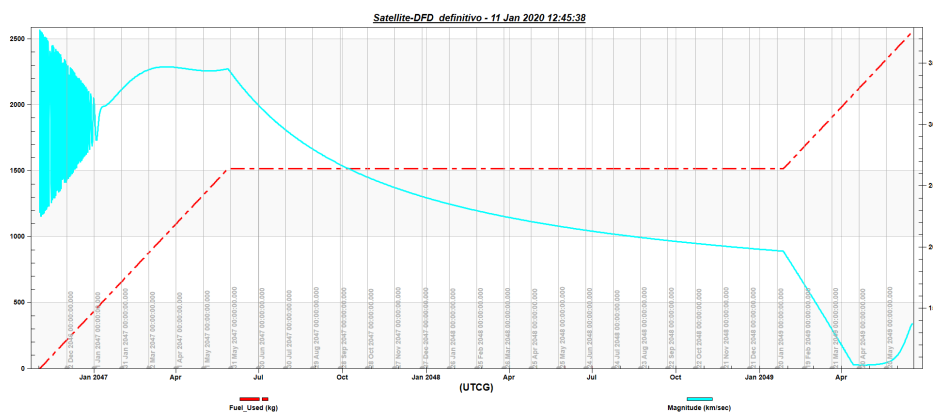
Figure 4.23: Propellant mass consumption and spacecraft velocity relative to the Sun during mission time travel until Saturn orbit insertion.

99

- **Titan orbit insertion**

Starting from the waiting orbit around Saturn a set of maneuvers are necessary to reach Titan. In order to properly deal the mutual gravitation interaction between Saturn, Titan and the spacecraft it is necessary to introduce the three-body problem. No general solution of this problem (or the more general problem involving more than three bodies) is possible. A description of the time-dependent behavior of three gravitationally interacting bodies was first mathematically formalized in 1687 by Issac Newton in his foundational work *PhilosohphæNaturalis Principae Mathematica* [87]. This problem consists of determining the perturbations (disturbances) in the motion of one of the bodies around the principal, or central, body that are produced by the attraction of the third. The motion of the Moon around the Earth, as disturbed by the action of the Sun is a classic example. The problem can be solved for some special cases, for example, those in which the mass of one body, as a spacecraft, can be considered infinitely small. In order to numerically solve the problem and obtain accurate results, a High-Precision Orbit Propagator (Titan HPOP Default v10) was created, which uses numerical integration of the differential equations of motions to generate ephemeris taking into account the gravitational influence of Saturn and the Sun. At the end of the deep space maneuver (Saturn orbit insertion), the spacecraft has time to collect precious scientific data related to Saturn, orbiting for about 170 days before starting the last mission maneuvers. The purpose of this phase is not only to achieved very similar orbital parameters to those of Titan, but also to perform a randezvous. Therefore, a strong temporally constraint has to be considered to solve the problem. The following maneuver strategy has been adopted:

- first finite burn: thrust directed along the anti-velocity direction;

- zero-thrust segment;

- phasing maneuver: active thrust components along anti-velocity and co-normal direction;

- final Titan orbit insertion maneuver.

As formerly stated, it is more convenient to perform a radial maneuver for the lowest speed. Initially, the orbital parameters achieved shall be different from the Titan ones in order to perform the required phasing maneuver within a reasonable amount of time. It is possible to observe in Figure 4.24 the portion of the waiting orbit (green) travelled by the spacecraft before the phasing maneuver starts (red). The phasing angle, which is the angle between the spacecraft position vector $r_{S/C}$ and Titan r_t, with respect to Saturn, decreases during the maneuver because of the different orbits travelled by the chaser and the target resulting in different velocities.
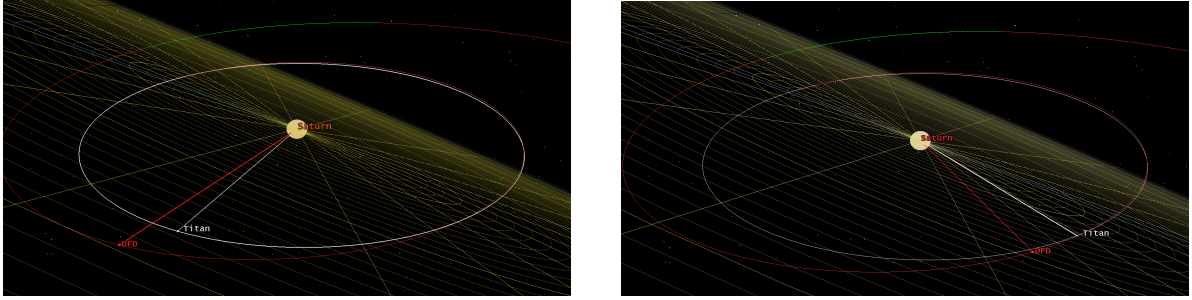
Figure 4.24: Central body: Saturn. The initial part of the required phasing maneuver is shown, where the phasing angle between the spacecraft position vector $r_{S/C}$ (red) and Titan's position (white) decreases during the maneuver.
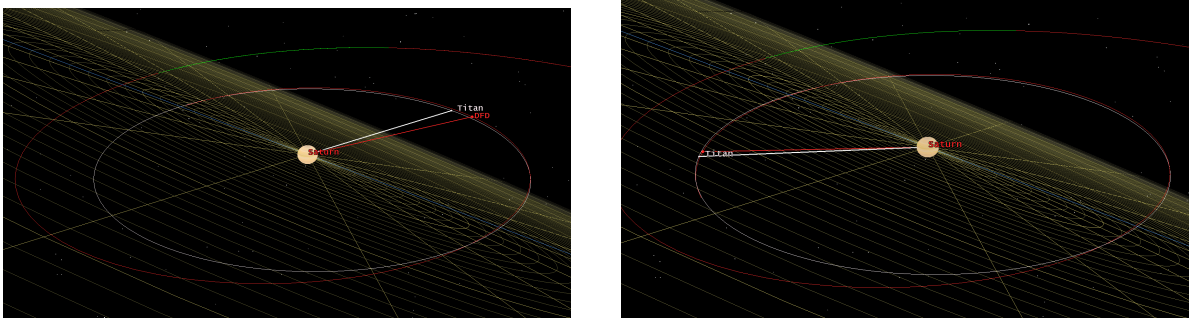
Figure 4.25: Central body: Saturn. The final part of the required phasing maneuver is shown, where the spacecraft reachs the target planet with the proper velocity vector with respect to Titan.

Table 4.17: Results related to the required insertion maneuver which let the spacecraft (chaser) reachs Titan (target), orbiting around Saturn.

Propagator model	Saturn propagator
DSM start time	15 Dec 2049 00:31:16
Maneuver duration	33.5 days
Total mass at beginning	4661.82 kg
Propellant mass used	77 kg
ΔV magnitude	1.569 km/s
Initial velocity (Saturn)	4.163 km/s
Final velocity (Saturn)	3.05 km/s
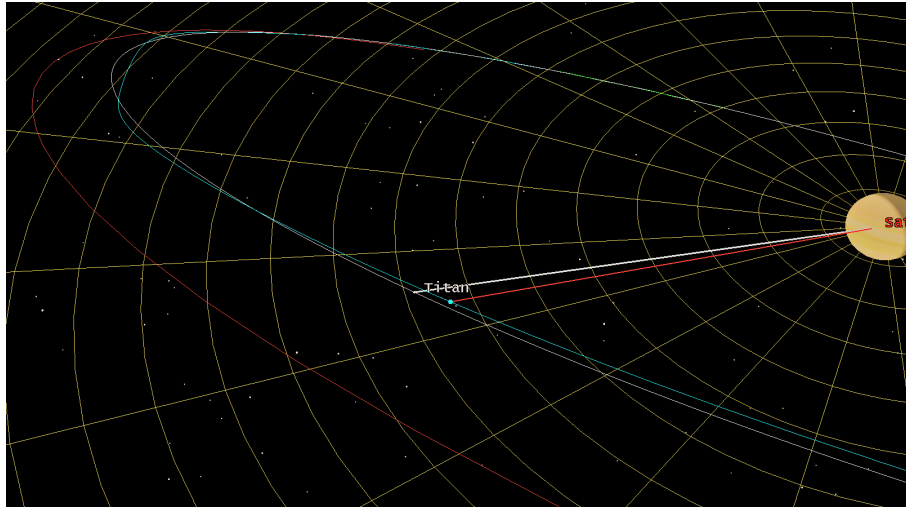
Figure 4.26: The initial part of the Titan orbit insertion phase is shown, where the spacecraft entering in the gravitational sphere of influence starts to orbit around the target.
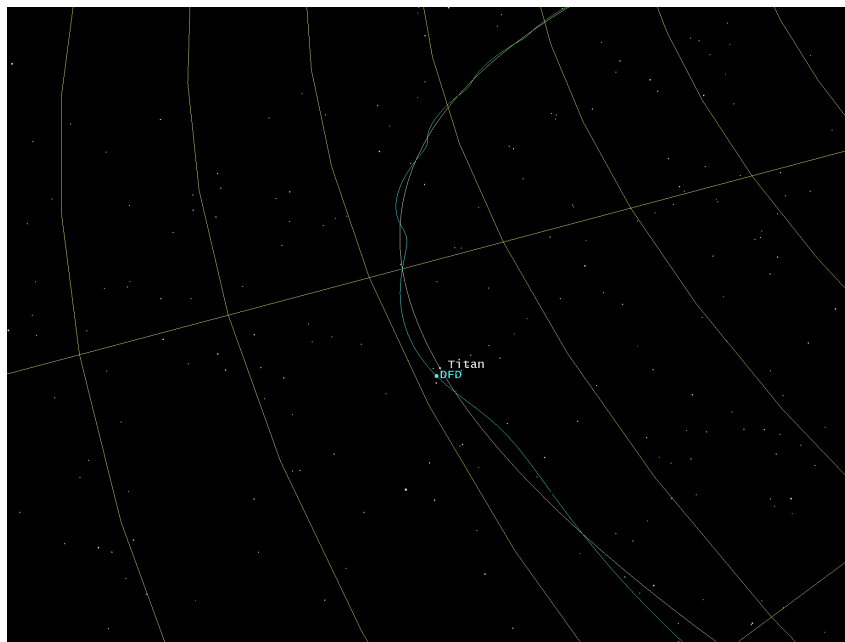
Figure 4.27: Saturn centered reference system: correction maneuvers are required in order to achieve the desired orbital parameters relative to Titan.

Once the spacecraft reachs Titan with the proper relative velocity, the final Titan orbit insertion maneuver starts, achieving a Titan centered circular orbit 4000 km away from the surface, as shown in Figs. 4.28 and 4.29. This altitude meets the scientific instruments requirements and provides stability to the orbit, requiring less station keeping maneuvers related to Saturn's perturbations, which can be usefull to freely vary the orbit.
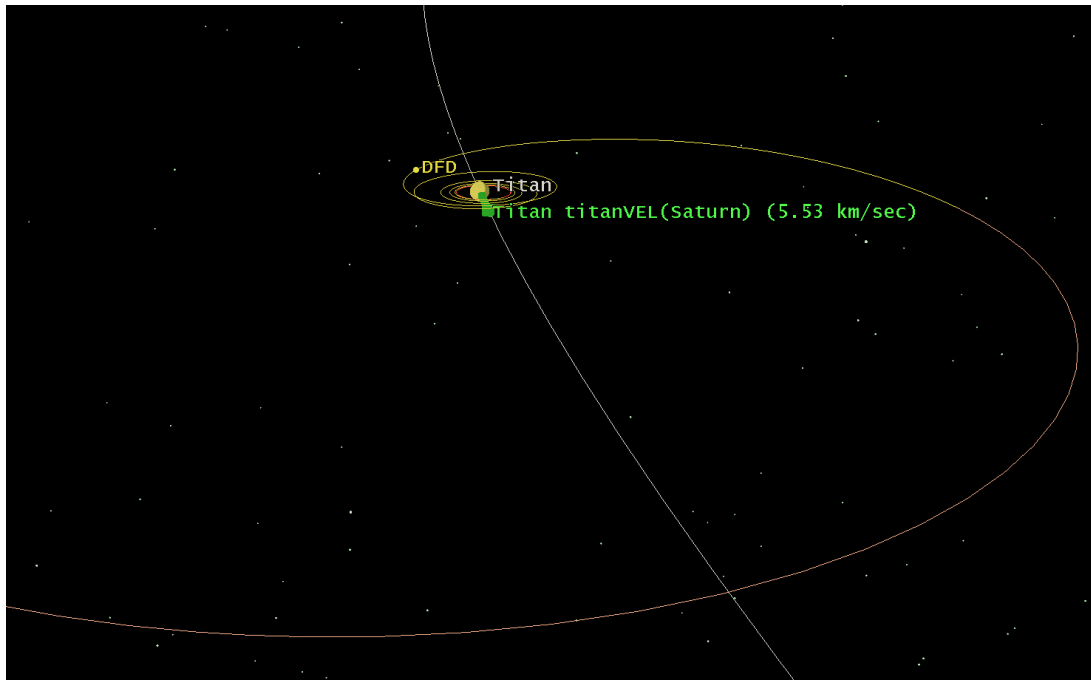
Figure 4.28: Titan orbit insertion from a Titan centered inertial reference system. After the phasing maneuver, the yellow line starts the orbit insertion maneuver which results in the final orbit around Titan (red).
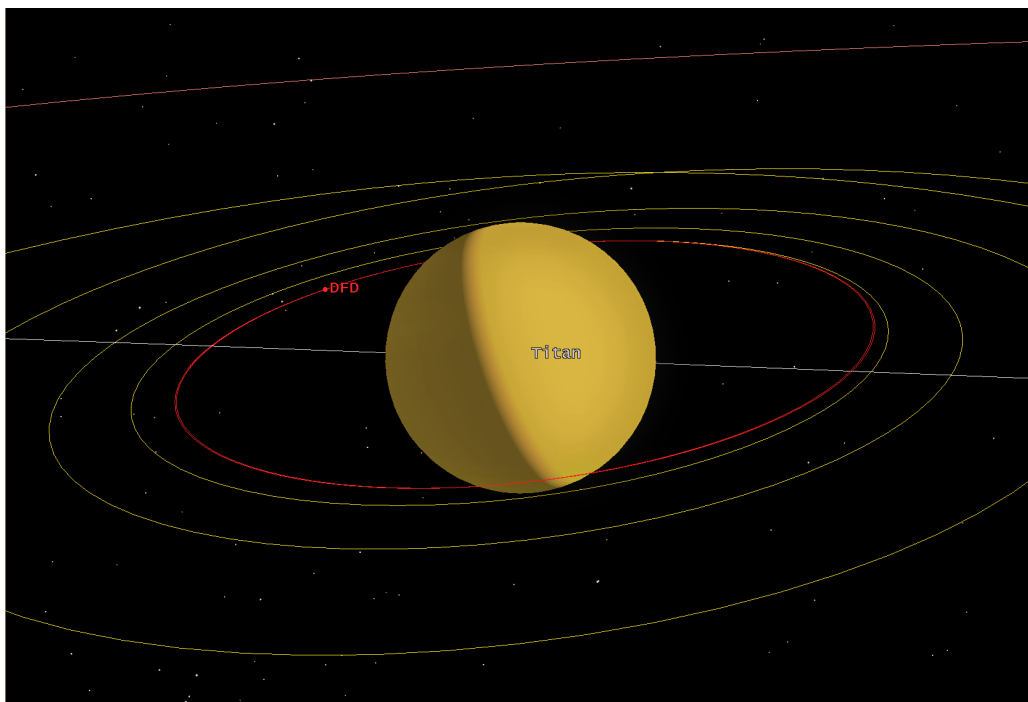
Figure 4.29: Titan orbit insertion from a Titan centered inertial reference system. The final orbit around Titan (red) distance is approximately 4000 km from the surface.

Table 4.18: Orbital parameters for the fianl orbit, using an inertial Titan centerd reference system.

Propagator model	Titan HPOP Default v10
Semi-major axis	6995 km
Radius of periapsis	5567 km
Radius of apoapsis	8422 km
eccentricity	0.2
Inclination	9 deg
Average orbital speed	1.2 km/s
Orbital period	0.448 days
Titan Radius	2574.73 km

In summary, the thrust-coast-thrust profile mission is based on the assumption that the DFD could be capable of turning off and on the thrust generation. This is an important hypothesis which requires that the engine will not produce thrust for about a year during the coasting phase, which is in theory possible but not yet certain. More specifically, because of the robotic nature of the mission, it could be possible to think to turn off the engine in order to save precious fuel (^{3}He); otherwise, for a manned space mission this could not be reasonable due to the fact that the electrical power generation could be vital for the crew. The spacecraft reachs the final orbit around Titan after 958.5 days (2.6 years) of space travel. By adding all the maneuvers estimated for the mission, only 381 days of the total mission duration are used to accelerate the spacecraft thanks to the thrust of the engine. Therefore, taking into account the 610 days of the coasting phase, when the engine is totally turned off, the total fuel (^{3}He) consumption for the entire mission is ≈ 0.112 kg.

Another possible solution, which could be revealed more feasible, is based on the DFD ability to turn off and on the thrust generation, though without restart the engine. In the thrust-coast-thrust profile mission, this is an important hypothesis which requires that the engine will not produce thrust for about a year, which is in theory possible but not yet certain, without stopping to generate the electrical power arising from the fusion reactions. In this case the fusion reactor still provide energy for all the entire mission, and the resulting fuel consumption would be ≈ 0.282 kg of ^{3}He.

4.5.4 Continuous thrust mission profile

The second alternative scenario analyzed is a contiuous thrust profile of the mission, which represents the natural alternative mission solution where the engine is always generating a constant thrust. It has been divided into four different phases: Earth departure, interplanetary trajectory, Saturn orbit insertion and Titan orbit insertion. The same engine has been considered also for the continuous thrust profile mission.
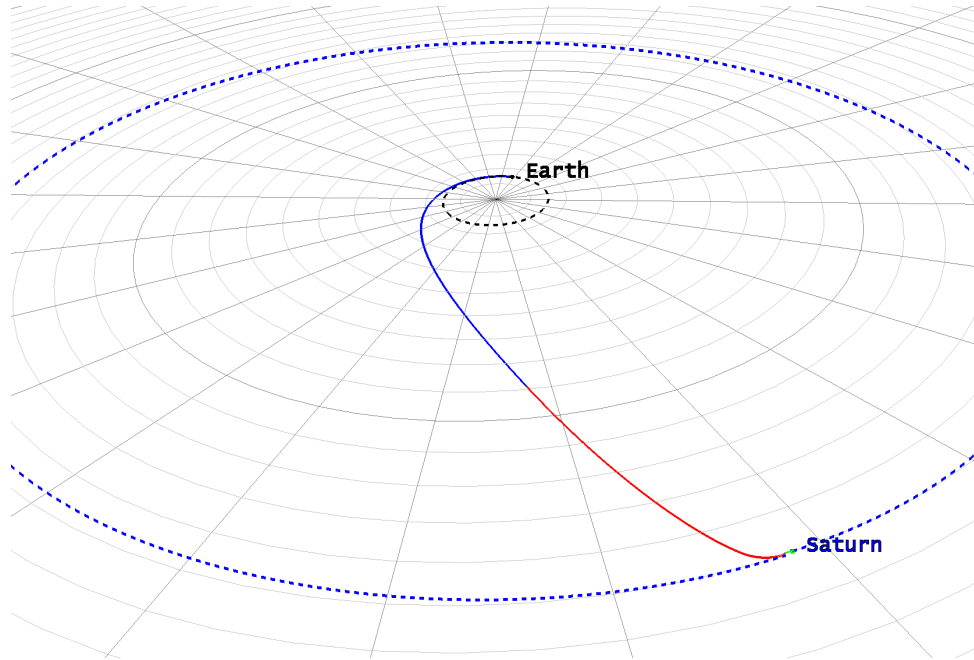
Figure 4.30: Planar trajectory for the continuous thrust profile mission. At the end of the white segment there is the change in direction of the thrust at the switch time. The trajectory follows Earth's orbit for some time before following a nearly straight trajectory to Saturn.

An iterative process is necessary to define the initial mass of the spacecraft, in order to define the propellant mass for all the mission which is directly related to the total duration of the trip. Starting from the same orbital initial conditions for the thrust-coast-thrust profile the same calculations have been performed, with the strong constraint on the thrust, which is active for all the time of the mission. The results from the Earth departure phase analysis are listed in Table 4.19.

Table 4.19: Earth departure spiral results achieved using the sparse non-linear optimizer (SNOPT) on STK software.

Start time	25 Sep 2047 11:44:51
Earth departure final time	28 Dec 2047 01:26:25
Maneuver time	93 days
Payload Mass	1000 kg
Initial spacecraft mass	9000 kg
Propellant mass used	686.99 kg
ΔV magnitude	7.475 km/s
Final velocity (Earth)	1.377 km/s

In this case the main goal of the calculation was to find a proper swicth time for the change in direction of the thrust in order to reach Saturn with an acceptable velocity (12.5 km/s) that allows to orbit around the planet. The results are listed in Table 4.20.

Table 4.20: Heliocentric orbit: results for the deep space maneuver achieved using the sparse non-linear optimizer (SNOPT) on STK software in order to minimize the propellant consumption.

Propagator model	Heliocentric
DSM start time	28 Dec 2047 01:26:25
Swicth time	14 Jan 2049 02:37:56
DSM final time	9 Sep 2049 09:11:07
Maneuver duration	383.05 + 238 days
Total mass at beginning	8313 kg
Propellant mass used	2812 + 1749 kg
ΔV magnitude	14.503 + 36.035 km/s
Initial velocity (Sun)	31.65 km/s
Velocity at swicth time (Sun)	47.814 km/s
Final velocity (Sun)	12.5 km/s

The Saturn and Titan orbit insertion maneuvers conclude this scenario and the relative results are given.
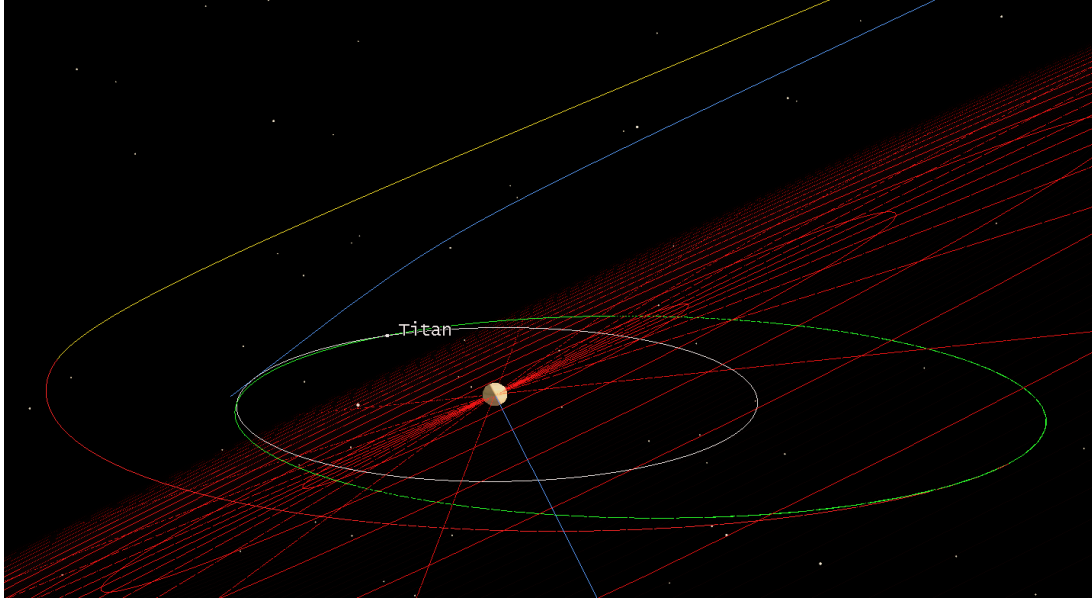
Figure 4.31: Saturn orbit insertion for the continuous thrust profile mission. The yellow line represents the primarily radial maneuver, then the red part is mainly acting along antivelocity vector and let the spacecraft orbit (green) around Saturn very close to Titan (white).

Finally, a summary for the entire alternative scenario is given in order to make a comparison with the previous solution taking into account mission durations and payload capability.

Table 4.21: Comparison between the thrust-cost-thrust (T-C-T) profile and the continuous thrust (continuous T) profile missions.

	T-C-T mission	continuous T mission
Start time (LEO)	2 Nov 2046	25 Sep 2047
Mission duration	958.5 days [2.63 years]	714.05 days [1.95 years]
Total mass at beginning	7250 kg	9015 kg
Payload mass	1800 kg	1000 kg
Propellant mass used	2558 kg + 100 kg (TOI)	5247 kg + 100 kg (TOI)
Fuel (^{3}He) mass used	0.282 kg	0.20 kg
Maximum trip Velocity (Sun)	34.560 km/s	47.814 km/s

As can be seen from Table 4.21, the CT profile mission results into a shorter time travel mission with a not negligible decrease in payload capability related to the fact that the propellant consumption has doubled. The decrease of the payload mass can be explained thinking about the Earth departure phase: the higher the inital mass the longer the time necessary to escape from Earth, staying more time into the Van Allen belt. Then, a smaller payload has been obtained, through an iterative process, in order to provide a relatively fast spiral Earth deparure comparable with the first scenario solution. Another

107

advantage related to the shortening of the total mission duration is the save of precious fuel mass (^{3}He) if compared with the scenario of the T-C-T profile mission. Preliminarily, is essential to underline that the first scenario analysed is based on the assumption that the DFD can turn off and on the thrust generation, which is in theory possible but not certain yet. This is an important hypothesis which requires that the engine will not produce thrust for more than a year, without stopping to generate the electrical power arising from the fusion reactions. Another solution has been considered: because of the robotic nature of the mission, it could be possible to shut down the engine, saving ^{3}He fuel; otherwise, for a manned space mission this could not be reasonable due to the fact that the electrical power generation could be vital for the crew. Taking into account the coasting phase, when the engine is turned off, the total fuel consumption for the entire mission would be about 0.112 kg instead of 0.282 kg relative to the case previously discussed.

Finally, there are two possible solutions related to the operative phase of the mission. The results lead two different feasible mission concepts. The high payload capability for both the mission profiles allows to consider a parachute descent through Titan's dense atmosphere performed by a lander probe, containing a rover or even better a rotorcraft, carried on the main spacecraft (orbiter). In this case, during the TOI maneuver, the orbiter will release the lander and keep orbiting around Titan or, performing a proper maneuver, it can orbit again around Saturn. In the first case the lander can be designed to collect scientific data for all the operative phase, sending it to the powerfull orbiter that is capable to receive and retransmit to Earth the precious data. In the latter case the lander will send data to the orbiter during the atmospheric descent and a period after the landing limited by the orbiter spacecraft trajectory and the lander power capability; moreover, after the separation, an orbiter deflection maneuver (ODM) would be required. This maneuver changes the path of the orbiter with just the right lander relative timing to perform the data relay during the descent, requiring a ΔV of tens m/s order of magnitude.

5 Conclusions

Realistic trajectories analysis were performed to accomplish a randezvous interplanetary mission to reach the Saturn-Titan system. An initial solution with an impulsive approach was used as the basis of a more accurate finite thrust analysis, which allows to estimate the propellant mass required, the flight time as well as the type of maneuvers necessary to acoomplish the mission. Our analysis confirmed that a Titan mission concept using a 2-MW class DFD engine is feasible, also taking into account an Earth departure from LEO, dramatically reducing launch and overall mission costs and also allows checkout and testing in low Earth orbit. Moreover, the strong advantages related to this new propulsion system concept result in a great reduction of travel time with respect to the previous performed missions and a tremendous payload capability increase with a huge availability of electrical power during all the mission.

For our work purpose, the engine performance listed in Table 5.1 have been considered and the results are extremely promising although the conservative assumption on the specific power of the engine, which is the lowest estimated value arising from the power and mass budget performed by the PSS and PPPL.

Table 5.1: Performance of the Direct Fusion Drive used for all the calculations.

Fusion Power	2 MW
Specific Impulse	9600 s
Thrust	8 N
Specific Power	0.75 kW/kg
Thrust Efficiency	0.5
Engine mass	2660 kg

Several finite maneuver analysis have been performed, using Astrogator tool on STK software, estimating the mission phases duration and the propellant mass consumption for all the required maneuvers. In order to accomplish this goal, the proper thrust vector direction and maneuver duration have been estimated, using the SNOPT solver where practical. Most of the time the thrust vector has been considered updated throughout the maneuver to maintain the required thrust direction. This choice forces the thrust vector to the desired direction at every instant during the burn, rotating with a specified coordinate system or tracking with the spacecraft's inertial velocity vector. In a future research work, it could be more appropriate to consider an inertial at ignition condition, where the thrust vector direction is defined by attitude control at ignition and remains the same throughout the maneuver. This fixes the thrust direction in the inertial direction calculated at the beginning of the burn and is used for inertially fixed spacecraft. This option does not require a continuous attitude change, which is necessary in the update during burn option and in some cases makes the maneuver more feasible. However taking into account the main objective of the thesis work, which was to estimate the propellant mass required for the mission and the payload capability, this choice does not affect significantly the results. Moreover, a real numeric optimization process was not performed, although a basic optimization has proven to be useful to approximate the optimal thrust direction

and to minimize the duration of burns, hence the propellant used using the SNOPT solver on STK software.

The first scenario analysed for the Titan mission is based on the DFD ability to turn off and on the thrust generation, though without restart the engine. In the thrust-coast-thrust profile mission, this is an important hypothesis which requires that the engine will not produce thrust for about a year, which is in theory possible but not certain yet, without stopping to generate the electrical power arising from the fusion reactions. Another option has been considered. More specifically, because of the robotic nature of the mission, it could be possible to think to turn off the entire engine in order to save precious fuel (^{3}He); otherwise, for a manned space mission this could not be reasonable due to the fact that the electrical power generation could be vital for the crew. By adding all the maneuvers estimated, only 381 days of the total mission duration are used to accelerate the spacecraft thanks to the thrust of the engine. Therefore, taking into account the 610 days of the coasting phase, when the engine is turned off, the total fuel (^{3}He) consumption for the entire mission would be about 0.112 kg instead of 0.282 kg relative to the case previously discussed, which is listed in Table 5.2.

This solution leads to a higher payload capability and mission duration than the continuous thrust profile mission, as can be seen in the Table 5.2, due to the fact that the thrust is not active during all the mission phases, meaning less propellant to carry onboard. As a consequence, considering the same amount of payload, a faster spiral Earth departure is possible for the thrust-coast-thrust profile mission. In fact a smaller payload has been obtained for the continuous thrust profile mission, in order to provide a relatively fast spiral Earth deparure comparable with the first scenario solution.

Table 5.2: Comparison between the thrust-cost-thrust (T-C-T) profile and the continuous thrust (continuous T) profile missions.

	T-C-T mission	continuous T mission
Start time (LEO)	2 Nov 2046	25 Sep 2047
Earth departure duration	76 days	93 days
Payload mass	1800 kg	1000 kg
Total mass at beginning	7250 kg	9000 kg
Date of arrival (Saturn)	15 Dec 2049	20 Nov 2049
Mission duration	958.5 days [2.63 years]	714.05 days [1.95 years]
Propellant mass used	2558 kg + 100 kg(TOI)	5247 kg + 100 kg(TOI)
Fuel (^{3}He) mass used	0.282 kg	0.2 kg
Maximum trip Velocity (Sun)	34.560 km/s	47.814 km/s

From the continuous thrust profile solution is also noticible that the DFD is capable of really fast travel, rapidly reaching extremely high velocity. In the last mission phases, when a great amount of propellant has already been consumed and the spacecraft mass has decreased, the DFD can reach the required speed in a relatively short period, reducing of many years the time of flight. Collectively, such kind of maneuvers would have been too demanding for any kind of current propulsion systems. This is one of the DFD game-changer. This capability results in total trip duration of less than 2 years if we consider

the continuous thrust profile mission, which is more than three times less the duration of the travel of the Cassini spacecraft (7 years) to Saturn system, which has been possible due to several gravity assists.

It is important to emphasize that also the payload is much higher than that of the previous mission, delivering 1000 kg in the fastest solution or 1800 kg in the thrust-coast-thrust profile mission. For comparison the Cassini spacecraft had a total payload of 617 kg including the entire Huygens-lander (349 kg) [85]. This increase in the payload capability, combined with the huge electrical power availability generated by the fusion reactor, leads to a tremendous growth of scientific data. In fact, for any robotic mission, the higher the payload mass, the more scientific instruments can be carry onboard and the more precious data can be collected. This is a key aspect also thinking to the near future lunar and Mars missions, where it would be essential to increase as much as possible the payload.

Realistic trajectories analysis have been performed to accomplish a randezvous interplanetary mission to reach the Saturn-Titan system. An initial solution with an impulsive approach has been used as the basis of a more accurate finite thrust analysis. Our analysis confirmed that a Titan mission concept using a 2-MW class DFD engine is feasible, also taking into account an Earth departure from LEO, dramatically reducing launch and overall mission costs and also allows checkout and testing in low Earth orbit. Moreover, the strong advantages related to this new propulsion system concept result in a great reduction of travel time with respect to the previous performed missions and a tremendous payload capability increase with a huge availability of electrical power during all the mission. This kind of engine would be truly game-changing for any robotic missions to asteroids, Jupiter and its moons, and any other deep space destination become more faster, cheaper, and can return orders of magnitude more science. There are many missions that can be accomplished now with a small amount of ^{3}He from terrestrial sources, and enormous reserves are available on the moon for future missions [45, 46]. Several finite maneuver analysis have been performed, estimating the mission phases duration and the propellant mass consumption for all the required maneuvers. In order to accomplish this goal, the proper thrust vector orientation and maneuver duration have been numerically estimated. Most of the time the thrust vector has been considered updated throughout the maneuver to maintain the required thrust direction. This choice forces the thrust vector to the desired direction at every instant during the burn, rotating with a specified coordinate system or tracking with the spacecraft's inertial velocity vector. In a future research work, it could be more appropriate to consider an inertial at ignition condition, where the thrust vector direction is defined by attitude control at ignition and remains the same throughout the maneuver. This fixes the thrust direction in the inertial direction calculated at the beginning of the burn and is used for inertially fixed spacecraft. This option does not require a continuous attitude change, that is necessary in the update during burn option and in some cases makes the maneuver more feasible. However, this choice does not affected significantly the results, which are extremely promising although the conservative assumption on the specific power of the engine. Moreover, a real numeric optimization process was not performed, although a basic optimization has proven to be useful to approximate the thrust direction, minimizing the duration of burns, hence the propellant used.

From the CT profile solution is also noticible that the DFD is capable of really fast travels, rapidly reaching extremely high velocity. In the last mission phases, when a great amount of propellant has already been consumed and the spacecraft mass has decreased, the DFD can reach the required speed in a relatively short period, reducing of many years the time of flight. Collectively, such kind of maneuvers would have been too demanding for any kind of current propulsion systems. This observations result in a total trip duration of less than 2 years for the CT profile mission, which is more than three times less the duration of the Cassini spacecraft travel to Saturn, which has been possible due to several gravity assists. It is important to emphasize that also the payload is much higher, delivering 1000 kg in the fastest solution or 1800 kg in the T-C-T profile mission. For comparison the Cassini spacecraft had a total payload of 617 kg including the Huygens-lander (349 kg) [85]. This increase in the payload capability, combined with the huge electrical power availability generated by the fusion reactor, leads to a tremendous growth of scientific data. In fact, for any robotic mission, the higher the payload, the more scientific instruments can be carry onboard and the more precious data can be collected. This is a key aspect also thinking to the near future lunar and Mars mission where it would be essential to increase as much as possible the payload.

Appendix A: Matlab® Files

Script used in Chapter 4.5.1 for the preliminary estimation on the propellant mass required for the mission, using an impulsive approach.

```matlab
1   clear all
2   close all
3   clc
4
5   % Engine parameters chosen and fixed :
6   % Propellant mass related to the mission Delta V obtained
7   % from the Lambert Problem .
8
9   %% INPUT DATA
10
11  Thrust = 8;              % Newton
12  g = 9.806;               % m/s^2
13  Isp = 9600;              % s
14  payload = 1000;          % kg
15  Engine = 2800;           % kg
16  propellstima = 2150      % kg
17  factor = 100;            % kg
18  initialmass = payload + Engine + propellstima + factor; % kg
19  DeltaV = 40;             % km/s
20
21  %% RESULTS
22
23  meanmass = initialmass − (propellstima)/2        % kg
24  acceleraz = Thrust / meanmass;                   % mean
         acceleration
25  days = DeltaV*1000 / (acceleraz)  /3600 / 24;   % burning time
26
27  mpunto = Thrust / (g*Isp);                       % kg/s
28  mp = mpunto*days*24*3600;                        % kg
```

Script used in Chapter 4.5.1 for the initial estimation for the dependence of the mission masses on time of flight, using the Tsiolkovsky rocket equation:

```matlab
1  clear all
2  close all
3  clc
4
5  DeltaV = 46000;                                    % m/s
6  % Delta_t = linspace(1,15);                        % years
7  % m_0 = [0:500:10000];                             % kg
8  Delta_t = 31536000*linspace(0,15);                 % sec
9  m_0 = 10000;                                       % kg
10 I_sp = 8500;                                       % sec
11 g_0 = 9.80665;                                     % m/s^2
12 alfa = 0.75e-3;                                    % 0.75 kg/kW
13 eta = 0.5;                                         % Overall efficiency
14
15 m_f = m_0 * exp( -DeltaV / (I_sp * g_0) );  % Rocket equation
16
17 m_u = m_0 * ( exp(-DeltaV / (I_sp * g_0)) - (alfa / 2*eta)*(
       DeltaV^2./Delta_t)*((I_sp * g_0)^2/DeltaV^2)*(1-exp(-DeltaV /
       (I_sp * g_0))) );
18
19 % plot(m_0, m_f)
20
21 figure(1)
22 plot((Delta_t/86400/365),m_u) % payload mass vs Delta t
23 grid
24 xlabel('Time of flight [years]')
25 ylabel('payload mass [kg]')
26
27 figure(2)
28 plot((Delta_t/86400/365),(m_u/m_0)) % m_u/m_0 vs Delta t
29 grid
30 xlabel('Time of flight [years]')
31 ylabel('m_u/m_0')
32
33 %%%%%%%%%%%%%%%%%%%%% Delta V - Time %%%%%%%%%%%%%%%%%%%%%
34
35 Delta_V =
       [135.115615309690,98.2070551213005,76.4975623374538,62.2867678035864,

36     52.2980246367246,44.9108047461483,39.2370506811036,35.1280845263469,

37     35.0010619900612,37.4967223452279,39.6295434033359,41.4495226129899,
```

```
38        42.9847283353299,44.2414684060335,45.2032372493555,45.8363560693190,

39        46.1171917026007,46.0745863314108,45.7940710725970,45.3720582270278,

40        44.8804398211618,44.3629742525131,43.8439595258111,43.3362626447209,

41        42.8463719241061,42.3772527858271,41.9299234235464,41.5043287255959,

42        41.0998319693925,40.7154955236698,40.3502427707006,40.0029517982542,

43        39.6725091877214,39.3578401281330,39.0579243487600,38.7718035242411];

44
45   DELTA_t = (300:100:3800)/365;
46
47   % figure(3)
48   % plot(DELTA_t, Delta_V)
49   % grid
50   % xlabel('Time of flight [years]')
51   % ylabel('Delta V [km/s]')
52
53   P = polyfit(DELTA_t, Delta_V,7);
54   Y = polyval(P,DELTA_t);
55
56   figure(3)
57   plot(DELTA_t,Y)
58   grid
59   xlabel('Time of flight [years]')
60   ylabel('Delta V [km/s]')
61   title('Delta V Estimation for Titan Orbit Randevouz (Launch
        2030)') % rif Start=2025-11-12
62   legend('Delta V Lambert Solution')
63
64   %DELTA_t = (300:100:3800)*86400;      % s
65   DELTA_t = (300:100:2200)*86400;       % s
66
67   %%%%%%%%%%%%%%%%%%%%%%%%%%%%%%%%%%%%%%%%%%%%%%%%%%%%%%%%%%%%%%%%%%%%%%%%%
68
69   m_payload = 1000;
70
71   m_struttura = 2660 + 1000; % 2800 + 1000 , Scatter factor
72   m_finale = m_struttura + m_payload;
73
```

```matlab
74  m_iniziale = m_finale * (exp( (1000*Delta_V(1:20)) / (I_sp * g_0
       )) ); % try erase (1:20)
75  % m_iniz = m_payl ./ ( exp(-Delta_V ./ (I_sp * g_0)) - (alfa /
       2*eta)*(Delta_V.^2 ./ DELTA_t).*((I_sp * g_0)^2 ./Delta_V.^2)
       .*(1-exp(-Delta_V ./ (I_sp * g_0))) )';
76
77  m_prop = m_iniziale - m_finale;
78
79  figure(4)
80
81  Pol = polyfit((DELTA_t/86400/365), m_iniziale ,15);
82  % propellant mass,(DELTA_t/86400),m_prop,'--b'
83  YY = polyval(Pol,(DELTA_t/86400/365));
84  plot((DELTA_t/86400/365),YY,'b', (DELTA_t/86400/365),m_prop,'--b
       ')
85
86  % plot((DELTA_t/86400/365),m_iniziale ,'b', (DELTA_t/86400/365),
       m_prop,'--b')
87  % Delta_V   or   (DELTA_t/86400/365)
88
89  grid
90  xlabel('Time of flight [years]')        % Delta V [km/s]   or
       Time of flight [years]
91  ylabel('mass [kg]')
92  hold on
93
94  %%%%%%%%%%%%%%%%%%%%%%%%%%%%%%%%%%%%%%%%%%%%%%%%%%%%%%%%%%%%%%%%%%%
95
96  m_payload = 2000;
97  %DELTA_t = (300:100:3800)*86400;    % s
98  DELTA_t = (300:100:2200)*86400;     % s
99  m_finale = m_struttura + m_payload;
100
101  m_iniziale = m_finale * (exp( (1000*Delta_V(1:20)) / (I_sp * g_0
       )) ); % erase (1:20)
102  % m_iniz = m_payl ./ ( exp(-Delta_V ./ (I_sp * g_0)) - (alfa /
       2*eta)*(Delta_V.^2 ./ DELTA_t).*((I_sp * g_0)^2 ./Delta_V.^2)
       .*(1-exp(-Delta_V ./ (I_sp * g_0))) )';
103
104  m_prop = m_iniziale - m_finale;
105
106  Pol = polyfit((DELTA_t/86400/365), m_iniziale ,15);
107  % propellant mass,(DELTA_t/86400),m_prop,'--b'
108  YY = polyval(Pol,(DELTA_t/86400/365));
```

```matlab
109  plot((DELTA_t/86400/365),YY,'r', (DELTA_t/86400/365),m_prop,'--r
        ')
110
111  %(DELTA_t/86400/365),m_iniziale,'r', (DELTA_t/86400/365),m_prop
        ,'--r')
112  % Delta_V   or   (DELTA_t/86400/365)
113
114  hold on
115
116  %%%%%%%%%%%%%%%%%%%%%%%%%%%%%%%%%%%%%%%%%%%%%%%%%%%%%%%%%%%%%%%%%%%%
117
118  m_payload = 3000;
119  %DELTA_t = (300:100:3800)*86400;     % s
120  DELTA_t = (300:100:2200)*86400;      % s
121
122  m_finale = m_struttura + m_payload;
123
124  m_iniziale = m_finale * (exp( (1000*Delta_V(1:20)) / (I_sp * g_0
        )) ); % erase (1:20)
125  % m_iniz = m_payl ./ ( exp(-Delta_V ./ (I_sp * g_0)) - (alfa /
        2*eta)*(Delta_V.^2 ./ DELTA_t).*((I_sp * g_0)^2 ./Delta_V.^2)
        .*(1-exp(-Delta_V ./ (I_sp * g_0))) )';
126
127  m_prop = m_iniziale - m_finale;
128
129  Pol = polyfit((DELTA_t/86400/365), m_iniziale,15);
130  % propellant mass,(DELTA_t/86400),m_prop,'--b'
131  YY = polyval(Pol,(DELTA_t/86400/365));
132  plot((DELTA_t/86400/365),YY,'g', (DELTA_t/86400/365),m_prop,'--g
        ')
133
134  % plot((DELTA_t/86400/365),m_iniziale,'g',(DELTA_t/86400/365),
        m_prop,'--g')
135  % Delta_V   or   (DELTA_t/86400/365)
136
137  hold on
138  legend('initial mass for 1000 kg payload','propellant mass for
        1000 kg payload','initial mass for 2000 kg payload','
        propellant mass for 2000 kg payload','initial mass for 3000
        kg payload','propellant mass for 3000 kg payload' )
139  title('Mass Estimation with Engine Mass of 2800 kg')
140
141  %%%%%%%%%%%%%%%%%%%%%%%%%%%%%%%%%%%%%%%%%%%%%%%%%%%%%%%%%%%%%%%%%%%%
142
```

```matlab
143  % figure(5)
144  % plot((DELTA_t/86400/365),m_iniziale,'b')
145  % propellant mass,(DELTA_t/86400),m_prop,'--b'
146  % grid
147  % xlabel('Time of flight [years]')
148  % ylabel('initial mass [kg]')
149
150  figure(5)
151  Pol = polyfit((DELTA_t/86400/365), m_iniziale,15);
152  % propellant mass,(DELTA_t/86400),m_prop,'--b'
153  YY = polyval(Pol,(DELTA_t/86400/365));
154
155  plot((DELTA_t/86400/365),YY,'b')
156  grid
157  xlabel('Time of flight [years]')
158  ylabel('initial mass [kg]')
```

References

[1] S. A. Cohen, C. Swanson, N. McGreivy, A. Raja, E. Evans, P. Jandovitz, M. Khodak, G. Pajer, T. Roglien, S. Thomas, et al., Direct fusion drive for interstellar exploration, submitted to JBIS (2019).

[2] R. Godwin, Apollo 11: The NASA Mission Reports, no. v. 1 in Apogee Bks, Apogee Books, 1999.
URL https://books.google.com/books?id=bHtpkI9Vk4gC

[3] D. Chappell, Mars Robotic Exploration Missions: Mars Subsurface Radar Mapper Design, 1995.
URL https://books.google.com/books?id=-m-tmwEACAAJ

[4] L. Casalino, Propulsione spaziale, Appunti di lezione, Politecnico di Torino, (2018).

[5] S. Scarsoglio, Human body alterations in space, in: Appunti di lezione, Politecnico di Torino, (2019).

[6] J. Samarabandu, R. Acharya, E. Hausmann, K. Allen, Analysis of bone x-rays using morphological fractals, IEEE transactions on medical imaging 12 (3) (1993) 466–470.

[7] G. L. Matloff, Deep space probes: To the outer solar system and beyond, Springer Science & Business Media, (2006).

[8] G. Vulpetti, L. Johnson, G. L. Matloff, Solar sails: a novel approach to interplanetary travel, Springer, (2014).

[9] C. R. McInnes, Solar sailing: technology, dynamics and mission applications, Springer Science & Business Media, (2004).

[10] J. C. Maxwell, Viii. a dynamical theory of the electromagnetic field, Philosophical transactions of the Royal Society of London (1865) 459–512.

[11] J. C. Maxwell, A treatise on electricity and magnetism, Vol. 1, Clarendon press, (1881).

[12] M. Macdonald, Solar sailing: applications and technology advancement (2011).

[13] Y. Tsuda, O. Mori, R. Funase, H. Sawada, T. Yamamoto, T. Saiki, T. Endo, J. Kawaguchi, Flight status of ikaros deep space solar sail demonstrator, Acta Astronautica 69 (9-10) (2011) 833–840.

[14] Y. Tsuda, O. Mori, R. Funase, H. Sawada, T. Yamamoto, T. Saiki, T. Endo, K. Yonekura, H. Hoshino, J. Kawaguchi, Achievement of ikaros—japanese deep space solar sail demonstration mission, Acta Astronautica 82 (2) (2013) 183–188.

[15] B. Initiatives, https://breakthroughinitiatives.org/initiative/3 (2018).

[16] P. Lubin, A roadmap to interstellar flight, arXiv preprint arXiv:1604.01356 (2016).

[17] G. Genta, Next Stop Mars: The Why, How, and When of Human Missions, Springer, (2016).

[18] R. Y. Kezerashvili, O. L. Starinova, A. S. Chekashov, D. J. Slocki, Inflation deployed torus-shaped solar sail accelerated via thermal desorption of coating, arXiv preprint arXiv:1908.06761 (2019).

[19] F. Romanelli, C. Bruno, G. Regnoli, Assessment of open magnetic fusion for space propulsion, ESA-ESTEC Final Report, ESA-ARIADNA Contract 18853 (05) (2005).

[20] G. Schmidt, J. Bonometti, P. Morton, Nuclear pulse propulsion-orion and beyond, in: 36th AIAA/ASME/SAE/ASEE Joint Propulsion Conference and Exhibit, (2000), p. 3856.

[21] G. Dyson, Project orion: The true story of the atomic spaceship (2002).

[22] T. J. Lawrence, Nuclear-thermal-rocket propulsion systems, Nuclear space power and propulsion systems (2008) 31.

[23] W. Robbins, An historical perspective of the nerva nuclear rocket engine technology program, in: Conference on Advanced SEI Technologies, (1991), p. 3451.

[24] G. L. Bennett, R. J. Hemler, A. Schock, Space nuclear power-an overview, Journal of propulsion and power 12 (5) (1996) 901–910.

[25] A. T. Josloff, N. F. Shepard, T. S. Chan, F. C. Greenwood, N. A. Deane, J. D. Stephen, R. E. Murata, Sp-100 generic flight system design and early flight options, in: AIP Conference Proceedings, AIP, (1994), pp. 533–538.

[26] A. Lépine-Szily, P. Descouvemont, Nuclear astrophysics: nucleosynthesis in the universe, International journal of astrobiology (2012) 243–250.

[27] A. Einstein, Einstein's proposal of the photon conceptfia translation of the annalen der physik paper of 1905, Ann. Physik 17 (1905) 132.

[28] C. for nuclear science, technology, Nuclear fission, `http://nuclearconnect.org/know-nuclear/science/nuclear-fission` (2015).

[29] `https://openstax.org` (2016).

[30] I. A. Crawford, Interstellar travel: a review for astronomers, Quarterly Journal of the Royal Astronomical Society 31 (1990) 377–400.

[31] M. Amoretti, C. Amsler, G. Bazzano, G. Bonomi, A. Bouchta, P. Bowe, C. Carraro, C. Cesar, M. Charlton, M. Doser, et al., High rate production of antihydrogen, Physics Letters B 578 (1-2) (2004) 23–32.

[32] `https://www.britannica.com/science/cross-section-physics` (2016).

[33] J. Lilley, Nuclear physics: principles and applications, John Wiley & Sons, (2013).

[34] B. R. Martin, G. Shaw, Nuclear and particle physics: an introduction, John Wiley & Sons, (2019).

[35] K. S. Krane, D. Halliday, et al., Introductory nuclear physics, John Wiley & Sons, (1987).

[36] B. Zohuri, Hydrogen driving thermonuclear fusion energy, in: Hydrogen Energy, Springer, (2019), pp. 61–120.

[37] B. Zohuri, Plasma physics and controlled thermonuclear reactions driven fusion energy, Springer, (2016).

[38] S. Glasstone, R. Lovberg, Controlled thermonuclear reactions, d. vannorstrand company, Inc., New York (1960).

[39] A. A. Sokolov, I. M. Ternov, Synchrotron radiation, Akademia Nauk SSSR, Moskovskoie Obshchestvo Ispytatelei prirody. Sektsia Fiziki. Sinkhrotron Radiation, Nauka Eds., Moscow, 1966 (Russian title: Sinkhrotronnoie izluchenie), 228 pp. (1966).

[40] C. Kunz, Synchrotron radiation (1974).

[41] B. Zohuri, Inertial confinement fusion driven thermonuclear energy, Springer, (2017).

[42] H. Zerriffi, Tritium Production: DOE Moves Ahead Where Non-Proliferationists Fear to Tread, IEER, Science for Democratic Action Vol. 5 N 1 1996, (1996).

[43] R. Kennedy, The interstellar fusion fuel resource base of our solar system, Journal of the British Interplanetary Society 71 (2018) 298–305.

[44] G. Turner, M. ozima and fa podosek noble gas geochemistry . cambridge (cambridge university press) 2002. 300 pp. price (hardback)£ 55. isbn 05 2180 366 7, Mineralogical Magazine 67 (2) (2003) 418–419.

[45] L. Wittenberg, J. Santarius, G. Kulcinski, Lunar source of 3he for commercial fusion power, Fusion technology 10 (2) (1986) 167–178.

[46] W. Fa, Y.-Q. Jin, Quantitative estimation of helium-3 spatial distribution in the lunar regolith layer, Icarus 190 (1) (2007) 15–23.

[47] https://www.theguardian.com/environment/2009/may/28/national-ignition-facility-fusion-energy (2009).

[48] A. J. Chorin, Numerical solution of the navier-stokes equations, Mathematics of computation 22 (104) (1968) 745–762.

[49] https://alfven.princeton.edu/research/past/MagneticNozzle (2015).

[50] https://www.enea.it/it.

[51] L. Spitzer Jr, The stellarator concept, The Physics of Fluids 1 (4) (1958) 253–264.

[52] G. H. Miley, Status of fusion research and implications for d/he-3 systems, NASA, Lewis Research Center (1988).

[53] H. Momota, A. Ishida, Y. Kohzaki, G. H. Miley, S. Ohi, M. Ohnishi, K. Sato, L. C. Steinhauer, Y. Tomita, M. Tuszewski, Conceptual design of the d-3he reactor artemis, Fusion Technology 21 (4) (1992) 2307–2323.

[54] A. Kolb, C. Dobbie, H. Griem, Field mixing and associated neutron production in a plasma, Physical Review Letters 3 (1) (1959) 5.

[55] https://commons.wikimedia.org/wiki/File:Field-Reversed_Configuration.svg.

[56] A. Ishida, H. Momota, L. Steinhauer, Variational formulation for a multifluid flowing plasma with application to the internal tilt mode of a field-reversed configuration, The Physics of fluids 31 (10) (1988) 3024–3034.

[57] Y. S. Razin, G. Pajer, M. Breton, E. Ham, J. Mueller, M. Paluszek, A. H. Glasser, S. A. Cohen, A direct fusion drive for rocket propulsion, Acta Astronautica 105 (1) (2014) 145–155.

[58] M. Rosenbluth, M. Bussac, Mhd stability of spheromak, Nuclear Fusion 19 (4) (1979) 489.

[59] S. A. Cohen, R. Milroy, Maintaining the closed magnetic-field-line topology of a field-reversed configuration with the addition of static transverse magnetic fields, Physics of Plasmas 7 (6) (2000) 2539–2545.

[60] S. A. Cohen, B. Berlinger, C. Brunkhorst, A. Brooks, N. Ferraro, D. Lundberg, A. Roach, A. Glasser, Formation of collisionless high-β plasmas by odd-parity rotating magnetic fields, Physical review letters 98 (14) (2007) 145002.

[61] L. C. Steinhauer, Review of field-reversed configurations, Physics of Plasmas 18 (7) (2011) 070501.

[62] D. Welch, S. A. Cohen, T. Genoni, A. Glasser, Formation of field-reversed-configuration plasma with punctuated-betatron-orbit electrons, Physical review letters 105 (1) (2010) 015002.

[63] A. H. Glasser, S. A. Cohen, Ion and electron acceleration in the field-reversed configuration with an odd-parity rotating magnetic field, Physics of Plasmas 9 (5) (2002) 2093–2102.

[64] S. A. Cohen, A. Landsman, A. Glasser, Stochastic ion heating in a field-reversed configuration geometry by rotating magnetic fields, Physics of Plasmas 14 (7) (2007) 072508.

122

[65] Princeton Plasma Physics Laboratory (PPPL), Princeton Satellite Systems (PSS) - Private communication, (2020).

[66] S. J. Thomas, M. Paluszek, S. Cohen, N. McGreivy, E. Evans, Fusion-enabled pluto orbiter and lander, in: AIAA SPACE and Astronautics Forum and Exposition, (2017), p. 5276.

[67] M. Paluszek, G. Pajer, Y. Razin, J. Slonaker, S. Cohen, R. Feder, K. Griffin, M. Walsh, Direct fusion drive for a human mars orbital mission, in: Proceedings, International Astronautical Congress (AIC) IAC-12, C4, 7-C3. 5, 10, no. PPPL-5064, Princeton Plasma Physics Lab.(PPPL), Princeton, NJ (United States), (2014).

[68] N. McGreivy, UEDGE simulations of a direct fusion drive FRC rocket, SULI Report:, (2016).

[69] R. R. Bate, D. D. Mueller, J. E. White, W. W. Saylor, Fundamentals of astrodynamics, Dover publications, (2019).

[70] https://phys.libretexts.org/Bookshelves/Astronomy_and_Cosmology_
TextMaps/Map%3A_Celestial_Mechanics_(Tatum)/14%3A_General_
Perturbation_Theory/14.4%3A_Lagrange's_Planetary_Equations.

[71] J. P. Vinti, Gaussian variational equations for osculating elements of an arbitrary separable reference orbit, Celestial mechanics 7 (3) (1973) 367–375.

[72] G. Monegato, Fondamenti di calcolo numerico, Clut, (1998).

[73] P. E. Gill, W. Murray, M. A. Saunders, SNOPT: An SQP algorithm for large-scale constrained optimization, SIAM Rev. 47 (2005) 99–131.

[74] P. E. Gill, W. Murray, M. A. Saunders, E. Wong, User's guide for SNOPT 7.7: Software for large-scale nonlinear programming, Center for Computational Mathematics Report CCoM 18-1, Department of Mathematics, University of California, San Diego, La Jolla, CA (2018).

[75] C. Sotin, R. Jaumann, B. Buratti, R. H. Brown, R. Clark, L. Soderblom, K. Baines, G. Bellucci, J.-P. Bibring, F. Capaccioni, et al., Release of volatiles from a possible cryovolcano from near-infrared imaging of titan, Nature 435 (7043) (2005) 786.

[76] G. Tobie, J. I. Lunine, C. Sotin, Episodic outgassing as the origin of atmospheric methane on titan, nature 440 (7080) (2006) 61–64.

[77] S. Rodriguez, S. Le Mouélic, J. Barnes, J. Kok, S. Rafkin, R. Lorenz, B. Charnay, J. Radebaugh, C. Narteau, T. Cornet, et al., Observational evidence for active dust storms on titan at equinox, Nature Geoscience 11 (10) (2018) 727–732.

[78] C. Elachi, S. Wall, M. Allison, Y. Anderson, R. Boehmer, P. Callahan, P. Encrenaz, E. Flamini, G. Franceschetti, Y. Gim, et al., Cassini radar views the surface of titan, Science 308 (5724) (2005) 970–974.

[79] C. C. Porco, E. Baker, J. Barbara, K. Beurle, A. Brahic, J. A. Burns, S. Charnoz, N. Cooper, D. D. Dawson, A. D. Del Genio, et al., Imaging of titan from the cassini spacecraft, Nature 434 (7030) (2005) 159.

[80] https://sci.esa.int/web/cassini-huygens/2085-objectives/.

[81] https://solarsystem.nasa.gov/missions/cassini/the-journey/the-spacecraft/.

[82] https://solarsystem.nasa.gov/missions/cassini/mission/quick-facts/.

[83] https://www.jpl.nasa.gov/missions/cassini-huygens/.

[84] https://www.esa.int/Science_Exploration/Space_Science/Cassini-Huygens/Cassini_spacecraft.

[85] D. M. Harland, Mission to Saturn: Cassini and the Huygens probe, Springer Science & Business Media, 2002.

[86] R. T. Mitchell, Cassini/huygens at saturn and titan, Acta Astronautica 59 (1-5) (2006) 335–343.

[87] I. Newton, The Principia: mathematical principles of natural philosophy, Univ of California Press, (1999).

Ringraziamenti